Tore Grüner Bjåstad

# High frame rate ultrasound imaging using parallel beamforming

Thesis for the degree of Philosophiae Doctor

Trondheim, January 2009

Norwegian University of Science and Technology
Faculty of Medicine
Department of Circulation and Medical Imaging

**◉ NTNU**
Norwegian University of
Science and Technology

## Høg bilderate i ultralydavbilding ved hjelp av parallell stråleforming

Denne avhandlinga omhandlar ein teknikk for å auke ultralyd bilderate kalla parallell stråleforming. Bruksområdet er avgrensa til hjerteavbilding, sidan det er denne type avbilding som stiller høgast krav til bilderate.

Hjartemuskelen trekk seg saman og slappar av omtrent ein gong kvart sekund. Kontraksjonen er ein kompleks prosess der ulike delar av hjartet trekk seg saman til ulike tider og med forskjellig hastigheit. For å kunne studere denne bevegelsen nøyaktig med ultralyd, treng ein høg bilderate. Eit ultralydbilete vert danna ved å skyte ein avbildingspuls langs ei rekke med skannelinjer som dekker objektet ein vil avbilde. Bilderata er då begrensa av kor mange strålar ein nyttar, og av tida det tar for ein avbildingspuls å propagere langs ei skannelinje til maksimal avbildingsdybde og attende.

Multippel linjeakkvisisjon, MLA, er ein teknikk som ofte vert nytta for å auke bilderata. I staden for å lage kun ei bildelinje for kvar sendepuls, lagar ein med denne teknikken fleire linjer i parallell. Teknikken vert også kalla parallell stråleforming og kan då auke bilderata proporsjonalt med antalet parallelle skannelinjer. Ulempa med teknikken er at den fører til uønska bildeartefakt. Artefakta har ein stripeliknandes utsjånad og er spesielt tydelige i bildesekvensar (filmar). Eit mål med denne avhandlinga er å kunne nytte parallell stråleforming til å auke bilderata utan at det resulterar i bildeartefakt.

Avhandlinga inneheld resultat frå data-simuleringar, in-vitro- og in-vivo målingar. Det visast at forskyvinga mellom sende- og mottakarretning når ein nyttar MLA fordreiar puls-ekko-responsen til kvar skannelinje. Dette gir eit skift-variant avbildingssystem med bildeartefakt. Avhandlinga omfattar fire bidrag. Bidraga inneheld beskrivingar av målemetodar for å evaluere og kvantifisere puls-ekko-fordreiinga, bildeartefakt og skiftinvarians. Bidraga inneheld også evalueringar og samanlikningar av forskjellige metodar for reduksjon av MLA-bildeartefakt. Dei to metodane som har blitt mest vektlagt er styringskompensasjon og syntetiske sendestrålar (STB, Synthetic Transmit Beam). Styringskompensasjon gav god reduksjon av bildeartefakt under ideelle forhold, men virkninga vart kraftig redusert i realistiske scenario med aberrasjonar. STB-metoda metoda gav god reduksjon av bildeartefakt både med og utan aberrasjonar. I tillegg visast det at ein ved å nytte STB akvisisjonsmønsteret også kan estimere vevshastigheit med ei nøyaktigheit som er samanliknbar med konvensjonell vevsdoppler.

Tore Grüner Bjåstad
Institutt for sirkulasjon og bildediagnostikk, NTNU
Hovedveileder: Hans Torp, Biveileder: Kjell Kristoffersen

# Abstract

The human heart contracts and relaxes approximately once each second. This is a complex process where different parts of the cardiac tissue contract and relax at different times and at different rates. The accurate evaluation of this deformation with ultrasound requires the use of a high frame rate. The frame rate of a conventional ultrasound image is limited by the round trip propagation time of the sound pulse along each of the scan lines covering the imaged object. A common technique to increase the frame rate is multiple line acquisition, MLA. Using this technique, several scan lines are acquired in parallel for each transmitted pulse. This technique is therefore also called parallel beamforming. Although it increases the frame rate in proportion to the number of parallel beams, this technique also introduces block-like artifacts in the B-mode image. These artifacts severely degrade the image quality, and are especially visible in image sequences (movies). An aim of this thesis is to investigate methods to increase the frame rate using parallel beamforming without introducing such image artifacts.

Investigations of the mechanisms of MLA image artifacts have shown that the misalignment of the transmit and receive beams causes distortions to the pulse-echo responses. These distortions result in a shift variant imaging system and image artifacts. This thesis is comprised of four papers that document several metrics that have been developed to evaluate the pulse-echo distortions, image artifacts and shift invariance property. Different methods for artifact reduction have been compared and evaluated. The two methods that have been most thoroughly investigated are steering compensation and the synthetic transmit beam method, STB. In the first method, the receive beams are additionally steered to partially avoid the pulse-echo distortion. Applying this method reduced image artifacts under ideal conditions. However, the performance was heavily reduced in realistic scenarios with aberrations. In the STB method, synthetic transmit beams are created in each receive direction through interpolation. This method performed well both with and without aberrations. Additionally, it has been shown that from the same STB acquisition pattern it is also possible to estimate velocities with an accuracy comparable to that of conventional TDI. This enables higher TDI frame rates or a larger field of view compared to conventional TDI, which requires separate acquisitions for B-mode and tissue Doppler.

# Preface

The present thesis is submitted in partial fulfillment of the requirements for the degree of PhD at the Faculty of Medicine at the Norwegian University of Science and Technology (NTNU). The research was funded by NTNU, and was carried out under the supervision of Professor Hans Torp in the Department of Circulation and Medical Imaging, NTNU.

## Acknowledgments

Several people have been involved in the work presented in this thesis and deserve my gratitude. First of all I would like to thank my supervisor, Professor Hans Torp. His support and guidance throughout this work has been invaluable. He has been available for assistance 24 hours a day, 365 days a year during my time here. Through his profound knowledge of ultrasound, he has always been able to find solutions or good approaches to solve my problems (preferably via a quick K-space analysis of it).

I would also like to thank my colleagues and co-authors Torbjørn Hergum and Svein Arne Aase. Torbjørn had a head start on the STB technique in the autumn of 2003. I joined in during the spring of 2004 as the co-author on the first article on STB. Discussions then and later have been of great importance for my work. Svein Arne has been my roommate during the last few years and co-author on my second and third paper. His efficiency and companionship has been very valuable both for my academic work and for enjoyable days at the office. I further would like to thank all my other colleagues and fellow PhD students in the department. Your social companionship and our technical discussions have made the days at the department fun and inspiring.

I would also like to express my gratitude to the people at GE Vingmed for their help and support with hardware and software. A special thanks goes to my co-supervisor, Kjell Kristoffersen. His broad technical knowledge has been of great help to my work. The Trondheim ultrasound group works in close collaboration with clinicians; through this collaboration I have been given help on clinical issues and have acquired professionally scanned ultrasound images. This has been greatly appreciated.

Finally I would like to thank my dear wife, Karianne, for her encouragement, understanding and love throughout these years.

# Table of Contents

Table of Contents

11

# Chapter 1

# Introduction

Tore Grüner Bjåstad
Dept. Circulation and Medical Imaging, NTNU

Ultrasound imaging is based on a very simple phenomenon that is familiar to most people: the echo. If we shout towards a mountain, the mountain will, after a short time delay, send back the exact same words. Or, stated more scientifically: Sound waves emitted towards a solid object at a right angle will be reflected back to the emitter with a time delay corresponding to the distance back and forth divided by the speed of sound. So if we know the speed of sound and measure the time delay, we can calculate the distance to the reflecting object. After the Titanic went down in 1912, this principle was applied in a patent to detect underwater icebergs [1] and at the end of the First World War, the echo device known as sonar was developed to detect submarines.

Although the principle behind medical ultrasound is the same as for sonar, it is also a bit different. Instead of measuring a single reflection from a solid surface, several small reflections from tissue boundaries are recorded as a sound pulse travels through the body. In the earliest medical ultrasound device, the reflectoscope [2], the amplitudes of these echoes were displayed versus time on an oscilloscope. This type of display came to be known as A-mode, and allowed physicians to get information about the inside of the body without any form of invasive surgery. In 1953, Dr. I. Edler and Professor C. H. Hertz used A-mode to observe heart wall motion [3] and started what later was to be known as "echocardiography."

Since the first A-mode curves on an oscilloscope, medical ultrasound has gone through a vast evolution. Technological advances in electronic circuit design, signal processing, acoustics, materials and software have opened new application areas. Nowadays, ultrasound is a standard tool in many clinical settings. Using ultrasound, clinicians are capable of getting live images of internal organs as well as quantitative information about their function, all of this without any harm to the patient.

Although technological advances continuously push medical ultrasound forward, there are some fundamental physical obstacles that remain. One of them is the speed of sound. This is more or less fixed at 1540 m/s in tissue. Ultrasound images require pulsed transmissions in several scan line directions. Each scan line requires waiting for echoes as the sound propagates through the body, which means that the sound

speed limits how rapidly ultrasound images can be acquired. For an imaging depth of 15cm, each transmitted pulse has to travel 30 cm at 1540 m/s. Hence each ultrasound scan line requires 0.19 ms of acquisition time. A typical 2D ultrasound image is constructed from approximately 100-200 scan lines across an imaging sector. Each ultrasound frame is then recorded in 0.02-0.04 seconds, which corresponds to 25-50 frames per second. This is more than sufficient for imaging slowly moving organs such as the liver or kidney. However, when imaging the heart, the frame rate becomes critical. Twenty-five to 50 frames per second might be sufficient for a qualitative assessment of global heart contraction. However, any quantitative analysis requires a higher frame rate. According to [4] frame rates above 100 hertz are required for accurate quantitative analysis using tissue Doppler. As shown in [5, 6], a heart beat actually contains motion with frequency components of up to 100 hertz. Frame rates above 200 hertz would then be required to accurately capture all of this motion.

High frame rate is thus an important property in cardiac imaging. The example above with 25-50 frames per second was for 2D B-mode imaging. For other modalities, such as color Doppler, or combinations of several modalities, the frame rate might drop significantly (or alternatively, the field of view must be reduced). For 3D imaging, the frame rate becomes even more critical. Here, the ultrasound beams will have to sweep a volume instead of a plane. The number of necessary scan lines is then squared, which may reduce the frame rate to just a couple of frames per second.

Several techniques exist to increase the frame rate of ultrasound imaging. Almost without exception these techniques result in a trade-off in image quality. One commonly used technique to increase frame rate is parallel beamforming [7, 8]. As with other techniques, the straightforward use of this technique results in a noticeable reduction in image quality. Put more precisely, images produced using this technique contain block-like image artifacts. This thesis explores the possibility of using this technique to increase the frame rate of ultrasound imaging, both in B-mode and TDI, and to do so without introducing artifacts in the image.

The thesis is organized as follows. First, background theory on ultrasound acquisition and beamforming is presented. This is followed by a chapter dedicated to frame rate issues. This illuminates the challenges associated with frame rate increase and compares the parallel beamforming method to other common methods for increasing the frame rate. This then leads to the aims of this thesis, summaries of each paper, the thesis discussion and conclusions. Finally, the four papers that comprise this thesis are presented.

## 1.1 Ultrasound data acquisition

### 1.1.1 Scanning modes

Three classical ways of displaying ultrasound echo data are: A-mode, M-mode and B-mode. These are illustrated in Fig. 1.1. Plot a) illustrates A-mode. The echo amplitudes from a single scan line direction are plotted versus depth. The graph is overwritten for each new transmission. Plot b) illustrates M-mode. This scan still
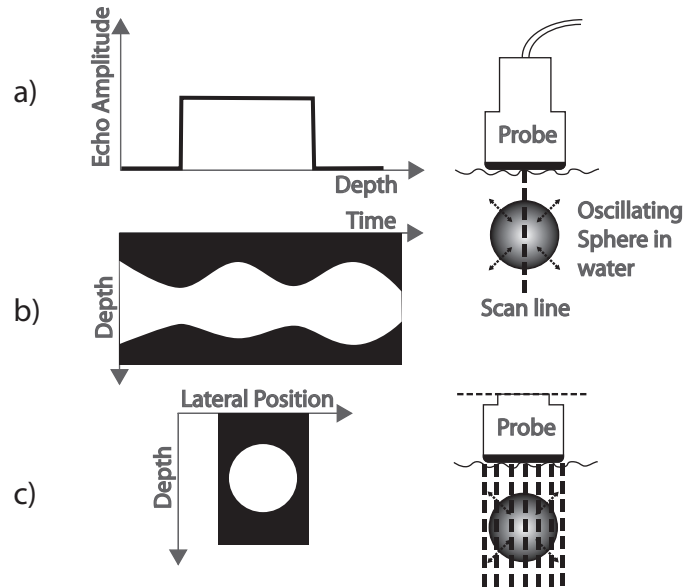
Figure 1.1: Imaging a oscillating sphere with three different scan modes. a) A-mode. Echo amplitude versus depth. b) M-mode. Gray tone coded echo amplitudes, depth versus time of transmission. c) B-mode. Gray tone coded echo amplitudes, depth versus lateral position.

has just one scan line direction, but the depth is now along the vertical axis and the echo amplitudes are plotted as gray tone coded vertical lines in the image. White indicates strong echo and black no echo. The plot is continuously updated with a new vertical line for each new transmission. Hence, the horizontal axis shows the time of each transmission. Plot c) illustrates B-mode (Brightness mode). In this scan type, the echo intensities are also gray tone coded, but the directions of the scan lines are spread out over a sector to create a 2D still image of the object. The image shows depth along the vertical axis and the lateral position of the scan line along the horizontal axis. When doing live scanning, the plot will be continuously updated creating a live movie of the object in the imaging sector.

## 1.1.2 Ultrasound transducer

The device that transmits and receives ultrasound is called a transducer and typically contains one or more piezoelectric elements. A piezoelectric material has the property that it contracts and expands when positive and negative voltages are applied. By applying a voltage alternating with the desired frequency, the piezoelectric elements transform electric energy into acoustic energy and emit ultrasound at the desired frequency.
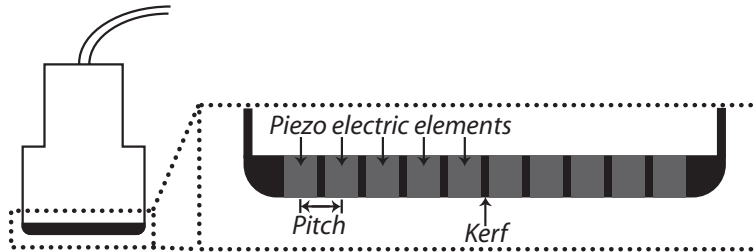
Figure 1.2: Illustration of a medical ultrasound transducer with piezoelectric elements. The number of elements is reduced for illustrational purposes. Typically such a transducer would have more than 100 elements.

Some transducers use only a single element to transmit ultrasound. However, most transducers contain an array of small elements since this provides the greatest flexibility in controlling the radiation pattern (See Fig. 1.2). Since each element is small, they emit spherical sound waves. By controlling the amplitude and delay of the signal for each element, the interference pattern created from all the spherical waves can be controlled. Typically the radiation pattern is formed into a narrow, focused and steered beam of sound.

### 1.1.3 Probe types

Different transducers are used for different applications. The most common transducer types are shown in Fig. 1.3.

The probe in a) is called linear switched array. A linear array is typically quite wide and has large piezoelectric elements. The elements can be large compared to the ultrasound wavelength, since this type of transducer typically does not steer the beam. Each scan line is created from beams pointing straight down from a varying origin on the array. The array is called switched since it uses only a group of elements at one time. The center of this group is slid across the transducer during a scan. A typical application for such a probe is vascular imaging, i.e. imaging arteries and veins.

The probe in b) is called curved array. This type of array works in the same way as a linear array. It is switched and uses a group of elements at a time. But since the surface of the array is curved and each scan line is perpendicular to the surface, this type of probe provides a wider field of view. This is useful in fetal imaging, or when imaging internal organs such as the liver and kidney.

Probe c) in Fig. 1.3 is called a phased array. In such arrays all scan lines typically have a fixed origin on the transducer surface, but are steered in a fan pattern to create the image. These probes are typically smaller than linear and curved linear arrays. The reason for this is that they mostly are used for cardiac imaging where the footprint has to fit between the ribs. Also, the elements of a phased array are smaller than for linear arrays. This allows for larger steering angles without the unwanted interference called grating lobes (Typical element sizes are around half the wavelength).
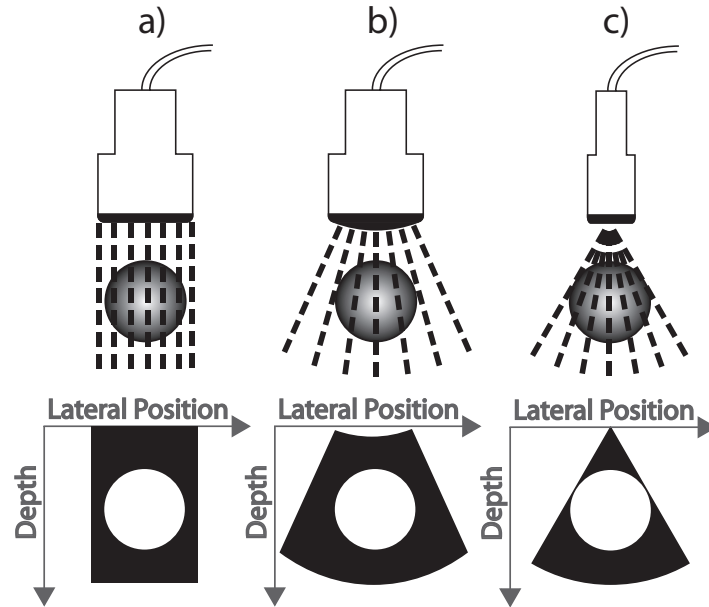
Figure 1.3: The most common probes used in medical ultrasound. a) Linear switched array. b) Linear curved array. c) Phased array.

### 1.1.4   Basic beamforming

An ultrasound B-mode image is constructed from the echo data of beams in several different directions. The term beam means that the ultrasound energy is focused in one specific direction and depth. This is enabled by the subdivision of the transducer into elements. By adding delays to the electrical pulses sent to each element, the radiation pattern can be controlled. This type of beamforming is illustrated in Fig. 1.4.

Plot a) shows the transmit beamforming. A signal generator sends a high frequency pulse to all channels of the system. Each channel has delay circuitry that adds an adjustable delay to the pulse. The delays are chosen so that the ultrasound waves from each element arrive at the focal point simultaneously. This ensures high pressure that gradually builds in the direction of the focal point, and reaches its maximum at this point (approximately). To the sides of the focal point, the ultrasound waves will not be in phase. These locations will thus have lower amplitudes. For some directions, the ultrasound waves will be in opposite phase and add destructively. In these directions the pressure will be zero (approximately).

Plot b) shows the receive beamforming. The principle here is exactly the same, only the process is reversed. A small point scatterer at the focus reflects incoming ultrasound uniformly. These pressure waves propagate to the transducer and are converted to electric signals by the piezoelectric elements. The delays are the same as
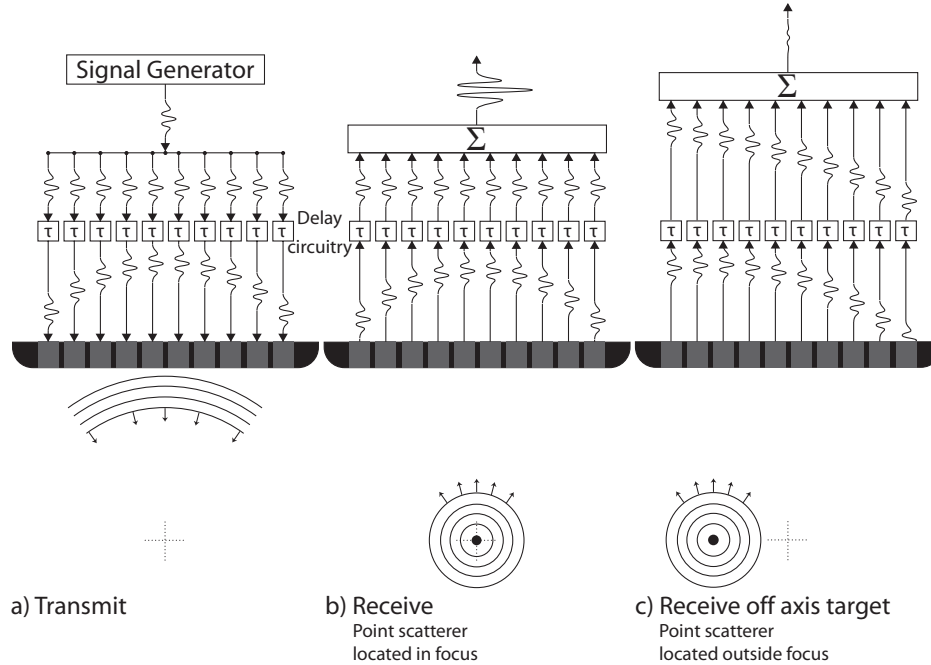
Figure 1.4: Transmit and receive beamforming. For all three illustrations, the transducer is focused at the dotted cross. a) Transmit beamforming. b) Receive beamforming with a point scatterer at the focus point. c) Receive beamforming with a point scatterer located outside the focus point.

when transmitting, and ensure that signals originating from the focal point are aligned. The aligned signals are then summed. Since they all are in phase, the resulting output is amplified.

Plot c) shows what happens if the point scatterer is located outside the focal point. The transducer receive delays are adjusted to amplify signals originating from the focal point. Since this scatterer is located outside, the electrical pulses are not aligned after the delay circuitry. Hence they are summed out of phase, and the resulting output is not amplified (in the illustrated case, the amplitude is actually decreased since the point scatterer is located close to a zero point).

### 1.1.5 Beam profiles

The transducer radiation pattern can be described using beam profiles. The top left plot in Fig. 1.5 shows the pressure pulse measured along an equidistant arc at the focal range (with time along the vertical axis and azimuth angle along the horizontal axis). The corresponding beam profile shows the lateral energy distribution, and is calculated as the mean square value of the pressure. In most cases the beam profiles
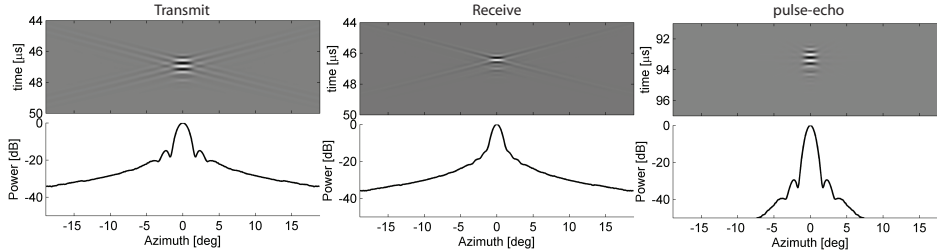
Figure 1.5: Beam profiles. Top figure row shows transducer responses along an arc at the focal range. Bottom rows show the corresponding beam profiles. The left plots shows the response and beam profile of the transmit aperture. The middle plots show the receive response and beam profile. The right plots show the pulse-echo response and beam profile.

are displayed in logarithmic scale. The central part of the beam profile is referred to as the main lobe. The parts of the beam profile outside the first zeros are referred to as the side lobes.

The top middle plot of Fig. 1.5 shows the receive response of the transducer at the focal range. This corresponds to the signal received by this scan line from a point source emitting a spherical delta pulse located at focal range and at the angles specified by the horizontal axis. Since receiving is a passive process, the receive beam profile maps the receive angle sensitivity instead of pressure.

The focal range pulse-echo response of the transducer is shown in the right plot of Fig. 1.5. This corresponds to the signal received by this scan line when imaging (transmitting and receiving) a point scatterer located at focal range and at the angles specified by the horizontal axis. Pulse-echo beam profiles thus show from which spatial extent scan lines get their echo data. Knowing the transmit and receive response, the pulse-echo response can be found from the temporal convolution between these two. The pulse-echo response is also referred to as the two-way response.

Fig. 1.5 only shows the beam profiles in the azimuth plane. Similar plots could also be made to describe the transducer sensitivity in the elevation plane.

The beam profiles in Fig. 1.5 show beam profiles at a single range, the focal range. The left plot of Fig. 1.6 shows gray tone coded transmit beam profiles for all depths from 0 to 120 mm. Such plots illustrate how the radiation field concentrates towards the focal depth. The right plot shows the intensity along the beam axis. Such plots are referred to as range profiles, and show how the pressure (or sensitivity) builds up towards the focus, and decays after.

The beam width $D_F$, indicated in the left plot of Fig. 1.6 is calculated as [9]:

$$D_F = F_\# \lambda, \tag{1.1}$$

$$F_\# = \frac{F}{a} \tag{1.2}$$
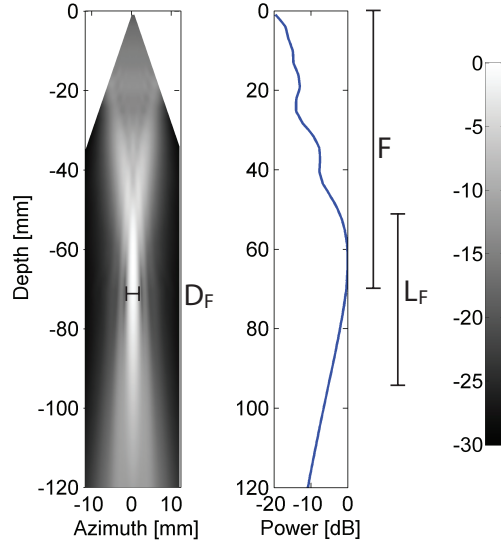
Figure 1.6: Transmit beam profiles versus depth. Left plot shows an image of the transmit beam profiles from depths 0 to 120 mm. The right plot shows the range profile, which is the intensity along the center axis of the beam.

where $\lambda$ is the wavelength, $F$ is the focal distance and $a$ is the aperture width. This is the continuous wave beam width that follows from the Fraunhofer approximation, but inserting the center wavelength of the imaging pulse is a good approximation for the pulsed wave case.

The depth of focus, $L_F$ (indicated in the figure) is the range span where the beam width is approximately constant around the focal distance. $L_F$ is given by [9]:

$$L_F = 2 \cdot \lambda F_\#^2, \tag{1.3}$$

### 1.1.6 Common beamforming techniques

Receive focusing can be done in a more optimal way than the transmit focusing. Since the receive array only is listening, it can adjust the focus to follow the transmitted pulse. This technique is called dynamic focusing. The resulting beam profiles are shown in the left plot of Fig. 1.7. A narrow focus is maintained through the whole length of the beam. The right image of Fig. 1.7 shows the two-way beam. Due to the dynamic receive focusing, the beam remains reasonably concentrated throughout the length of the beam.

To keep the side lobes down, a weighting function can be applied to the signal to/from each transducer element. This is called apodization, and is illustrated in Fig. 1.8. Due to a simpler implementation, it is most common to use apodization on receive. The resulting beam profiles with and without receive apodization are shown
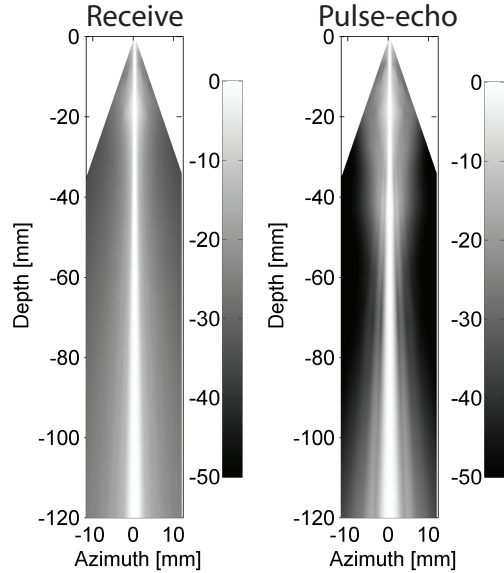
Figure 1.7: Receive and two-way beam profiles plotted versus depth. The beam profiles are normalized to maximum intensity at all depths. Notice that the dB scale is different for the receive and two-way plots.

in the left and middle plots of Fig. 1.8. One can clearly see that the side lobe levels are decreased. The disadvantage is that the main lobe width is increased, reducing the lateral resolution.

In the middle plot of Fig. 1.8 the beam width changes with distance from the transducer. This is not always desirable since it results in non-uniform resolution throughout the image. Eq. 1.1 shows that the resolution can be kept constant by keeping $F_{\#}$ constant. This can be achieved by expanding the aperture as the focus follows the pulse. The technique is therefore called expanding aperture. The right plot of Fig. 1.8 shows that this keeps the beam width constant until the aperture is expanded to its maximum (at 7 cm in this case).

### 1.1.7 Image Quality

The ultrasound image quality is dependent on several factors, some of which can be controlled by changing parameters, and some of which are beyond control due to the propagating medium. Most of the imaging qualities of a transducer can be found from considering its point spread function (PSF). The PSF shows how the imaging system images a single point scatterer. A simulated PSF in the focal point of a phased array is shown in Fig. 1.9. The dimensions of the PSF determine the spatial resolution of the system. The spatial resolution is defined as the smallest distance between two targets before the imaging system cannot resolve them anymore. In the lateral direction

21
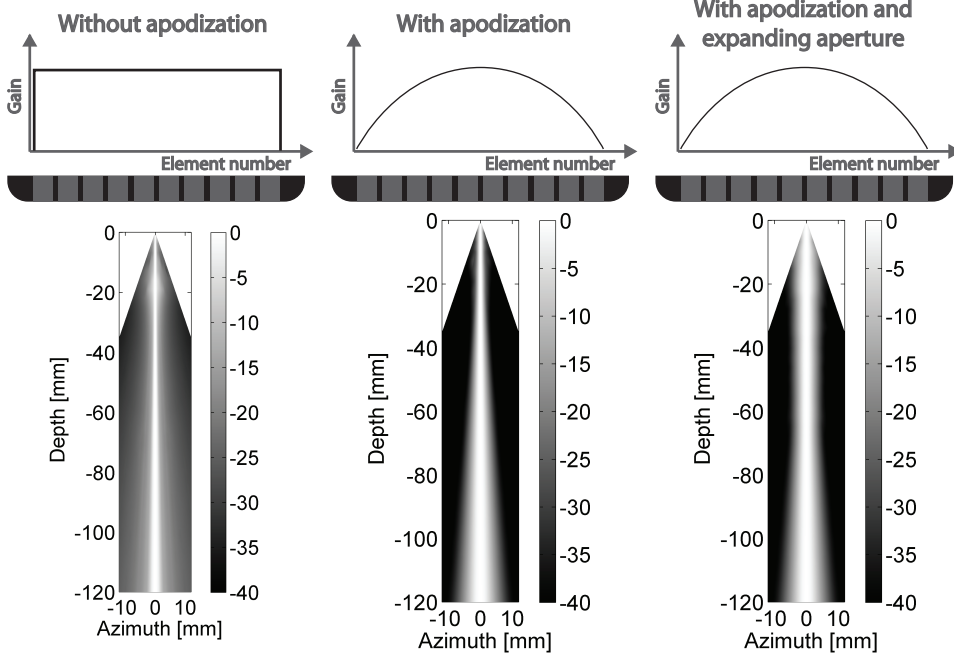
Figure 1.8: Receive apodization and expanding aperture. The top image row shows the aperture and its weighting function. The bottom image row shows the resulting receive beams. The figure to the left shows the receive beam from using dynamic receive focusing without apodization (identical to the two-way beam shown in Fig. 1.7, but with a slightly different dynamic range). The middle plot shows the resulting receive beam from applying receive apodization. The right plot shows the receive beam from applying both receive apodization and expanding aperture.

(normal to the beam direction) the resolution is given by:

$$\Delta x = \frac{\lambda F}{a_{tx} + a_{rx}}, \tag{1.4}$$

where F is the focal range, $\lambda$ is the center wavelength of the imaging pulse and $a_{tx}$ and $a_{rx}$ are the size of the transmit and receive apertures. This equation is similar to Eq. 1.1, except that $a$ is replaced with the two-way aperture, $a_{tx} + a_{rx}$, to get the actual imaging resolution. The radial resolution depends on the pulse length, and is given by:

$$\Delta r = \frac{c \cdot T_{pulse}}{2} = \frac{c}{2 \cdot B_{pulse}}, \tag{1.5}$$

where $c$ is the speed of sound, $T_{pulse}$ is the pulse length, and $B_{pulse}$ is the frequency bandwidth of the pulse.
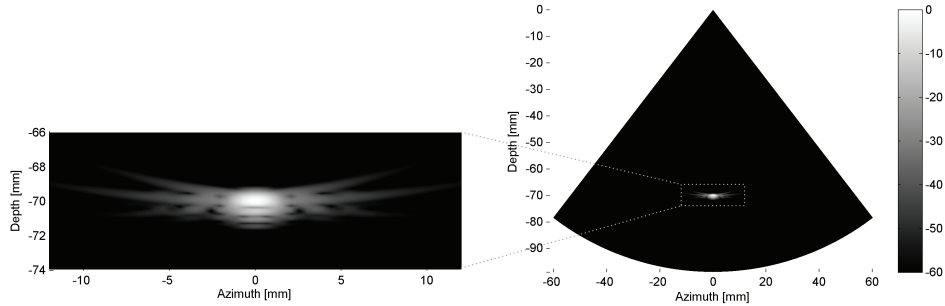
Figure 1.9: The point spread function of an imaging system. The left plot shows the PSF, and the right plot shows the location of the PSF in the field of view.

The image quality is also dependent on the contrast resolution of the system. The contrast resolution is a measure of how well the imaging system can differentiate between two regions with different scattering properties. An example could be an echo-free cyst embedded in tissue. Contrast resolution is determined by the side lobe level of the PSF.
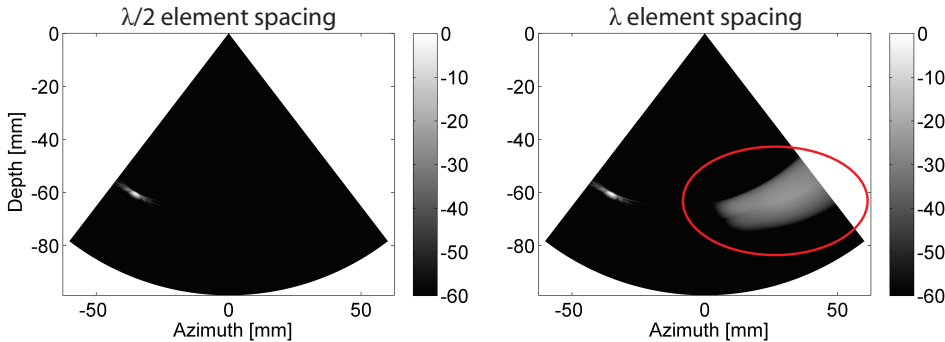


Figure 1.10: Grating lobes. The image to the left shows the image of a point scatterer imaged with a $\lambda/2$ pitch array. The image to the right shows the same point scatterer imaged with a $\lambda$ pitch array. For the latter case, the large element spacing results in grating lobes when the beams are steered. The scan lines to the far right of the image thus pick up the point scatterer to the far left in their grating lobes. This causes the cloud emphasized with a surrounding oval in the image. Notice that the dB scale is larger than the normal 40dB. This was done deliberately to emphasize the effect of grating lobes.

Another type of side lobe that reduces the contrast resolution is grating lobes. Grating lobes are strong distant side lobes that appear if the pitch is too large compared to the wavelength. A comparison between PSFs from arrays with pitch $\lambda/2$ and $\lambda$ is shown in Fig. 1.10. The point scatterer located to the left is picked up

in the grating lobes of the scan lines to the right in the image.

### 1.1.8 Shift invariance

Shift invariance is an important property for an imaging system. In a shift invariant imaging system, the image of an object is independent of the object position relative to the imaging aperture; i.e., the appearance of an object should not change when an object moves. Hence, in a shift invariant imaging system, the PSF is identical at all positions.

A conventional ultrasound system will not be globally shift invariant. Due to focusing and steering, the PSF will slowly vary with position throughout the image. For the image quality of an ultrasound imaging system, it is most important with local shift invariance; i.e., the PSF should be constant over smaller areas of the imaging sector. This is important for object motion to be perceived correctly in image sequences.

### 1.1.9 Body wall distortion effects

The beamforming delays are adjusted to ensure that the ultrasound waves from all elements arrive at the focal point at the same time. It is then assumed that the propagation velocity is constant. This is not the case when imaging through the body wall. The ultrasound waves propagate through fat, muscle, blood and connective tissue, which all have different speeds of sound. This causes distortions to the ultrasound wave front, which are referred to as aberrations. These distortions typically reduce the focusing effect and result in a lower main lobe level and reduced contrast resolution.

Another beamforming assumption is that the ultrasound pulse is reflected only one time. In practice, the pulse is reflected several times between tissue layers before returning to the transducer. The increased propagation time of echoes reflected multiple times will make them arrive simultaneously with direct echoes from more distant locations, which combined reduce the contrast resolution. Multiple reflections are also called reverberations and are especially visible in the near field due to the layered structure of the tissue close to the skin. Here they appear as a haze over the imaged structures.

### 1.1.10 Biomechanical effects of ultrasound

If applied with enough power, ultrasound waves can be harmful. An example is the therapeutic ultrasound that is used to shatter kidney stones. Another example is high-intensity focused ultrasound, HIFU. HIFU can be used to perform surgery inside the body, specifically to produce highly localized lesions.

There are two biomechanical effects of transmitting ultrasound into tissue. The first effect is a temperature increase. The energy from ultrasound is absorbed by the tissue as heat. The temperature increase from ultrasound exposure is described by

the thermal index, TI [10]:

$$TI = \frac{W_0}{W_{deg}}, \tag{1.6}$$

where $W_0$ is the time-averaged acoustic power of the source (or another power parameter), and $W_{deg}$ is the power necessary to raise the target temperature by 1°C based on specific thermal and tissue models.

The second biomechanical effect is cavitation. Cavitation is the creation of gas bubbles in the tissue. This can occur if the peak negative pressure of the ultrasound pulse is too high. The mechanical index, MI, is an estimate of the likelihood of cavitation, and is given by [10]:

$$MI = \frac{P_{r.3}}{\sqrt{f_c}}, \tag{1.7}$$

where $P_{r.3}$ is a measure of the peak negative pressure and $f_c$ the center frequency of the imaging pulse (See [10] for details).

From an image quality point of view, it would be beneficial to use a high transmit power. This would increase the penetration and increase the signal-to-noise ratio of the received signal. However, to avoid harmful biomechanical effects, the maximum allowed MI and TI for ultrasound equipment used for medical imaging are under strict regulations.

### 1.1.11 Sampling

To be able to perfectly reconstruct a sampled signal, the Nyquist sampling theorem states that the sampling frequency must be at least twice the highest frequency component in the signal. This puts constraints on the sampling frequency when digitalizing the received ultrasound echoes, but it also puts constraints on the spacing between the ultrasound beams. From the Fraunhofer approximation, it follows that the Fourier transform of a continuous wave ultrasound field in focus is given by the aperture shape and size, and the wavelength. This gives us the lateral bandwidth of each frequency component in pulsed wave transmission and the following Nyquist beam spacing requirements for transmit and two-way beams (in radians):

$$\delta\theta_{nq}^{t} = \frac{\lambda}{a_{tx}}, \tag{1.8}$$

$$\delta\theta_{nq}^{tr} = \frac{\lambda}{a_{tx} + a_{rx}}, \tag{1.9}$$

where $\lambda$ is the wavelength and $a_{tx}$ and $a_{rx}$ are the transmit and receive aperture sizes. To achieve lossless insonification and sampling of an object, both these constraints must be met. If not, azimuthal information will be lost, and the resulting image will contain aliasing artifacts. The typical indication of under sampling and aliasing is that the imaging system becomes locally shift variant, i.e. the PSF varies with small changes in position.

A sufficiently sampled image of a point scatterer (i.e. the PSF) and its corresponding frequency transform are shown in Fig. 1.11. The maximum and minimum lateral frequencies for this pulse's temporal center frequency are indicated by two thin dotted lines. The corresponding lateral frequencies given in $1/rad$ are stated above the lines. Sampling at twice this frequency results in the beam spacing given by Eq. 1.9. This equals the equation for imaging resolution stated in Eq. 1.4 divided by $F$. This difference is only due to conversion between radians and meters. The Nyquist beam spacing requirements in meters can be found from multiplying Eq. 1.8 and 1.9 with $F$, the focal range.



PSF spatial domain    PSF frequency domain
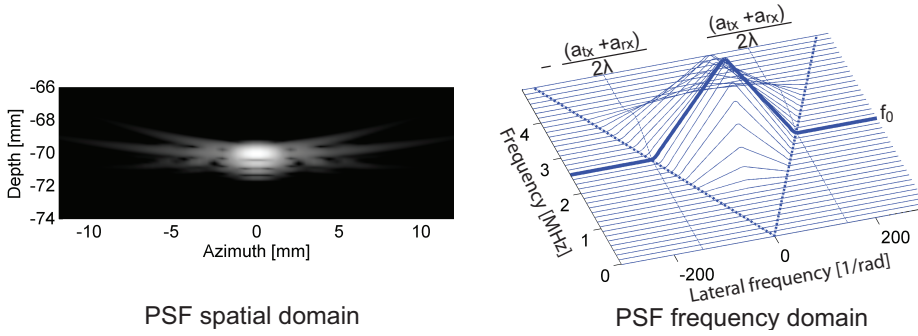
Figure 1.11: PSF shown in spatial domain to the left and frequency domain to the right. The thick solid line shows the lateral frequency content at the center frequency of imaging pulse. The thick dotted lines indicate maximum lateral frequency components for all temporal frequencies. The thin dotted lines indicate maximum lateral frequency components of the center frequency (The formula for this value is stated above the line)

## 1.2 Frame Rate

The frame rate of an imaging system determines how well it can capture rapid object motion. For slow moving organs such as the liver or kidney, the frame rate is not very important. To capture the motion of the heart or blood flow, on the other hand, a high frame rate is very important.

The fundamental physical factor that limits the frame rate of ultrasound imaging is the speed of sound, $c$. An ultrasound image is typically constructed from several scan lines in different directions. For each of these scan lines an imaging pulse has to travel to the maximum imaging depth, $R$, and back. This gives us the acquisition time for a single scan line:

$$T_{sl} = \frac{2R}{c}, \tag{1.10}$$

The acquisition time for a frame of $N_{sl}$ scan lines then becomes:

$$T_{fr} = T_{sl} \cdot N_{sl} = \frac{2R}{c} \cdot N_{sl}. \tag{1.11}$$

Assuming an equal transmit and receive aperture, $a_{tx} = a_{rx}$, transmit sampling criterion will be satisfied when the two-way criterion is satisfied (Eq. 1.9). The number of scan lines, $N_{sln}$, necessary to sufficiently sample a sector $\phi$ (in radians) then becomes:

$$N_{sln} = \frac{\phi}{\delta\theta_{nq}^{tr}} = \frac{\phi \cdot (a_{tx} + a_{rx})}{\lambda}. \tag{1.12}$$

Before the ultrasound echoes are displayed as gray tone coded B-mode, the echoes will be detected (squared value of the envelope) and log-compressed. This process effectively doubles the lateral bandwidth of the echo data. To avoid aliasing from this process, one will have to acquire twice the number of scan lines, $N_{sln}$, stated in Eq. 1.12. Inverting Eq. 1.11 and inserting $2 \cdot N_{sln}$ for $N_{sl}$ then gives us the maximum frame rate of a sufficiently sampled image scan:

$$f_{fr} = \frac{1}{T_{fr}} = \frac{1}{2 \cdot N_{sln} \cdot T_{sl}} = \frac{c\lambda}{4R\phi \cdot (a_{tx} + a_{rx})}. \tag{1.13}$$

If inserting typical cardiac parameters ($c = 1540m/s, f0 = 2.5MHz, \lambda = c/f0 = 0.616mm, R = 15cm, \phi = 75deg, a_{tx} = 2cm, a_{rx} = 2cm$), the resulting frame rate from this formula will be 30 frames per second.

The following sections review selected methods for increasing the frame rate.

### 1.2.1   IQ interpolation

In the term IQ data, the "I" stands for in phase, and "Q" for quadrature. The IQ ultrasound data is simply the complex base band version of the echo data, i.e., the received echo data demodulated and bandpass filtered (without any loss of information). This is a commonly used and convenient format for further processing of the ultrasound data.

The concept of IQ interpolation is to double (or more) the amount of scan lines before the detection stage. By doing this, the echo data will also be sufficiently sampled after the lateral bandwidth doubling in the detection stage. This way, the $N_{sln}$ scan lines of Eq. 1.12 will be sufficient, resulting in a doubling of the frame rate in Eq. 1.13.

However, since the interpolation is done coherently, IQ interpolation will be sensitive to motion. If the object has moved sufficiently in the time span between two neighboring scan lines, these two scan lines can in the worst case be out of phase. This would result in the interpolated scan line amplitude being zero. For less motion, the amplitude of the interpolated scan lines will be reduced. Due to this, IQ interpolation and object motion can lead to artifacts in the B-mode images.
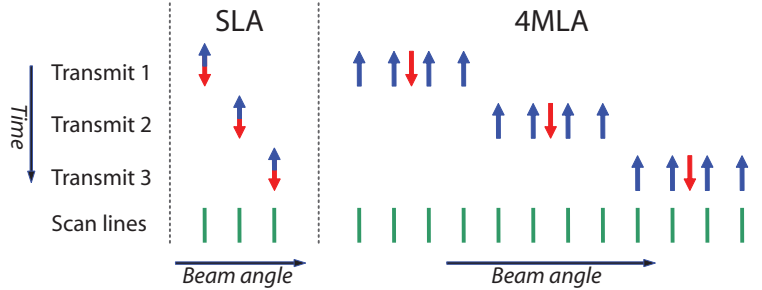
Figure 1.12: Comparison of single line acquisition, SLA, and multiple line acquisition, MLA. SLA is shown to the left, MLA to the right. Down arrows indicate transmit direction and up arrows receive directions. For SLA, transmit and receive directions are identical. The resulting scan line directions are indicated with lines at the bottom of the illustration.

## 1.2.2 Multiple Line Acquisition, MLA

The concept of MLA is to acquire more than one scan line for each transmit event [7, 8]. This is also called parallel beamforming (multiple parallel receive beams for each transmit beam). This allows for fewer transmit events with the same amount of scan lines. The concept is illustrated for four parallel beams, 4MLA, in Fig. 1.12. The potential frame rate increase compared to conventional single line acquisition, SLA, is equal to the number of parallel beams.

Using this technique, a frame could theoretically be acquired from one transmit pulse illuminating the whole object and beamform in all receive directions at once. However, there are several reasons why this is not an especially good idea:

1. Reduced image resolution. To illuminate the whole object with a single pulse, the transmit beam would have to be wide. This corresponds to using a very small transmit aperture. From Eq. 1.4, one can see that the resolution then is reduced to the resolving power of the receive beam alone ($\lambda F/a_{rx}$).

2. Higher side lobes. The resulting two-way side lobe level will be identical to the side lobe level of the receive beam alone (-14dB). The side lobes of a normal two-way beam are located 28 dB below the main lobe level (See Fig. 1.5). This results in a heavily reduced contrast resolution. Applying receive apodization could compensate for this, but that would reduce the resolution further.

3. Reduced penetration. Transmitting an unfocused pulse instead of a focused pulse reduces the allowed transmit power according to the maximum limit for the mechanical index, MI. The MI limit is calculated from maximum axial pressure, and while a focused transmit pulse has its maximum deep in the tissue, an unfocused transmit pulse has its maximum at the transducer surface. Hence, the signal-to-noise ratio will be much poorer in the lower parts of the ultrasound image using an unfocused transmit pulse than a focused transmit pulse.

4. Increased hardware requirements. Beamforming all receive beams real time for each transmit event puts high requirements on the hardware.

From this it can be concluded that it is beneficial to generate transmit beams that are as focused as possible for maximum image quality.

When applying MLA to reduce the number of transmit beams, the transmit aperture, $a_{tx}$, must be adjusted to satisfy the Nyquist transmit beam spacing requirements stated in Eq. 1.8. The first paper in this thesis presents an equation for the necessary number of parallel beams given Nyquist oversampling factors $p^t$ and $p^{tr}$ for the transmit and two-way beam spacing. For transmit and receive apertures $a_{tx}$ and $a_{rx}$ this relation is given by:

$$N_{mlaN} = \frac{p^t}{p^{tr}} \cdot (1 + \frac{a_{rx}}{a_{tx}}).  \tag{1.14}$$

This equation shows that for two parallel beams and marginal sampling ($p^t = p^{tr} = 1$), no reduction in transmit aperture is required, resulting in twice the frame rate without loss in image resolution, contrast resolution or penetration. However, using four parallel beams and marginal sampling (i.e. a fourfold increase in frame rate), the transmit aperture will have to be reduced to $1/3$ of the receive aperture. The image quality will then start to suffer from the three first issues listed above.

It can be mentioned here that Eq. 1.14 assumes that IQ interpolation is used to avoid aliasing from the detection stage. If not, $N_{mlaN}$ should be multiplied by a factor of two. Using four parallel beams without IQ interpolation could then give a frame rate four times higher than that of the SLA case in Eq. 1.13 without having to reduce the transmit aperture. By doing this, one also avoids the potential problem of motion artifacts using IQ interpolation.

The main problem resulting from applying parallel beamforming is, however, the block-like artifacts in the B-mode image. The mechanisms of these artifacts will be discussed in chapter 1.3.

### 1.2.3   Multiple Line Transmission, MLT

The concept behind MLT is to transmit in several directions simultaneously. As is shown in Fig. 1.13, this technique can be combined with MLA to also acquire multiple scan lines for each transmit beam. For the case shown to the right in the figure, the number of transmit events is reduced by a factor of four compared to conventional SLA.

An advantage of MLT is an even higher achievable frame rate before the transmit aperture has to be reduced. According to Eq. 1.14, the frame rate can be increased by a factor of two times the number of parallel transmit beams without reductions to the transmit aperture when combined with 2MLA. Alternatively, a factor four times the number of parallel transmit beams if IQ interpolation is not used.

A disadvantage of MLT is the crosstalk between the parallel transmit beams. The crosstalk can be split into two types, as illustrated in Fig. 1.14. The first type is transmit crosstalk. This is energy from the side lobe of the first transmit direction
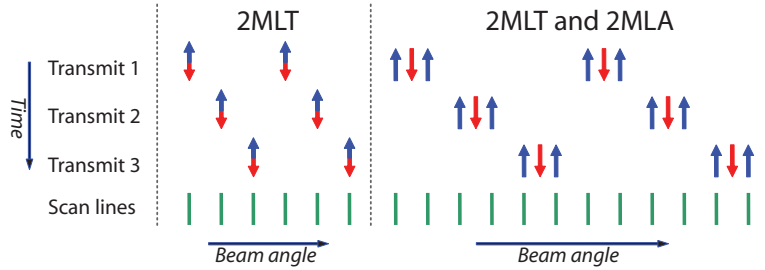
Figure 1.13: Illustration of multiple line transmission, MLT. 2MLT with one receive beam per transmit beam is shown to the left and 2MLT with two receive beams per transmit beam to the right. Down arrows indicate transmit direction and up arrows receive directions. The resulting scan line directions are indicated with lines at the bottom of the image.
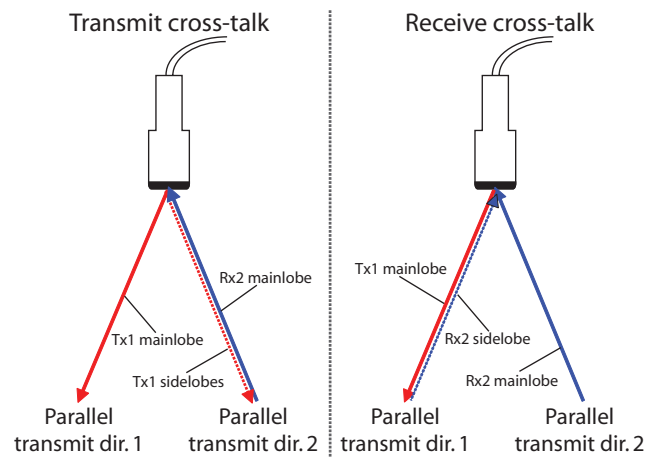


Figure 1.14: Illustration of MLT crosstalk. Parallel transmit beams are named Tx1 and Tx2. Corresponding receive beams are named Rx1 and Rx2. The illustration to the left shows transmit crosstalk: Transmitted side lobe energy from the first MLT transmit direction is picked up in the receive beam of the second transmit direction. The illustration to the right shows receive crosstalk: Transmitted main lobe energy from the first MLT transmit direction is picked up in the side lobe of the receive beam of the second MLT transmit direction.

that is picked up in the main lobe of the receive beams of the second transmit direction (to the left in Fig. 1.14). The second type is receive crosstalk. This is energy from the main lobe of the first transmit direction picked up in the side lobes of the receive beams of the second transmit direction (illustrated to the right in Fig. 1.14). The effect of the two types of crosstalk from imaging a single point scatterer can be seen in Fig. 1.15. Obviously, the amount of crosstalk will be dependant on the separation

between the parallel transmit directions. Hence, they should be separated as much as possible. To reduce the transmit crosstalk further, apodization can be applied to the transmit aperture. Likewise, the receive crosstalk can be reduced by applying apodization to the receive aperture. Another method to reduce crosstalk is to apply coded excitation with a different code for each parallel transmit direction [11].
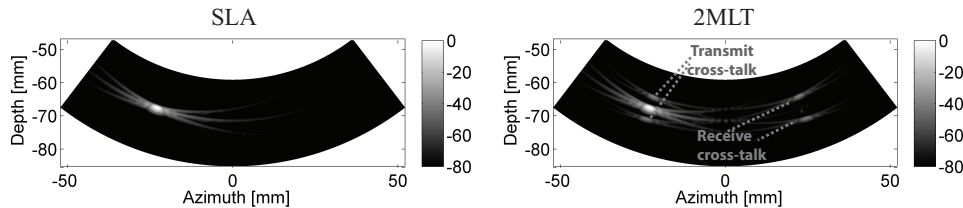


Figure 1.15: MLT crosstalk when imaging a single point scatterer. Single line acquisition is shown to the left and 2MLT to the right (two parallel transmit beams). The effects of transmit and receive crosstalk is indicated in the figure. A large dynamic range (80 dB) was used for illustrational purposes.

### 1.2.4   Synthetic Aperture

Synthetic aperture (SA) imaging was originally developed for radar applications back in the 1950s. The main concept is to construct a large aperture from several transmits with a small aperture at different aperture positions. The principles of medical SA imaging are illustrated in Fig. 1.16. Several low-resolution images are created by transmitting at each element sequentially, and for each of these transmits, beamforming the whole ultrasound image. These low-resolution images can be combined coherently into a single high-resolution image. Since the response from all elements to all elements is known, it is possible to do transmit focusing at all depths of this high-resolution image; in other words, dynamic focusing can be done both on transmit and receive. In a real time implementation, the high-resolution image would constantly be updated with new low-resolution images in exchange for old low-resolution images. This would allow frame rates equal to the pulse repetition time of the system. However, only one of the low-resolution images contributing to the high-resolution image is updated at this rate. To increase the signal-to-noise ratio, it is common to implement SA with groups of elements that emulate radiation from a single element. More on synthetic aperture imaging can be found in [13]

One of the problems with SA is the computational cost. Implementing the technique in real time puts very high requirements on the hardware capabilities. However, a full scale system for doing this is currently in development at DTU in Denmark [14].

Another problem with this technique, as with all techniques where coherent combinations are made from several transmits, is motion artifacts. Each high-resolution image is a coherent combination of low-resolution images from several transmits. Motion within in the time span of the low-resolution transmits will cause
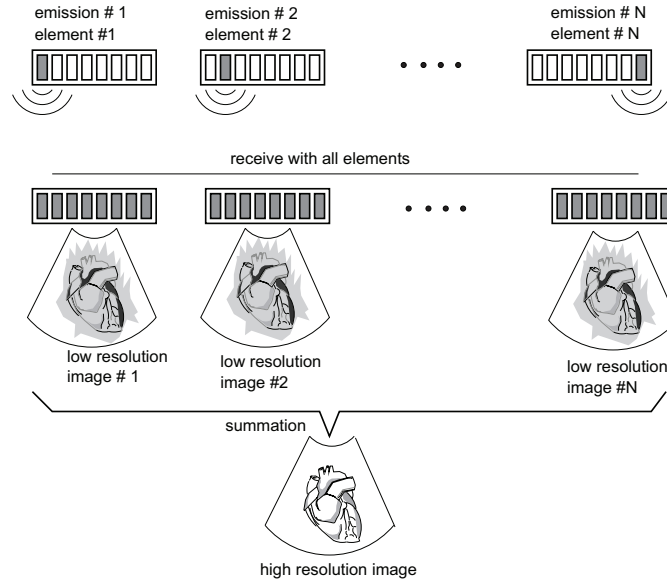
Figure 1.16: Illustration of the basic principles of synthetic aperture in medical ultrasound imaging. Several low-resolution images are created from transmitting sequentially at each element and receiving at all elements. When low-resolution images for all elements are acquired, these are coherently combined into a high-resolution image. The illustration is acquired from [12], and is printed with permission from the author.

motion artifacts in the final high-resolution image. More on SA motion artifacts and compensation can be found in [15–18].

### 1.2.5 High frame rate using limited diffraction beams

This technique is described in [19]. The concept is to transmit and receive using limited diffraction beams. Theoretically, the limited diffraction beam type has the property that it can propagate to infinite distance without changing its transverse beam patterns. However, for a practical finite-aperture radiator, it merely has a large depth of field compared to a conventional spherically focused beam [20, 21]. The use of limited diffraction beams instead of diverging waves, as in SA, has the advantage of higher SNR. Using this technique, an image can be created from a single transmit. However, to achieve a wider field of view, limited diffraction beams will have to be transmitted in several directions. Combining data from overlapping transmit beams also allows for dynamic transmit focusing, which improves spatial and contrast resolution.

Another aspect of the method is that the image formation is done in the spatial Fourier domain instead of traditional delay and sum beamforming. The final image is

created from an inverse Fourier transform.

At the cost of reduced lateral resolution, it is also possible to transmit plane waves instead of limited diffraction beams [22].

## 1.3 MLA artifacts
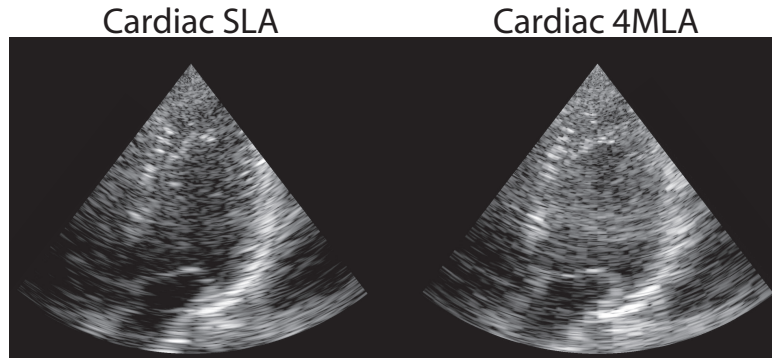


Figure 1.17: Example of B-mode image artifacts resulting from the use of MLA in imaging the left ventricle of the heart. The B-mode image to the left was acquired using conventional SLA, while the image to the right was acquired using 4MLA. The last image can clearly be seen to contain lateral block-like artifacts, especially in the bottom right corner of the image. Images are acquired from the second paper of this thesis.

As mention in Chapter 1.2.2, the main problem of applying multiple line acquisition (MLA) is that it results in image artifacts. As can be seen from Fig. 1.17, these artifacts are manifested as lateral blocks or discontinuities in the image. Although the mechanisms that cause these artifacts are described in the papers of this thesis, a short explanation will be given in this chapter.

The fundamental cause of the artifacts is that the receive directions are offset from the transmit directions. Due to these offsets, the two-way beams become distorted. These distortions are split into three. The first distortion is called warping. This is the two-way beam being pulled towards the transmit beam direction (illustrated in the top plot of Fig. 1.18). The two-way response comes from the radial convolution of the transmit and receive response. The two-way beam profile can be approximated as the product between the transmit and receive beam profile. As can be seen from the top plot in Fig. 1.18, the resulting solid line two-way beam profile is placed closer to the transmit direction than the dotted line receive beam profile. The strength of the warping will also vary by depth. This is illustrated in the bottom plot of Fig. 1.18. This shows a trace of the two-way beam maximum versus depth for six neighboring 2MLA beams. The two-way beams clearly follow curved paths instead of straight lines, as would be the case with SLA. Typically the warping is strongest at the focal depth,
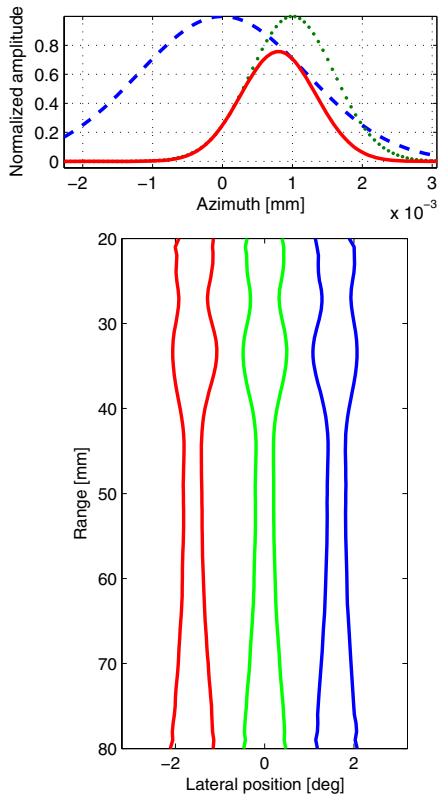
Figure 1.18: Illustration of the warping effect of MLA imaging. Top figure shows the mechanisms of warping. The interaction between the transmit beam (dashed line) and the receive beam (dotted line) results in a two-way beam (solid line) with a maximum closer to the transmit beam than the receive beam. The bottom plot shows the depth variation of the warping. Each line shows the trace of a two-way beam in a 2MLA scan. Lines for three neighboring transmit events and thus six neighboring two-way beams are plotted.

since this is where the transmit beam is most tightly focused. This leads to large gaps between neighboring MLA groups, so that imaged objects become irregularly sampled.

The second distortion type is called skewing. This is the two-way beam profile becoming asymmetrical. Skewing is illustrated in Fig. 1.19. The interaction between the transmit and receive beam weights the receive side lobes on each side differently, resulting in an asymmetric two-way beam profile. Since this in effect results in a beam that is more sensitive on one side than on the other, this distortion will also contribute to an irregular sampling of the imaged object.

A third distortion from the transmit-receive offset is that the gain of the two-way beam is reduced (See Fig. 1.18). This gain reduction increases with offset distance

34
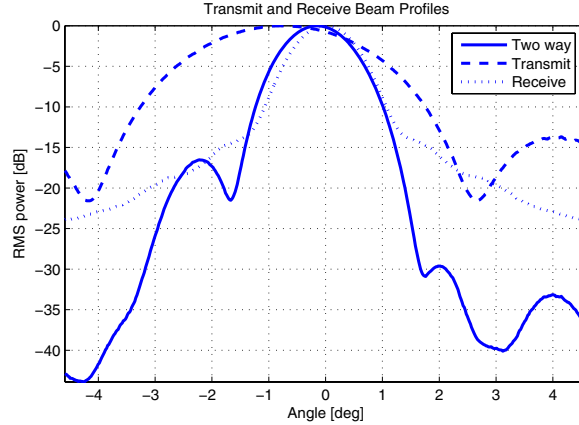
Figure 1.19: Illustration of the skewing effect using MLA. The interaction between the transmit beam (dashed line) and the offset receive beam (dotted line) results in an asymmetrical two-way beam profile (solid line).

and results in a lateral gain modulation in the B-mode image (when imaging with more than two parallel beams).

Techniques to compensate for these parallel beamforming artifacts have previously been proposed by others [23–29]. A common factor among all these proposals is that they are contained in commercial patents and not in academic papers. As patents are only designed to describe techniques, the information provided offers little insight into the actual performance. Performance evaluations of several compensation techniques will be presented in the papers of this thesis.

## 1.4 Tissue Doppler Imaging

Tissue Doppler imaging, TDI, is an imaging modality that estimates tissue velocities. It was first introduced by McDicken et al. in 1992 [30]. Since then, TDI has become a common imaging modality among cardiologists since it enables quantitative evaluation of cardiac tissue function.

The principles of TDI are similar to those of Color Flow imaging [31]. Several pulses are transmitted in each direction, and the phase shifts between the receive data are calculated to estimate motion (See Fig. 1.20). The autocorrelation method [32] is most commonly used to estimate the phase shift.

It is common to also acquire B-mode images along with the tissue Doppler images. These images are combined into a single color-coded image displaying both tissue intensity and tissue velocities. Due to rapid tissue deformation, frame rates above 100 Hz are desired in cardiac TDI [4]. There are two factors limiting the TDI frame rate. The first is that tissue Doppler data require several transmissions in each direction. For the case illustrated in Fig. 1.20, two transmits are used in each direction. This
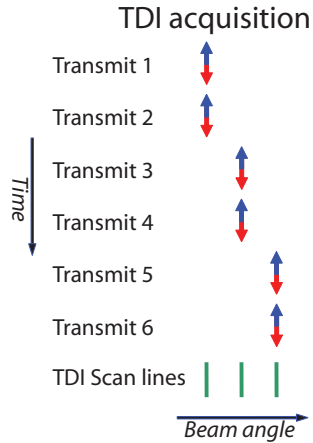
Figure 1.20: Illustration of the TDI acquisition pattern. For each scan line direction, two or more pulses are transmitted in each direction. The lines with arrows on both ends indicate transmit and receive in the same direction. The TDI scan line directions are indicated with solid lines at the bottom of the figure.

would reduce the frame rate by a factor of two compared to the B-mode SLA case shown to the left in Fig. 1.12. The number of transmits in each direction could also be greater than two. This would result in an even larger drop in the frame rate. The second factor is that the B-mode images require a separate acquisition in addition to the tissue Doppler acquisition.

A common way to compensate for these frame rate reducing factors is to reduce the field of view. This, however, is not always desirable. An example is when studying asynchrony between cardiac walls. It is then desirable to capture both cardiac walls within one sector, something that requires a large field of view (approximately 60 degrees sector width).

Another common way to increase TDI frame rate is to increase the beam width. This allows for fewer transmit beams, and thus a higher frame rate. It does, however, also reduce the penetration and lateral resolution.

In previous work, it has been suggested that the overall TDI frame rate be increased by separately decreasing the B-mode frame rate [33]. For example, one B-mode frame for every second Doppler frame would be one possible approach. This does result in a lower B-mode temporal resolution, however, and a temporal mismatch between the displayed B-mode image and the overlaid velocities.

Another proposal is presented in [34], which describes a method for continuous acquisition high frame rate tissue Doppler. The velocities are then estimated from phase shifts between consecutive frames. This eliminates the need for a separate tissue Doppler acquisition, but, to avoid aliasing, the number of transmit beams have to be kept low. Hence, this method is most suitable for narrow sector imaging.

A method that achieves both a high frame rate B-mode and tissue Doppler with a

wide imaging sector will be presented in the last paper of this thesis.

## 1.5   Motivation and aims of study

The main motivation for this thesis is the need for higher frame rate in cardiac ultrasound imaging. Parallel beamforming is a promising technique for achieving this, but as pointed out in the introduction, this method suffers from B-mode image artifacts. Previous work performed on removing these artifacts is mainly contained within commercial patents, hence little information exists on the mechanisms of these artifacts or on metrics to evaluate and quantify them. As patents are aimed at describing rather than evaluating, they also provide little information about the actual performance of the methods in practical, realistic scenarios. Academic work on this subject is thus in short supply.

Combined modes, such as TDI, where combined B-mode and tissue Doppler data are acquired using separate acquisitions, reduce the frame rate. Since high frame rates are necessary for TDI quantitative analysis, this problem is often solved by reducing the field of view or reducing the image quality in the B-mode or tissue Doppler.

The aims of this thesis are to:

**Aim 1:** Indentify the mechanisms of parallel beamforming artifact and develop metrics to evaluate these mechanisms.

**Aim 2:** Investigate possibilities for artifact compensation and evaluate their performance using the developed metrics.

**Aim 3:** Investigate the performance of the compensation techniques in realistic, aberrating scenarios.

**Aim 4:** Address the possibilities of increasing the frame rate of combined tissue Doppler and B-mode imaging.

## 1.6   Summary of presented work

The following subsections contain summaries of the papers in this thesis. They are listed in the order the research was performed, which is not necessarily the order of publication. The third paper is in a review process and has recently been resubmitted after a revision. The fourth paper is unpublished, but has recently been submitted for publication in a peer-reviewed journal.

**Paper no. 1:**
**Parallel beamforming using synthetic transmit beams**

This paper addressed the fundamental source of parallel beamforming artifacts, namely the misalignment of the transmit and receive beams. This misalignment results in distortions to the ultrasound imaging beam that varies both with depth and from beam to beam. Due to this, parallel beamforming imaging systems are not spatially shift invariant; i.e. the image of an object varies with the object location. To remove distortions to the ultrasound beams and restore shift invariance, this work suggested creating synthetic transmit beams in the direction of each receive beam. The fundamental implementation of this technique is to create the synthetic transmit beams from interpolation on the unfocused channel data prior to beamforming. This work showed that an identical, but more practical feasible implementation can be performed after beamforming by receiving two times in each direction in neighboring transmit events. The proposed STB method was compared to other compensation methods through simulations and in vitro recordings. To evaluate the shift variance of the various methods, the paper introduced a plot that was later called the lateral shift variance plot (LSV plot). The paper also presented a formula for calculating the number of necessary parallel beams from the size of the transmit and receive apertures. The main result was that STB results in a more shift invariant imaging system with suppressed MLA artifacts. The paper also concluded that one of the other compensation methods, dynamic steering, appears to be a promising technique for removing MLA artifacts.

*The work was a joint effort with PhD student Torbjørn Hergum. Torbjørn Hergum conducted the theoretical work, illustrations and most of the writing. The author's main responsibilities were simulations, figures and quantitative results.*

*This paper was published in IEEE Transactions on Ultrasonics, Ferroelectrics, and Frequency Control, vol. 54, February 2007.*

**Paper no. 2:**
**The impact of aberration on high frame rate cardiac B-mode imaging**

This paper investigated the effect of aberration on parallel beamforming and dynamic steering as an MLA artifact compensation method. The B-mode artifacts of parallel beamforming are rooted in the misalignment of the transmit and receive beams. This causes the two-way beams to follow curved trajectories; i.e., the maximums of the two-way beam profiles are pulled towards the transmit beam directions. This is called warping. From models or simulations, the warping can be estimated, and the receive beams can be additionally offset to counteract the effect. This is the concept behind the dynamic steering method. The previous paper concluded that this was a promising technique for reducing MLA artifacts. This paper showed that although successful in ideal environments such as simulations and in-vitro recordings, the dynamic steering compensation fails in the presence of aberration. The mechanisms were investigated and explained through lateral shift variance plots, beam profile simulations, B-mode

38

simulations, in-vitro recordings and in vivo recordings. To measure the amount of artifacts in the B-mode image, this work introduced a new metric based on beam-to-beam correlation.

*The work was a joint effort with PhD Svein Arne Aase. Svein Arne Aase's main responsibility was scanner modifications and recording analysis. The author's main responsibility was simulations.*

*This paper was published in IEEE Transactions on Ultrasonics, Ferroelectrics, and Frequency Control, vol. 54, January 2007.*

**Paper no. 3:**
**Synthetic transmit beam technique in an aberrating environment**

Paper 2 showed that dynamic steering fails as an MLA artifact compensation method in aberrating environments. In this paper, the performance of the STB method was investigated in the presence of aberration. Given ideal STB interpolation, the only theoretical requirement for the STB method to work is that the transmit beam spacing satisfies the lateral Nyquist sampling theorem. Simple aberrations close to the transducer surface can be modeled as modifications to the transducer aperture. Such modifications do not increase the lateral bandwidth, and thus do not affect the sampling requirements. This work investigated STB performance with aberrations when using linear STB interpolation. The work was also a continuation of the first paper on STB. The number of parallel beams was increased from two to four, and new performance metrics such as speckle tracking error, higher order STB interpolation, beam profile shape conservation and beam-to-beam correlation are applied. The results showed that while aberration increases the image artifacts of conventional parallel beamforming, the usage of STB resulted in low levels of image artifacts both with and without aberration. This was also reflected in the speckle tracking errors, which increased with aberration for conventional parallel beamforming. Using STB the tracking error was almost unchanged. The LSV plots showed that using STB also resulted in close to shift invariance with aberration. Higher order STB interpolation further improved shift invariance, but might not be feasible due to potential motion artifacts. The beam profile shape was better preserved using STB. This was also reflected in the improved beam-to-beam correlation consistency.

*This paper is under review with IEEE Transactions on Ultrasonics, Ferroelectrics, and Frequency Control.*

**Paper no. 4:**
**Single pulse tissue Doppler using synthetic transmit beams**

While the previous papers focused on the amplitude of the echoes using parallel beamforming, this work focused on the phase of the echoes. More specifically, this work explored the possibility of estimating tissue velocities using the STB acquisition. This was enabled by double reception in each scan line direction. Since the proposed method

estimated the velocities from phase shifts between spatially neighboring transmit events, the method was named Single Pulse Tissue Doppler, SPTD. This method also included a novel transmit beam interleaving pattern, allowing the Nyquist limit to be adapted to cardiac velocities without loss in frame rate. The work addressed two problems of the SPTD method, namely the estimation bias and the higher estimation variance compared to regular TDI. The most noticeable problem with SPTD is the estimation bias which varies both from beam to beam and with depth. Through simulations, it was shown that the SPTD bias originated from lateral phase variations across the transmit beam. Model-based averaging was proposed as compensation. Warping and skewing resulted in decorrelation between scan lines in the same direction. This increased the estimation variance compared to regular TDI. However, if bias compensation and moderate radial averaging are applied, the accuracy of the SPTD velocity estimates are close to those of regular TDI. The use of the SPTD method resulted in combined B-mode and tissue Doppler images of the whole left ventricle at a frame rate of 110 frames per second.

*This paper has been submitted for publication in IEEE Transactions on Ultrasonics, Ferroelectrics, and Frequency Control.*

## 1.7 Discussion

The work in this thesis has shown that the STB technique improves shift invariance and reduces parallel beamforming artifacts. This makes parallel beamforming a more attractive technique, since the frame rate can be increased without compromising image quality. However, there are parameters other than shift invariance and artifacts, mainly spatial resolution, contrast resolution and penetration also determine image quality. As pointed out in the introduction, MLA can be used to increase the frame rate by a factor of four without compromising any of these measures of image quality (assuming that IQ interpolation is not used). If the frame rate is increased above this, the transmit aperture should be reduced to satisfy the transmit beam Nyquist criterion. This reduces spatial resolution and penetration. The biggest problem is the reduced penetration. This could be solved by applying coded excitation. A disadvantage of coded excitation for B-mode imaging is, however, that it cannot be used in combination with second harmonic imaging.

Another solution could be to use the STB technique in combination with MLT (multiple line transmission). This would allow a further increase in frame rate proportional to the number of parallel transmit beams. This could then be achieved without a loss in shift invariance, spatial resolution or penetration. The problem that would then have to be solved is the decreased contrast resolution due to cross-talk interference.

An important issue with the STB technique is potential motion artifacts. If the motion between neighboring transmit events becomes comparable to the wavelength of the imaging pulse, the resulting image might contain image artifacts. This is a common problem for all techniques that rely on the coherent combination of data from

several transmits. Both the previously described limited diffraction beam technique and the synthetic aperture technique rely on coherent combination to increase the resulting image quality. It is worth noting that the coherent combination in both these techniques is used for a different reason than for STB. The data is combined to increase spatial resolution and contrast resolution. Typically, data from more than two transmit beams are combined. This increases the time span of the combined data and also adds the problem of accelerated motion. The resolution of STB, on the other hand, is already defined by the MLA acquisition parameters. The STB combination is aimed only at removing image artifacts. This is done by combining data from only two transmits. This reduces the time span of the combined data and also avoids the problem of accelerated motion. This should make it easier to compensate for motion artifacts in STB than in the synthetic aperture and the limited diffraction beam methods. To execute this compensation, the motion of the object will have to be estimated. The last paper on single pulse tissue Doppler is a step on the way to doing this.

An alternative solution to avoiding motion artifacts could be to use the incoherent STB method applied in the last paper of this thesis. Motion artifacts are then avoided by detecting the data prior to the STB processing. However, this method cannot be theoretically shown to be the equivalent of synthesizing transmit beams in the direction of the receive beams. Detailed investigations of this method remain for future work.

It should be mentioned, however, that only limited amounts of motion artifacts have been observed in this work. As pointed out in the discussion of paper three, even the peak cardiac velocities would not cause more than an approximately 0.85 dB drop in the power of the STB interpolated scan line. The high velocities of the blood imaged inside the cavity caused some artifacts. In most cases, however, this will be a minor disturbance, since the amplitudes of the blood echoes will usually be significantly lower than the echoes from tissue.

This work has been limited to 2D acquisition. Several 2D applications benefit from high frame rates, but frame rate is an even larger limitation for 3D acquisition. Future work should therefore investigate potential solutions for 3D parallel beamforming. A straightforward approach could be to implement the STB technique along a plane in one of the dimensions. This should work without any adaptations. However, applying the STB technique in both dimensions presents some challenges. One challenge is the increased hardware requirements. In a 2D implementation, the STB technique requires two receive beams in each scan line direction. When applying the STB technique in both dimensions, the number of receive beams per scan line is doubled; i.e., four receive beams are required for each scan line direction. Another challenge is motion artifacts. Scanning a volume instead of a plane makes it impossible to avoid large time delays between transmits in one of the dimensions. A solution could perhaps be to apply motion compensation prior to STB interpolation. Since STB in both dimensions results in the coherent combination of data from four receive beams for each scan line, this motion compensation will be more complex than for the 2D case.

The following paragraphs compare the achievements of this thesis to the aims stated in chapter 1.5.

The first aim of this thesis was to identify the mechanisms of parallel beamforming

artifacts and to develop metrics to evaluate them. The fulfillment of this aim has been a continuous process throughout the thesis papers. Although the first paper presented the basic mechanisms of parallel beamforming artifacts, new knowledge was acquired throughout the remaining papers as well. Each of the three first papers presented new metrics for evaluating performance, and these metrics provided more insight into the image artifact mechanisms. While the first three papers concentrated on B-mode artifacts, the last paper also showed the impact that parallel beamforming has on the phase of each scan line.

The second aim was to investigate the possibilities for artifact compensation and to apply the metrics that had been developed to evaluate performance. All of the first three papers covered this. The first paper proposed the STB method as compensation, and compared it to several other methods using LSV plots. Another method, based on beam steering, was investigated in paper two with an increased arsenal of metrics. As new metrics were developed in papers two and three, these was also used to evaluate STB in paper three. The conclusions are that it is possible to compensate for these artifacts, and that STB seems to be the most robust and promising technique.

The third aim was to investigate the performance of the compensation techniques in realistic, aberrating scenarios. Although this was not done in the first paper of this thesis, it is a continuous theme throughout the remaining papers. The different conclusions obtained from investigating the dynamic steering method both with and without aberration in paper one and two show the importance of a realistic test scenario.

The fourth aim was to address the possibilities of increasing the frame rate of combined tissue Doppler and B-mode imaging. This was the main theme of the last paper in this thesis. It showed that although the mechanisms of parallel beamforming result in some challenges in doing so, it is possible to achieve a combined acquisition of these two modes with velocity estimation accuracy comparable to that of conventional TDI.

## 1.8 Conclusion

This thesis work has shown that native parallel beamforming results in B-mode image artifacts. The mechanisms behind these artifacts have been identified and described. The main proposed method is to remove artifacts by interpolating synthetic transmit beams (STB) in each parallel receive direction. Several metrics have been developed to investigate this and other methods. It can be concluded that STB counteracts the acoustic distortions caused by parallel beamforming, improves lateral shift invariance and decreases the image artifacts. It can also be concluded that the while the performance of steering compensation is reduced from aberrations, the STB performs well both with and without aberration. Using the STB acquisition pattern, it is in also possible to estimate tissue velocities with reasonable accuracy. This could provide an option for achieving a high frame rate TDI.

42

## 1.9    Publication list

**Peer reviewed papers**

1. T. Bjåstad, S. A. Aase and H. Torp, "The Impact of Aberration on High Frame Rate Cardiac B-Mode Imaging", *IEEE Transactions on Ultrasonics, Ferroelectrics and Frequency Control*, vol. 54, no. 1, pp. 32-41, 2007.

2. T. Hergum, T. Bjåstad, K. Kristoffersen and H. Torp, "Parallel beamforming using synthetic transmit beams", *IEEE Transactions on Ultrasonics, Ferroelectrics and Frequency Control*, vol. 54, no. 2, pp. 271-280, 2007.

**Conference proceedings**

1. T. Hergum, T. Bjåstad and H. Torp, "Parallel beamforming using synthetic transmit beams", *Proc IEEE Ultrason Symp*, vol. 2, pp. 1401-1404, 2004.

2. T. Bjåstad, S. A. Aase and H. Torp, "Velocity Sensitivity Mapping in Tissue Doppler Imaging", *Proc IEEE Ultrason Symp*, vol. 4, pp. 1968-1971, 2005.

**Submitted for publication**

1. T. Bjåstad and H. Torp, "Synthetic transmit beam technique in an aberrating environment", *IEEE Transactions on Ultrasonics, Ferroelectrics and Frequency Control*.

2. T. Bjåstad and H. Torp, "Single pulse tissue Doppler using synthetic transmit beams", *IEEE Transactions on Ultrasonics, Ferroelectrics and Frequency Control*.

# References

[1] R. A. Fessenden, "Method for measuring distance." U.S. Patent 1.217.585, 1914.

[2] B. B. Goldberg and B. A. Kimmelman, *Medical Diagnostic Ultrasound: A Retrospective on its 40th Anniversary*. New York: Eastman Kodak Company, 1988.

[3] Edler and C. H. Hertz, "The use of ultrasonic reflectoscope for the continuous recording of the movements of heart walls," *Communicated by Prof. B. Edlén*, 1954.

[4] B. Lind, J. Nowak, J. Dorph, J. van der Linden, and L. A. Brodin, "Analysis of temporal requirements for myocardial tissue velocity imaging," *Eur J Echocardiogr*, vol. 3, pp. 214–9, Sep 2002.

[5] H. Kanai, M. Sato, Y. Koiwa, and N. Chubachi, "Transcutaneous measurement and spectrum analysis of heart wall vibrations," *IEEE Trans UFFC*, 1996.

[6] H. Kanai, H. Hasegawa, N. Chubachi, Y. Koiwa, and M. Tanaka, "Non-invasive evaluation of local myocardial thickening and its color-coded imaging," *IEEE Transactions on Ultrasonics Ferro-electrics and Frequency Control*, 1997.

[7] D. P. Shattuck, M. D. Weinshenker, S. W. Smith, and O. T. von Ramm, "Explososcan: A parallel processing technique for high speed ultrasound imaging with linear phased arrays," *J Acoust Soc Amer*, vol. 75, no. 4, pp. 1273–1282, 1984.

[8] O. T. von Ramm, S. W. Smith, and H. G. Pavy, "High-speed ultrasound volumetric imaging system – part II: Parallel processing and image display," *IEEE Trans Ultrason Ferroelectr Freq Control*, vol. 38, pp. 109–115, March 1991.

[9] J. N. Wright, *Image formation in diagnostic ultrasound*. IEEE International Ultrasonics Symposium Short Course, 1997.

[10] T. L. Szabo, *Diagnostic ultrasound imaging: inside out.* Burlington, USA: Elsevier Academic Press, 2004.

[11] T. Misaridis and J. A. Jensen, "Use of modulated excitation signals in medical ultrasound. part iii: High frame rate imaging," *IEEE Transactions on ultrasonics, ferroelectrics, and frequency control*, vol. 52, 2005.

[12] S. Nikolov, *Synthetic aperture tissue and flow ultrasound imaging, PhD Thesis, Ørsted*. 2800, Lyngby, Denmark: DTU, Technical University of Denmark, 2001.

[13] J. A. Jensen, S. I. Nikolov, K. L. Gammelmark, and M. H. Pedersen, "Synthetic aperture ultrasound imaging," *Ultrasonics*, vol. 44, 2006.

[14] J. A. Jensen, O. Holm, L. J. Jensen, H. Bendsen, S. I. Nikolov, B. G. Tomov, P. Munk, M. Hansen, K. Salomonsen, J. Hansen, K. Gormsen, H. M. Pedersen, and K. L. Gammelmark, "Ultrasound research scanner for real-time synthetic aperture image acquisition," *IEEE Trans. Ultrason. Ferroelec. Freq. Contr.*, vol. 52, 2005.

[15] G. Trahey and L. Nock, "Synthetic receive aperture imaging with phase correction for motion and for tissue inhomogenities part ii: effects of and correction for motion," *IEEE Trans. Ultrason. Ferroelec. Freq. Contr.*, vol. 39, 1992.

[16] M. Karaman, H. Bilge, and M. ODonnell, "Adaptive multi element synthetic aperture imaging with motion and phase aberation correction," *IEEE Trans. Ultrason. Ferroelec. Freq. Contr.*, vol. 42, 1998.

[17] C. Hazard and G. Lockwood, "Effects of motion artifacts on a synthetic aperture beamformer for real-time 3d ultrasound," *Proceedings of the IEEE Ultrasonic Symposium*, 1999.

[18] J. Jeong, J. Hwang, M. Bae, and T. Song, "Effects and limitations of motion compensation in synthetic aperture techniques," *Proceedings of the IEEE Ultrasonic Symposium*, 2000.

[19] J. yu Lu, J. Cheng, and J. Wang, "High frame rate imaging system for limited diffraction array beam imaging with square-wave aperture weightings," *IEEE Transactions on Ultrasonics, Ferroelectrics and Frequency Control*, vol. 53, 2006.

[20] J. A. Stratton, *Electromagnetic Theory*, p. 356. New York and London: McGraw-Hill Book Company, 1941.

[21] J.-Y. Lu, H. Zou, and J. F. Greenleaf, "Biomedical ultrasound beam forming," *Ultrasound Med Biol*, vol. 20, 1994.

[22] J.-Y. Lu, "2d and 3d high frame rate imaging with limited diffraction beams," *IEEE Transactions on Ultrasonics, Ferroelectrics and Frequency Control*, vol. 44, 1997.

[23] L. J. Augustine, *High resolution multiline ultrasonic beamformer*. United States Patent 4.644.795, 1987.

References

[24] N. Wright *et al.*, *Method and apparatus for coherent image formation.* United States Patent 5.623.928, 1997.

[25] M. Bernard J. Savord, Andover, "Method and apparatus for increasing the frame rate and resolution of a phased array imaging system." U.S. patent 5.318.033, 1992.

[26] T. J. Hunt, B. M. Herrick, K. K. Robertson, and J. M. Ziel, "Ultrasonic imaging system using line splicing and parallel receive beam formation." U.S. patent 5.462.057, Oct. 31 1995.

[27] D.-L. D. Liu, J. C. Lazenby, Z. Banjanin, and B. A. McDermot, "System and method for reduction of parallel beamforming artifacts." U.S. Patent 6.447.452, Sep. 10 2002.

[28] G. L. Holley and I. M. Guracar, "Ultrasound multi-beam distortion correction system and method." U.S. Patent 5.779.640, July 14 1998.

[29] B. S. Robinson, "Ultrasonic diagnostic imaging systems with blended multiline for 2d and 3d applications." U.S. Patent 6.482.157, Mar. 30 2001.

[30] W. McDicken, G. Sutherland, C. Moran, and L. Gordon, "Colour doppler velocity imaging of the myocardium," *Ultrasound Med Biol*, 1992.

[31] P. N. T. Wells, "Ultrasonic colour flow imaging," *Phys. Med. Biol.*, 1994.

[32] C. Kasai, K. Namekawa, A. Koyano, and R. Omoto, "Real-time two-dimensional blood flow imaging using an autocorrelation technique," *IEEE transactions on sonics and ultrasonics*, 1985.

[33] J. Kirkhorn, S. Bjærum, B. Olstad, K. Kristoffersen, and H. Torp, "A new technique for improved spatial resolution in high frame rate color Doppler imaging," *Proc IEEE Ultrason Symp*, pp. 1947–1950, 2003.

[34] S. Bjaerum, H. Torp, and K. Kristoffersen, "High frame rate tissue doppler imaging," *Proceedings IEEE Ultrasonics Symposium*, 2001.

# Chapter 2

# Parallel Beamforming using Synthetic Transmit Beams

Torbjørn Hergum[1], Tore Bjåstad[1], Kjell Kristoffersen[2] and Hans Torp[1]
[1]Department of Circulation and Medical Imaging, Faculty of Medicine,
Norwegian University of Science and Technology (NTNU)
[2] GE Vingmed Ultrasound, Horten, Norway

Parallel beamforming is frequently used to increase the acquisition rate of medical ultrasound imaging. However, such imaging systems will not be spatially shift invariant due to significant variation across adjacent beams. This paper investigates a few methods of parallel beamforming who aims at eliminating this flaw and restore the shift invariance property. The beam-to-beam variations occur because the transmit and receive beams are not aligned. The underlying idea of the main method presented here is to generate additional synthetic transmit beams (STB) through interpolation of the received, unfocused signal at each array element prior to beamforming. Now each of the parallel receive beams can be aligned perfectly with a transmit beam - synthetic or real - thus eliminating the distortion caused by misalignment.

The proposed method was compared to the other compensation methods through a simulation study based on the ultrasound simulation software Field II. The results have been verified with in vitro experiments. The simulations were done with parameters similar to a standard cardiac examination with two parallel receive beams and a transmit-line spacing corresponding to the Rayleigh criterion, wavelength times f-number ($\lambda \cdot f\#$).

From the results presented it is clear that straightforward parallel beamforming reduces the spatial shift invariance property of an ultrasound imaging system. The proposed method of using synthetic transmit beams seems to restore this important property, enabling higher acquisition rates without loss of image quality.

## 2.1 Introduction

When performing ultrasound imaging of moving structures there is a demand to increase the rate of the image acquisition. This is particularly true for 3D imaging of the moving heart. A common way to increase the frame-rate of ultrasound imaging without compromising the number of scan lines is to use multiple beamformers [1][2]. With this approach several parallel receive-beams from closely spaced regions can be acquired simultaneously for each transmit-beam. The image acquisition rate is thus increased proportionally to the number of beamformers. However, as the transmit- and receive-beams are misaligned such a technique will result in spatial shift variance due to considerable beam-to-beam variation across adjacent beams. The shift variance is manifested as stationary stripes in the ultrasound image, and becomes more distinctive with increasing number of parallel receive beams.

Some methods have been proposed to solve this problem. One of them is to use a *sinc*-apodization on the transmit aperture, which theoretically will generate a square transmit beam profile, thus providing an uniform two-way response regardless of where the receive beam is positioned inside the transmit beam [3].

Another proposal is found in an U.S. patent submitted by J. N. Wright *et al.* [4]. The patent formulates a general method for reducing parallel beam artifacts based on creating synthetic scan lines through interpolation on combinations of existing scan lines. However, there is no obvious way of selecting the optimum beam spacing and interpolation filter coefficients when the 2-way beamprofiles are skewed or have irregular spacing.

In contrast to synthetic scan lines the idea introduced in this paper is to create synthetic transmit beams through interpolation on the unfocused signal at each element. However, with a proper choice of interpolation filter the interpolation can be performed on beamformed data instead of element data, making it easy to implement in real-time.

To begin with the inherent problems with parallel processing will be addressed. Then the general theory of the proposed method is examined, followed by one specific implementation of it. Next this is compared to other parallel processing compensation methods. Finally results from comparing the various compensation methods through simulations and in vitro experiments will be presented and discussed.

## 2.2 Background and Problem Statement

The geometric distortions due to misalignment of the transmit- and receive beams can be separated into two underlying effects; "warping" and "skewing". Beam warping, sometimes called "beam wander", is the effect that the two-way beam will in general not follow a straight line. When a transmit- and receive beam is not perfectly aligned, the transmit beam will 'pull' the receive beam toward its center, making the center of the two-way beam different from that of both the transmit- and receive beams. For the following argument the beam profiles will be assumed to have a Gaussian shape. The depth-dependent beam width is given by $\sigma_t(r)$ and $\sigma_r(r)$ for the transmit- and
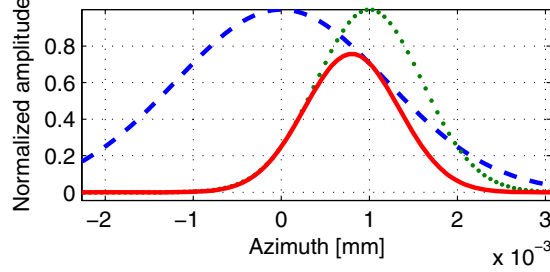
Figure 2.1: The warping effect of misaligned ultrasound Gaussian-shaped transmit (dashed) and receive (dotted) beams. Notice that the two-way beam (solid), the product of the transmit and receive beams, is centered in-between the peaks of the two one-way functions.

receive beam respectively, giving the two-way beam profile $g_{tr}(x)$ as

$$g_{tr}(x,r) = g_t(x - x_t, r)g_r(x - x_r, r)$$
$$\Downarrow$$
$$g_{tr}(x,r) = e^{-\frac{(x-x_t)^2}{2\sigma_t(r)^2}} e^{-\frac{(x-x_r)^2}{2\sigma_r(r)^2}} \tag{2.1}$$

where subscript $t$ indicates "transmit", $r$ indicates "receive" and $tr$ indicates "transmit-receive". An example of $g_{tr}(x)$ is plotted with $g_t(x)$ and $g_r(x)$ in Fig. 2.1, showing the warping.

The peak position $x = x_p$ of this function is found where $\partial g_{tr}/\partial x = 0$. The origin of the coordinate system is then positioned at the center of the transmit beam, that is, $x_t = 0$, yielding the following equation for the position of the peak:

$$x_p = \frac{\sigma_t^2 x_r + \sigma_r^2 x_t}{\sigma_t^2 + \sigma_r^2}$$
$$\Downarrow x_t = 0$$
$$x_p = \frac{\sigma_t^2 x_r}{\sigma_t^2 + \sigma_r^2} \tag{2.2}$$

The peak position of the two-way beams resulting from three transmit events using two parallel receive beams each is plotted in Fig. 2.2. The left part of the figure is simulated using Field II [5]. Although only the peak position of the pulse-echo field is plotted here, the full 2D transmit- and receive profiles were calculated. The $-3dB$ contour of these profiles were used as the depth-dependent beam widths $\sigma_t(r)$ and $\sigma_r(r)$ of (2.2). The peak position using the Gaussian beam profiles with depth dependent beam widths provided by Field II simulation is displayed in the right part of Fig. 2.2. Note that the received signal is assumed to follow straight lines. Due to the warping effect the samples are acquired from along curved lines, making the lateral
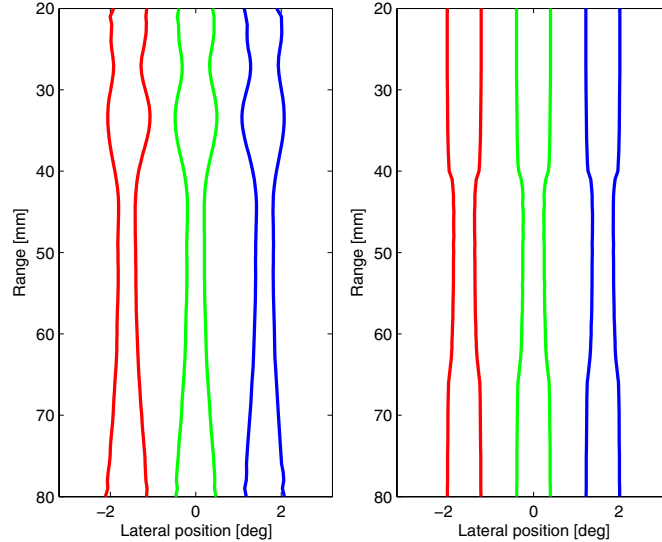
Figure 2.2: The lateral *peak position* of two-way beams as a function of depth. The left figure is simulated using Field II. The right figure is a plot of (2.2), which uses the Gaussian beam approximation. The two-way beams are the result of three transmit beams with two parallel receive beams each. Note the uneven sampling resulting from the curved scan lines, particularly the lack of samples at some locations around the focal depth at 5 cm. See text for details.

sampling non-regular. If the beams are distributed according to the Nyquist criterion, this non-regular sampling will lead to under-sampling, aliasing and thus loss of spatial invariance and image quality.

The simulation settings for both simulations can be found in Table 2.1. As can be seen by comparing the left and right part of the figure, the Gaussian beam approximation is only valid in the vicinity of the focal depth. In the near- and far-field this simple model is not sufficient to describe the field.

The second part of the geometric distortions are due to "skewing", since the beam profiles are in fact not Gaussian as assumed above. A skew (non-symmetric) two-way RMS beam profile resulting from offsetting a symmetric receive beam and a symmetric transmit beam is shown in Fig. 2.3. The RMS beam profile is found by calculating the root mean square along the time/radial direction of the transmit-, receive- and two-way field simulated using Field II.

Yet another effect of parallel beamforming is the loss of energy caused by misaligning the transmit- and receive beams. Using two parallel receive beams positioned symmetrically around the transmit beam will decrease the signal-to-noise ratio (SNR). However, using more than two parallel receive beams will give beams with varying gain. Compensating for this varying gain loss through amplification (*i.e.* by using (2.1)) will give beams with varying SNR and variance, further degrading the
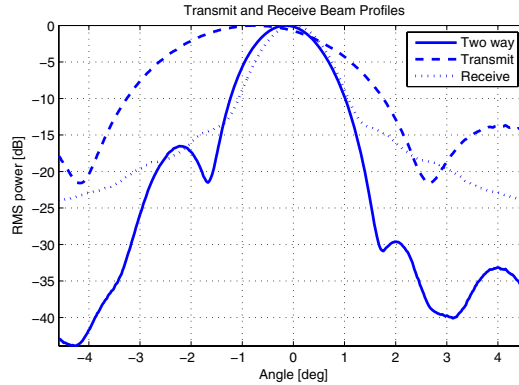
Figure 2.3: Beam profiles of transmit-, receive-, and two-way response. The transmit f# is twice that of the receive f#. Note the skewness of the two-way profile.

spatial invariance.

## 2.3 Shift Invariance through Coherent Interpolation

The goal of the proposed method in this article is to overcome the geometrical distortions caused by misaligned transmit- and receive-beams by creating synthetic transmit-beams in-between the real transmit-beams. The first step on the way to achieve this is to transmit beams with a spacing of no more than the Nyquist sampling criterion for ultrasound, $f\#\lambda$, which is also called the Rayleigh criterion [6]. Assume for the sake of the argument that the signal received on each element of the aperture and for all transmit events are stored separately and coherently in the ultrasound scanner. The sampling theorem states that the value from any intermediate beam can be found from these data through interpolation. Next these interpolated data can be passed through a receive beamformer, adding appropriate focusing delays to steer in the direction of the synthetic transmit beam. Since the receive beams are steered to the same point in space as the synthetic transmit beams, there will be no geometrical distortions of the two-way beams due to misalignment.

Let us now state this more formally. Fig. 2.4 puts some of the symbols into a sketch showing the elements of a simple transducer and the signals received from two consecutive excitation events. The aperture consists of $N$ elements transmitting $M$ beams into the imaging sector. To transmit beam number $k$, $1 < k < M$, the aperture is focused on the point $x_k$ at the depth $d = ct_0/2$. The received signal at aperture element $n$ after focusing at point $x_k$ is denoted $S_n(x_k, t_0)$, where $1 < n < N$. The signal originating from an intermediate position $x_i$ can be found through interpolation after collecting data from the desired amount of beams $k$. For each element $n$ on the aperture the recorded signals $S_n(x_k)$ are used to find the synthetic signal $\tilde{S}_n(x_i)$ using the interpolation filter $h(x_i, k)$:
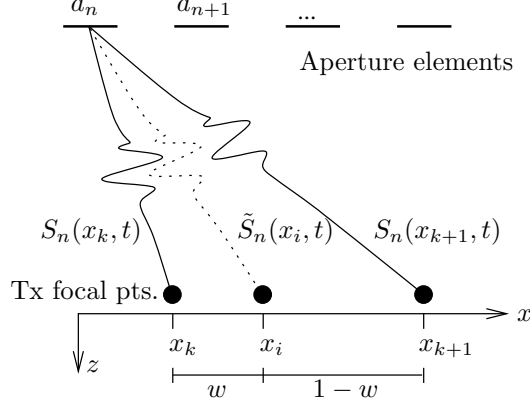
Figure 2.4: Illustration of the received signals on aperture element $a_n$ when transmit focus is set at the points $x_k$ and $x_{k+1}$. The interpolated signal $\tilde{S}_n(x_i, t)$ from the synthetic transmit beam focused at the point $x_i$ is also indicated. The normalized distances between the three points of interest is shown at the bottom.

$$\tilde{S}_n(x_i, t) = \sum_k h(x_i, k) S_n(x_k, t). \tag{2.3}$$

The total synthetic receive signal $\tilde{S}(x_i, t)$ from the point $x_i$ in space is found by focusing the synthetic receive- signals electronically to the point $x_i$ by adding time delays $\tau_n(x_i)$, and summing the signal from all elements on the aperture:

$$\tilde{S}(x_i, t) = \sum_n \tilde{S}_n(x_i, t - \tau_n(x_i)) \tag{2.4}$$

$$= \sum_n \sum_k h(x_i, k) S_n(x_k, t - \tau_n(x_i)) \tag{2.5}$$

$$= \sum_k h(x_i, k) \sum_n S_n(x_k, t - \tau_n(x_i)) \tag{2.6}$$

$$= \sum_k h(x_i, k) S_k(x_i, t) \tag{2.7}$$

where the interchange of the order of the summations from (2.5) to (2.6) can be done if the interpolation filter is linear, shift invariant and independent of $n$ (linear meant as a filter property, not filter type). The last sum in (2.6) is the mathematical expression for the signal $S_k(x_i, t)$ from a beam transmitted toward the point $x_k$ and then focused at the point $x_i$ while receiving. Instead of interpolating the received samples from each aperture element the same result can be achieved from steering the receive-beam toward the same point in subsequent transmit-events and then find the synthetic scan

line through interpolation of these signals, as is seen from (2.7). This will be denoted as parallel beamforming with STB (Synthetic Transmit Beams) throughout the text.

Changing the order of summation in (2.6) facilitates the practical implementation of STB as only the output data from the beamformer has to be buffered, which is a fraction of the size of the received signal from all aperture elements.

It is worth noting that STB like all coherent lateral interpolation methods assumes negligible object movement between subsequent transmit beams. If not, the phase difference between the interpolated signals might induce artifacts due to destructive interference. The maximum wall velocity in the left ventricle is typically $12cm/s$ [7] and a typical pulse repetition frequency for cardiac imaging is $4kHz$. The maximum wall displacement between subsequent beams is then found as $\frac{12cm/s}{4kHz} = 30\mu m$, which for a typical cardiac transmit frequency of $2.5MHz$ is less than one twentieth of a wavelength. A commonly used limit for coherent summation is $\lambda/8$ [6], so the STB method will sum coherently for fast cardiac movements as long as the interpolation filter is short.

For a rectangular aperture the Nyquist sampling requirement for beam density can be found from the Fraunhofer approximation to be one beam per $f_\#\lambda$, where $f_\# = F/a$ is the $f$-number, $F$ is the transmit focus depth, and $a$ is the aperture size on transmit or receive [8]. This is called the Rayleigh criterion. After including the oversampling factor $p^t$ and rearranging terms the lateral sampling frequency is found as

$$f_s^t = \frac{1}{p^t} \cdot \frac{a^t}{F \cdot \lambda} \qquad\qquad\qquad p^t \le 1. \qquad (2.8)$$

Again according to the Fraunhofer approximation the lateral bandwidth of the pulse-echo field is given by the convolution of the transmit- and receive apertures. Thus the two-way sampling frequency is found as

$$f_s^{tr} = \frac{1}{p^{tr}} \cdot \frac{(a^t + a^r)}{F \cdot \lambda} \qquad\qquad\qquad p^{tr} \le 1 \qquad (2.9)$$

where $a^t$ and $a^r$ is the aperture size on transmit and receive respectively, $\lambda$ the wavelength of the center frequency and $p^t$ and $p^{tr}$ oversampling factors on transmit and two-way respectively. The number of necessary parallel beams is now found as the ratio between $f_s^{tr}$ and $f_s^t$:

$$N_{pb} = \frac{p^t}{p^{tr}} \cdot (1 + \frac{a^r}{a^t}) \qquad (2.10)$$

For marginal sampling and equal aperture on transmit and receive it follows that two parallel beams are required to keep within the requirements of the sampling theorem. This case is treated experimentally in the next Section.
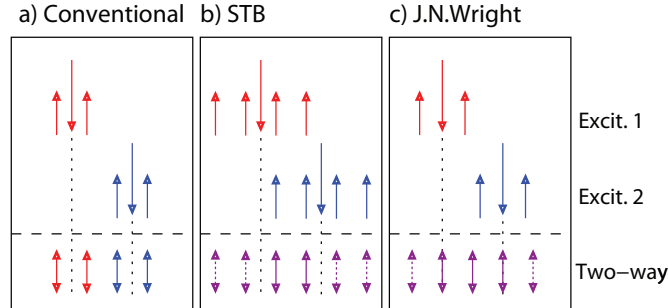
Figure 2.5: Sketch of the origin of scan lines.

Part *a)* of the figure shows two transmit beams (pointing down) with 2 parallel receive beams each, pointing up. The resulting scan lines are showed beneath the horizontal dashed line. The vertical dotted line extends the transmit beam direction to make it easier to see the alignment with the two-way beams.

Part *b)* of the figure shows the corresponding STB case. Here 4 parallel receive beams are acquired for each transmitted beam. These are aligned in pairs as shown, yielding the interpolated, synthesized beams showed beneath the dashed line. The solid arrows indicate the receive beams successfully generated from the two shown excitation events, while the dashed arrows represent scan lines that need another transmit event to be complete.

Part *c)* shows the origin of scan lines with the synthetic beam setup proposed by J. N. Wright.

## 2.4  Compensation Methods

### 2.4.1  Synthetic Transmit Beams

In Fig. 2.5*a)* an example of the conventional parallel beamforming approach is sketched, represented with two transmit beams and their corresponding two parallel receive beams. Beneath the dashed line the resulting 4 scan lines from these two excitations are shown.

Part *b)* of the figure sketches the corresponding practical implementation of the proposed STB method using a linear interpolation filter and two parallel receive beams. Note that twice the number of beamformers are necessary to form the synthetic transmit beams through interpolating the two receive beams at each position using the two-point linear interpolation filter

$$h(x_i, k) = [1 - w, w] \tag{2.11}$$
$$= [0.75, 0.25] \tag{2.12}$$

for the regularly spaced receive beams shown in Fig. 2.5. For a more general receive beam positioning $w$ is found as $w = \frac{x_i - x_k}{x_{k+1} - x_k}$, with reference to Fig. 2.4. Note that the STB principle can easily be extended to an arbitrary number of parallel receive

beams, only limited by the number of available receive beamformers.

Choosing a linear interpolation filter is the simplest implementation of STB, as only two receive beams has to be steered toward each desired scan line position. The impulse response of the linear interpolation filter is triangular, making it a $\text{sinc}^2$-function in the frequency domain [9]. This means that some of the high-frequency content of the signal will be attenuated, and there will be some noise due to aliasing from the wide transition band. The maximum error will appear for a marginally sampled white-noise process, where the reduction of power without aliasing compared to ideal interpolation is found from

$$P_{err} = 20 \log_{10} \left( \int\limits_{-f_s/2}^{f_s/2} \left( \frac{\sin(\pi f/f_s)}{\pi f/f_s} \right)^2 \mathrm{d}f \right) = -2.2\text{dB} \qquad (2.13)$$

where $f_s$ is the sampling frequency and $f$ is the lateral frequency variable.

The error will be lower for a band-limited signal, and is further reduced with oversampling, that is, using a higher density of transmit beams. However this is not wanted as the purpose of parallel beam processing is to obtain a high frame rate, which necessitates as scarce positioning of transmit beams as possible.

Higher order interpolation can be used if the necessary number of beamformers are available. Each scan line requires the same number of beamformers as the number of taps in the interpolation filter. Using an ideal interpolation filter in (2.7) will give perfect reconstruction with no artifacts from parallel processing. Unfortunately this requires an infinitely long interpolation filter, and the same number of beamformers.

## 2.4.2 Dynamic steering

Most modern (digital) beamformers are using different focusing delays for each depth when receiving, ensuring appropriate geometrical focus. This is called dynamic *focusing*. If the beamformer also updates the steering delays for each depth, this is called dynamic *steering*. Such a beamformer can focus along any line - straight or curved, upon reception.

If the beamformer is capable of such dynamic steering, another intuitive way of compensating for the warping effect is by deliberately offsetting the receive-direction for each depth in the opposite direction of the warping [10]. To make this work well a reasonably accurate beam model must run on the scanner. From Fig. 2.2 it can be seen that the Gaussian model presented in Section 2.2 can serve this purpose close to the focal depth, where it can be argued that a good image is most important. In other words, offsetting the receive focal direction with the inverse of (2.2) should reduce warping artifacts significantly.

If dynamic steering is not available, a fixed steering offset can be applied to eliminate warping at a desired depth, often chosen as the focal depth. However, this approach might lead to poor performance at other depths.

Table 2.1: Some common parameters for simulations and experiments.

| Parameter | Value |
|---|---|
| Center frequency $f_0$ | 2.5MHz |
| Focal point | 5cm |
| $f-$number transmit | 2.3 in focal point |
| $f-$number receive | 2.3 until the focal point, then increasing |
| Transmit line spacing | $1 \cdot \lambda f_{\#t}$ in focal point |
| Display interpolation | RF |

### 2.4.3 US patent by J. N. Wright

One version of the preferred embodiment in the US patent of J. N. Wright has been implemented both in simulations and experiments. It uses two parallel receive beams, and the synthetic beams are found by interpolating between these as given by Fig. 3 in the patent [4]. The position of transmit-, receive- and synthetic scan lines are indicated in part *c)* of Fig. 2.5.

The synthetic scanlines that align with the transmit *(tx)* beam are made by calculating the average of the two parallel receive *(rx)* beams originating from this transmit event. The synthetic beam halfway between the *tx* beams is calculated as the average between the two nearest *rx* beams, originating from two different *tx* events, as described in the patent. This is the same as running a two-point lateral averaging filter on the received RF data, meaning this method is expected to reduce the lateral resolution of the imaging system.

### 2.4.4 Simulation- and experimental setup

Using the ultrasound simulation software Field II [5] several approaches to parallel beamforming have been investigated: uncompensated, steering offset in focus, dynamically steered, the J. N. Wright method, and with synthetic transmit beams. Additionally the standard, focus offset, the J. N. Wright method and STB methods have been tested experimentally using a custom GE Vingmed Vivid 7 ultrasound scanner with 4 available beamformers.

The experimental image acquisition uses equivalent settings as for the simulations. Some common settings for all simulations and experiments can be found in Table 2.1. The effect of frequency dependent attenuation has not been taken into account in the simulations, but are naturally still present in the experiments.

## 2.5 Results and Discussion

A display method suitable for showing spatial variance artifacts is shown in Fig. 2.6. The top pane of the figure shows a simulated point spread function (PSF), with a corresponding RMS beam profile in the middle pane. By moving the point scatterer laterally and stacking the obtained beam profiles, the contour plot in the bottom
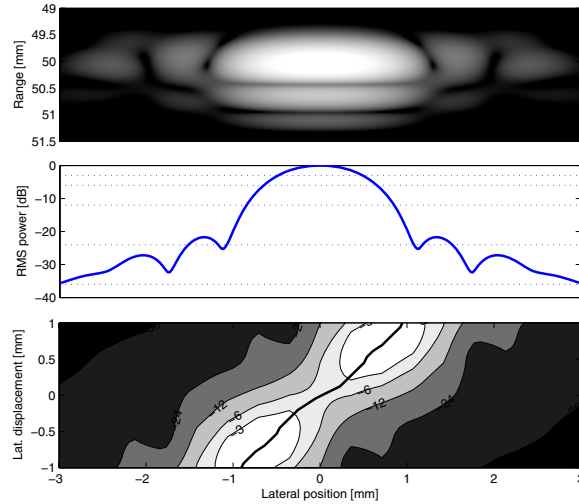
Figure 2.6: The top pane shows the image of a point scatterer, a point spread function (PSF). In the middle pane the beam profile (the RMS sum) of this PSF is shown. After obtaining such beam profiles for several lateral positions of the point scatterer the profiles are stacked and displayed in a contour plot in the lower pane. The level of the contours are [-3 -6 -12 -24 -36] dB as is indicated with dashed lines in the middle pane. The thick line indicates the peak position. If the imaging system is completely spatially shift invariant the contour plot should display a set of diagonals.

pane is obtained. A completely spatially shift invariant imaging system should show a non-varying diagonal structure.

The simulation results are displayed using three such plots each. For all plots the transmit focal depth is 5 cm and both dynamic focus and expanding aperture is used while receiving. The three plots shows the spatial variance resulting from moving a scatterer laterally at a depth of 3, 5 and 7 cm respectively. For a quantitative assessment of all simulation plots please refer to Table 2.2.

The reference situation where only one receive beam for each transmit beam is used is shown in Fig. 2.7. Note that for all scatterer depths the results are nearly spatially shift invariant, as is seen by the close to invariant diagonals. The nearly shift invariant property can also be seen quantitatively from Table 2.2. The right side of the figure shows experimental verification of the spatial variance plots, an image of an ultrasound phantom. In contrast to all the following setups, this simulation and experiment uses a transmit beam spacing of half the Rayleigh criterion, $\lambda f_{\#t}/2$, thus it runs at half the acquisition speed. This is done to give all plots the same scan line density, and can also be seen from (2.10).

Fig. 2.8 shows a plot for the case of using two parallel receive beams without any compensation techniques. Note that this results in a considerably more spatially variant imaging system at all depths. This is particularly noticeable around the focal
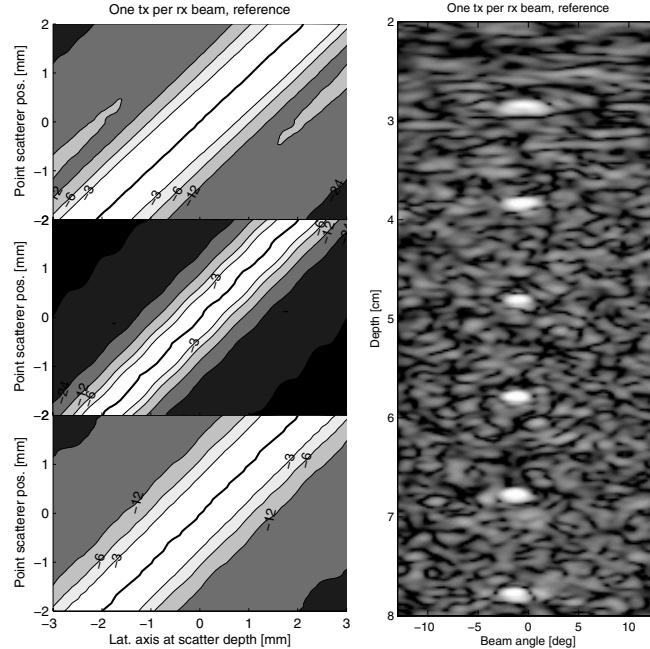
Figure 2.7: Reference situation, showing simulated results on the left side and an ultrasound image on the right for validation. The three panes of the simulations correspond to a scatterer depth of 3, 5 and 7 cm respectively. The thick line close to the center of the plot indicates the position of the beam peak value. The phantom image to the right was acquired with an ultrasound scanner using a phased array transducer. The beams are formed in a sector format and are displayed using polar coordinates. The remaining relevant settings are listed in Table 2.1, apart from the transmit line spacing, which is $\lambda f_{\#t}/2$ to make the scan line density equal the other simulations. See text for details.

depth. The image to the right displays how these artifacts show up in a recorded image. The lateral gain variation of nearly 5dB (see Table 2.2) is particularly noticeable. It is important to recognize that these artifacts are much more prominent in a dynamic image. The artifacts can be seen qualitatively in the movie, *Ch2_Movie01.mpg*, of the bicuspidal valve (located at *www.ntnu.no/us/ThesisMM/bjastad*).

Fig. 2.9 was made with the proposed method, STB. Compared to the uncompensated plots and image in Fig. 2.8 it is evident that the imaging is more shift invariant when STB is applied. The contour plots are better than the uncompensated version at all depths, and the image quality resembles that of the reference situation in Fig. 2.7. This can also be seen from the movie, *Ch2_Movie02.mpg*, which is made from offline processing of the same data set as *Ch2_Movie01.mpg* (located at *www.ntnu.no/us/ThesisMM/bjastad*). Note that this compensation method does not compromise on spatial resolution, as is seen in Table 2.2.
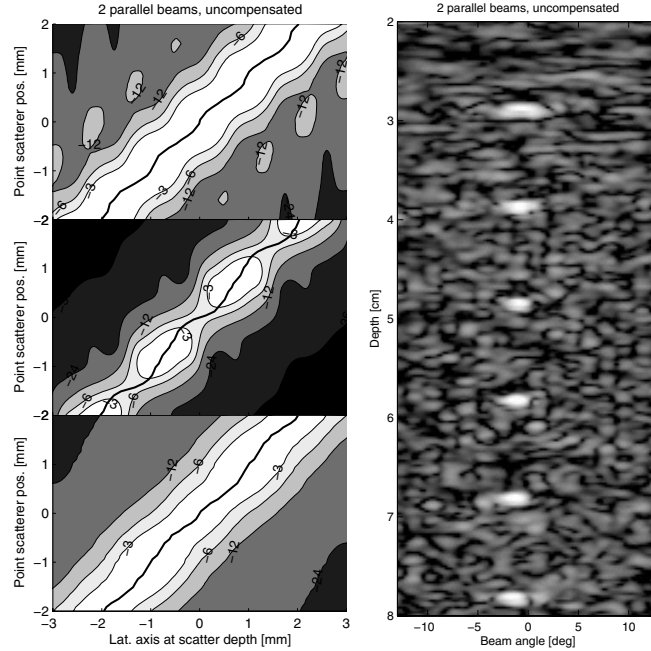
Figure 2.8: Imaging using 2 parallel receive beams, without any type of compensation. Note the evident lack of spatial invariance, especially with the scatterer at the focal depth (middle pane). This can also be seen from the ultrasound image to the right, where vertical stripes are apparent in a region around the focal depth of 5 cm.

The method proposed by J. N. Wright was found to perform best when the *rx*-beams were shifted further away from the *tx* direction, in the same manner as to compensate for the warping effect at the focal depth, as described in the section on *Dynamic steering*. The additional shift corresponded to a fourth of the receive line spacing. Results from simulations and experiments with these settings are displayed in Fig. 2.10, and numerical results from the simulations can be found in Table 2.2. Comparing these figures with those of the STB method in Fig. 2.9, the J. N. Wright method is seen to display nearly as good spatial shift invariance as the STB method. However, from the numerical results this method it is seen to give a 15% reduction in lateral resolution when compared to the STB method.

If dynamic steering is not available, the warping can only be fully compensated for at one specific depth. Figure 2.11 shows the results from warp-compensating at the focal depth. The middle left pane shows that offsetting the steering angle to eliminate warping at the focal depth successfully eliminates warping in focus. However the spatial invariance is significantly reduced below and above the focal point.

The left pane of Fig. 2.12 shows simulated results from using dynamic steering to compensate for warping at all depths. Unfortunately no experimental results are
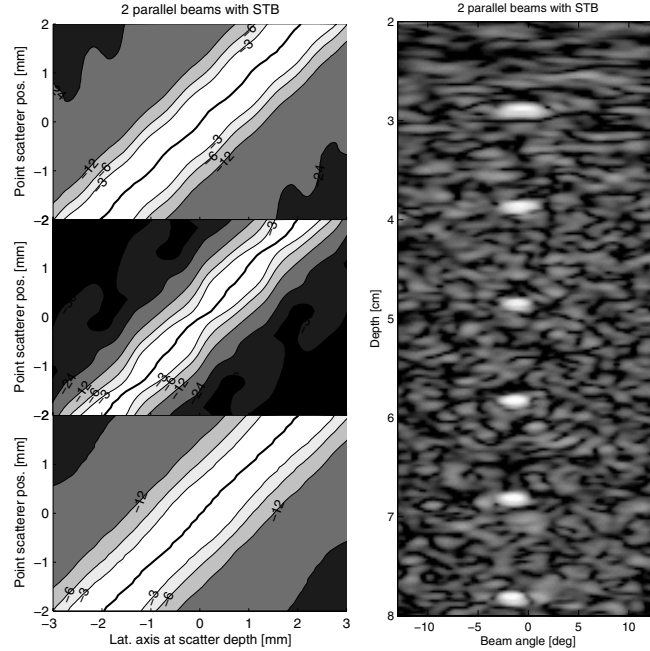
Figure 2.9: Much of the artifacts originating from parallel receive beams can be eliminated by using STB imaging, as is shown here. Note the difference from the uncompensated images in Fig. 2.8. Both experimental images were made with the same parameters and the same transmit- and scan line density. They differ only in the number of beamformers used. The axes show depth and angle increment, where the center line is chosen as zero degrees. Note how the STB image shows no signs of the easily noticeable vertical stripes of the image without STB. Also note that there is still some ripple left at the focal depth of the contour plot. This is probably caused by the non-ideal linear interpolation filter used.

available due to limitations in the available ultrasound scanner. When the steering compensation is done dynamically, warping is eliminated at all depths up until the accuracy of the Gaussian beam approximation. Note that the skewing artifact is left uncompensated with this approach. This is particularly noticeable in the top pane where the spatial invariance is poor despite the steering compensation efforts.

For completeness the right pane of Fig. 2.12 shows the simplest option when it comes to increasing the acquisition rate, simply decreasing the scan line density. From the two bottom panes it is seen that this approach suffers from under-sampling. It important to remember that the sampling criterion has to be credited at both transmit, receive and two-way. Even if this simple method has sufficient sampling on transmit and receive, the two-way situation is under-sampled.

Some numerical results from the simulation study are summarized in Table 2.2.
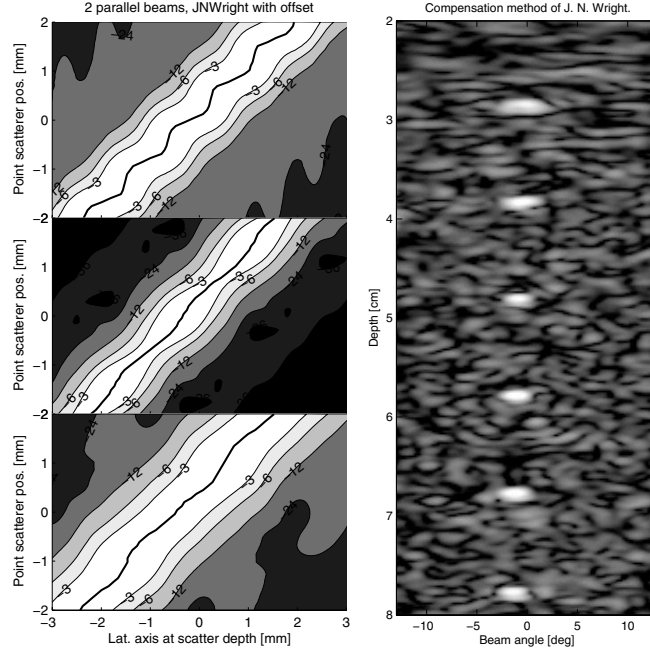
Figure 2.10: The J. N. Wright method with a static receive beam offset. No easily noticeable vertical stripes can be seen in the image. The image is however more blurred than the corresponding STB image. Also notice the more variable peak position (thick solid line) at all depths compared to STB.

The results of the first two columns are calculated with normalized beams, that is, the peak value is zero for all lateral scatter positions. The first column lists the mean -6dB beam width. The "Width var." and "Gain var." columns quantifies the difference between the min. and max. -6dB beam width and the peak gain difference respectively. The "Offset" column is computed to give a measure of the meandering movement of the peak position. It is given as the ratio of the two-sided lateral peak position error and the mean beam width at each depth.

Investigating the first column of the Table, it is seen that the mean beam width of the J. N. Wright method is slightly larger than for the other imaging methods. This can be contributed to the lateral filtering performed in this method. Apart from that, the mean beam width at at each depth is quite constant for each imaging method, with the exception of the undersampled method. Note that this is the case even when steering compensation methods are applied. Using a Gaussian beam profile approximation it can easily be shown that this is as expected. Looking at mean beam widths does not tell anything about the shift invariance property of the methods. This is better seen in the next column, displaying the difference between the maximum and minimum beam width as the scatterer is moved laterally. It can here be observed that all methods,

Table 2.2: Numerical results from comparison of parallel beamforming techniques.

| Method | Depth | Mean beam width [mm] | Width var. | Gain var. [dB] | Offset |
|---|---|---|---|---|---|
| Reference, | | | | | |
| | 30 mm | 2 | 3% | 0.3 | 2% |
| | 50 mm | 1.2 | 15% | 0.64 | 11% |
| | 70 mm | 2.1 | 7% | 0.32 | 5% |
| Uncomp., | | | | | |
| | 30 mm | 2 | 5% | 0.32 | 11% |
| | 50 mm | 1.3 | 37% | 4.8 | 29% |
| | 70 mm | 2.1 | 18% | 1.4 | 13% |
| Focus comp., | | | | | |
| | 30 mm | 2.1 | 76% | 0.89 | 50% |
| | 50 mm | 1.2 | 13% | 0.76 | 12% |
| | 70 mm | 2.3 | 115% | 3.66 | 48% |
| Dyn. steered, | | | | | |
| | 30 mm | 2 | 4% | 0.48 | 15% |
| | 50 mm | 1.2 | 13% | 0.72 | 11% |
| | 70 mm | 2.1 | 12% | 0.92 | 9% |
| STB, | | | | | |
| | 30 mm | 1.9 | 2% | 0.29 | 6% |
| | 50 mm | 1.3 | 16% | 1.97 | 16% |
| | 70 mm | 2.1 | 10% | 0.79 | 6% |
| J.N.Wright method, | | | | | |
| | 30 mm | 2 | 7% | 0.91 | 23% |
| | 50 mm | 1.5 | 15% | 2.12 | 16% |
| | 70 mm | 2.4 | 18% | 1.06 | 13% |
| Undersampled, | | | | | |
| | 30 mm | 2.2 | 25% | 0.51 | 9% |
| | 50 mm | 1.6 | 86% | 7.09 | 89% |
| | 70 mm | 2.6 | 57% | 3.49 | 41% |

except for the focus compensation method, perform best before and after the focal depth. This is due to the wider transmit beam at these depths. At the focal depth the -6dB beam width vary with 37% when no compensation is done. When applying either dynamic steering, the J. N. Wright method, or STB, all of which have similar performance here, the width variation is greatly reduced to around 15%, the same as in the reference situation. Looking at the next column, the gain variation, the dynamic steering method performs best, reducing the variation from 4.88dB uncompensated to 0.72dB at focal depth. That is only slightly higher than the reference situation and then as good as one can expect it to be with the applied beam density. An interesting number is the 2dB gain variation at the focal depth for the STB method.
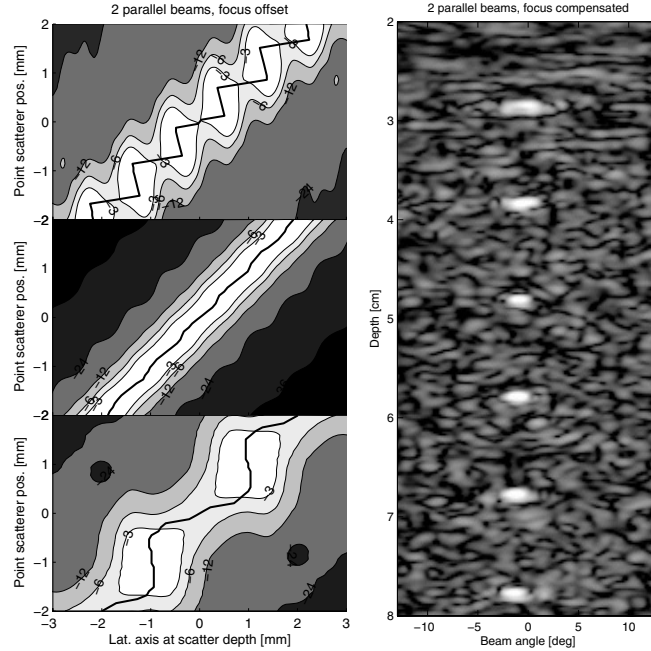
Figure 2.11: Here the results from warp compensation by statically offsetting the receive beam is shown. The offset is calculated to eliminate warping at the focal depth, resulting in poor performance at other depths.

This variation is most likely due to linear interpolation of marginally sampled data. The applied two point linear interpolation filter is not sufficient to fully correct for the beam warping, hence some under-sampling artifacts remains. This can also be seen from the STB offset at focal depth, which is a bit larger than the dynamic steering offset. Higher order interpolation would be required to correct for this.

In the remaining column, tabulating the peak value offset from the expected position, it is interesting to notice that the STB method performs better than dynamic steering both before and after focus. This can probably be contributed to two things. Firstly the ability of the STB method to correct for skewness in the beam profiles, which will be a prominent cause of artifacts in these regions. Secondly the Gaussian beam approximation used for estimating beam warping will be poor at depths outside the focal zone, causing the dynamic steering method to fail at these depths. The STB method will correct for warping at all depths independent of beam approximations. The J. N. Wright method is seen to yield results not quite as good as the STB method outside the focal depth.
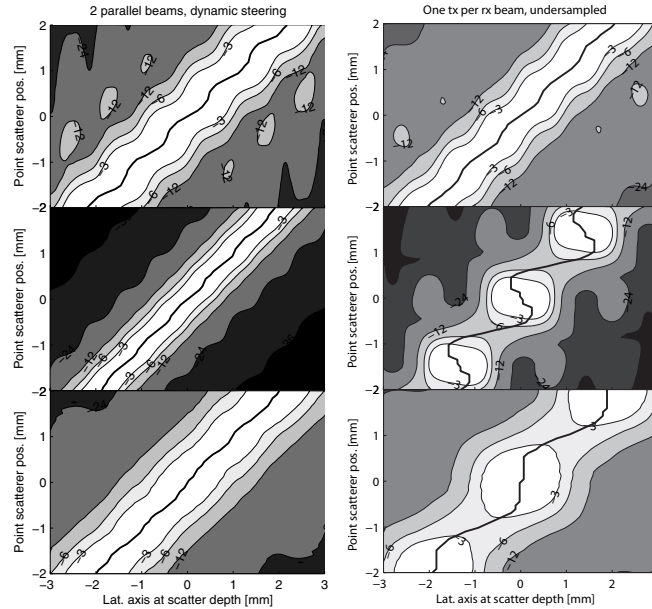
Figure 2.12: Left column: dynamic steering is used to compensate for warping at all depths. Compare this to the results from compensating at the focal depth only, shown in Fig. 2.11. No experimental results are available due to limitations in the available ultrasound hardware. Right column: The easiest way to increase the acquisition rate is simply to decrease the scan line density. Here the result from using the same transmit beam density as in the other plots is shown, but with only one parallel beam. This results in two-way under-sampling, as can clearly be seen from the middle and bottom pane.

## 2.6 Concluding Remarks

From the results presented above it is clear that straightforward parallel beamforming reduces the spatial shift invariance of an ultrasound imaging system. Some compensation approaches have been investigated, and the proposed method of using synthetic transmit beams seems to give a more spatial shift invariant imaging system, with the benefit of increased acquisition rate. However this comes at the cost of additional beamformers.

Dynamic steering also seems like a promising technique, even though it does not compensate for all parallel beam artifacts as the STB method does. The benefit of this technique over STB is that the same number of scan lines as available beamformers is obtained.

Note that significantly less spatial variance from parallel receive beam operation can be obtained by increasing the transmit beam density and/or increasing the transmit f-number. The penalty for doing so is decreased acquisition speed in the case

of increased transmit beam density. The main drawback of increasing the transmit f-number is reduced penetration. Additionally it will give a wider transmit focus, giving poorer resolution.

It is worth noting that different underlying phenomena contribute to the artifacts at increasing depth. In the region close to the transducer the skewing effect is the dominant artifact. In the focal region the warping effect dominates, while deeper in the image both effects contribute.

# References

[1] O. T. von Ramm, S. W. Smith, and H. G. Pavy, "High-speed ultrasound volumetric imaging system – part ii: Parallel processing and image display," *IEEE transactions on ultrasonics, ferroelectrics, and frequency control*, vol. 38, March 1991.

[2] D. P. Shattuck, M. D. Weinshenker, S. W. Smith, and O. T. von Ramm, "Explososcan: A parallel processing technique for high speed ultrasound imaging with linear phased arrays," *J. Acoust, Soc. Amer.*, vol. 75, no. 4, pp. 1273–1282, 1984.

[3] L. J. Augustine, *High resolution multiline ultrasonic beamformer*. United States Patent 4.644.795, 1987.

[4] N. Wright *et al.*, *Method and apparatus for coherent image formation*. United States Patent 5.623.928, 1997.

[5] J. A. Jensen, "Field: A program for simulating ultrasound systems," *Medical & Biological Engineering & Computing*, 1996.

[6] J. N. Wright, *Image formation in diagnostic ultrasound*. IEEE international ultrasonics symposium short course, 1997.

[7] M. Kowalski, T. Kukulski, F. Jamal, J. D'Hooge, F. Weidemann, F. Rademakers, B. Bijnens, L. Hatle, and G. R. Sutherland, "Can natural strain and strain rate quantify regional myocardial deformation? a study in healthy subjects," *Ultrasound in Med. & Biol.*, vol. 27, no. 8, pp. 1087–1097, 2001.

[8] T. L. Szabo, *Diagnostic ultrasound imaging inside out*. Elsevier academic press, 2004.

[9] J. G. Proakis and D. G. Manolakis, *Digital Signal Processing. Principles, Algorithms, and Applications*. London: Prentice Hall, third ed., 1996.

[10] K. E. Thiele and A. Brauch, *Method and apparatus for dynamically steering ultrasonic phased arrays*. United States Patent 5.322.068, 1994.

# Chapter 3

# The Impact of Aberration on High Frame Rate Cardiac B-Mode Imaging

T. Bjåstad and S. A. Aase, and H. Torp
Dept. Circulation and Medical Imaging, NTNU

In echocardiography, especially in 3D echocardiography, achieving high frame rates is a major challenge. A suggested solution is parallel receive beamforming. Without any compensation, this approach is known to produce block-like artifacts, where each block corresponds to one parallel receive group. In this work, in vitro imaging, in vivo imaging, and simulations were used to investigate the artifacts. In vitro, imaging a tissue phantom, the artifacts were successfully compensated for. However, in vivo, imaging the heart, the compensation techniques no longer sufficed and the artifacts persisted. With in vivo imaging, aberrating tissue layers are present between the heart and the probe. To investigate the effects of aberration on a parallel receive system, an in vitro experiment was performed with and without a silicon phase aberrator in front of the probe. The aberrator caused the artifacts to appear even when compensation techniques were applied. Simulations confirmed the measured results and indicated that distorted beam profiles and decorrelation between parallel receive groups caused the artifacts. To quantify the magnitude of the artifacts, a correlation-based indicator was developed. The indicator separated images with and without artifacts and confirmed that the artifacts appeared from the combination of parallel receive beams and aberration.

## 3.1 Introduction

To study deformation in all phases of the cardiac cycle, sufficient temporal resolution, frame rate, is needed. Using 3D ultrasound, far more data have to be recorded in the same amount of time, thus making it more challenging to achieve a high frame rate.

To achieve high frame rates and still keep sufficient spatial resolution, parallel

71

receive beams can be applied [1, 2]. Using parallel receive beams, multiple scan lines are acquired for each transmit event, hence increasing the frame rate. Parallel beamforming is therefore also known as multiple line acquisition (MLA). As described in [3–5] this technique has some challenges due to misalignment of the transmit and receive beams. If not compensated for, this causes block-like artifacts in the B-mode images and also a periodical lateral gain variation pattern. These effects will be referred to as MLA artifacts.

Several compensation methods have been proposed. In U.S. patents [3] and [6], the authors describe incoherent methods for beam interpolation applied after detection of the RF signal. These methods take nonuniform lateral distribution of two-way beam profiles and gain variation into account. In [4], coherent interpolation is used to produce synthetic scan lines in between the original ones, taking advantage of the fact that the lateral bandwidth increases in the detection step. This increases the beam density and thereby reduces the required number of MLA channels. Another method for MLA correction is described in [5], where synthetic transmit beams are generated in the direction of each receive beam by interpolating the RF-signal from each transducer element prior to receive beamforming. Coherent interpolation between scan lines from different transmit pulses is sensitive to rapid motion. This limits the applicability of the two latter methods in cardiac imaging. A solution with dynamic beam steering is suggested in [7]. In this solution the receive focusing is steered dynamically in the lateral direction to compensate for the nonuniform lateral distribution of two-way beam profiles.

When imaging the heart, the transmit and receive beams of an ultrasound system will be distorted due to inhomogeneities in the body wall. This phenomenon is known as aberration. MLA systems require a specific geometric relation between the transmit and receive beams. Since aberration distorts the beams, it is likely that aberration will have an effect on the ability to correct for MLA artifacts.

We show that cardiac in vivo MLA images contain block artifacts even when beam steering and gain compensation techniques are used. A major difference between in vitro images, where compensation is successful, and cardiac images, where compensation fails, is aberration. In this paper we therefore investigate the impact of aberration on MLA imaging systems, suggesting that aberration is a major reason for failing compensation in cardiac MLA images.

The outline of this investigation is as follows: First, the artifacts of MLA are explained and demonstrated in vivo. Having established the problem, it is shown that these artifacts can be corrected when imaging a tissue mimicking phantom where no aberration is present. When placing a thin silicon aberrator between the probe and phantom, it is shown that the compensation techniques no longer suffice. Further, the effects and mechanisms of aberration in conjunction with MLA are investigated through simulations and correlation analysis.

72

## 3.2   Theory

### 3.2.1   Multi-Line Acquisition

The transmit and receive directions of an MLA setup are illustrated in Fig. 3.1. Thin lines indicate receive directions and thick lines the transmit directions. Several receive scan lines are formed in parallel for each transmit event and constitute an MLA group. An MLA system with four parallel receive lines in each MLA group will be referred to as a 4MLA system.
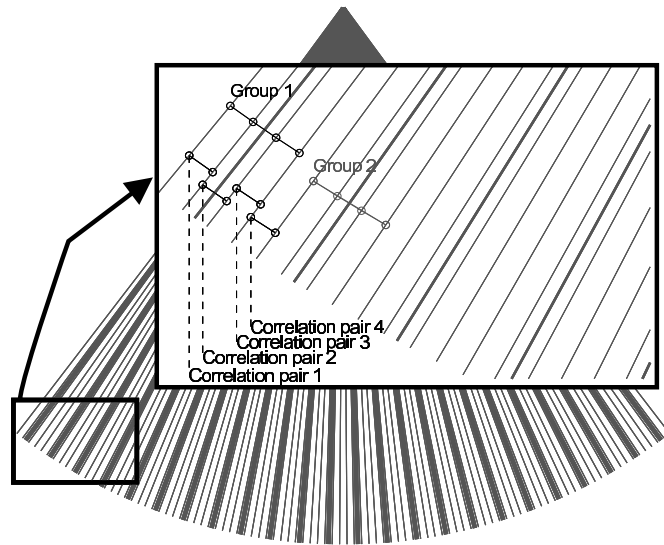


Figure 3.1: 4MLA ultrasound scan grid with Tx lines (thick) and Rx lines (thin). Magnified section: Part of ultrasound scan grid with visualization of MLA groups and scan line correlation pairs.

As described in [5], MLA image artifacts are caused by the misalignment of the transmit and receive beams. The misalignment pulls the lateral maximum of the two-way beam profiles toward the transmit beam lateral maximum. This causes irregular overlaps between adjacent two-way beam profiles. If not compensated for, there will be a gap in the sampling between the MLA groups and hence irregular sampling. This effect is referred to as warping and causes sharp lateral discontinuities in the image. The discontinuities can be seen as the edges of the block artifacts in the images. As proposed by [7], this warping can be compensated for by steering the receive beams an appropriate amount away from the transmit beam. This will result in more regular lateral sampling. Since the warping effect varies with depth, this steering should ideally be dynamic. However, a static steering offset will be sufficient as long as the beam widths of the transmit and receive beams are constant over the relevant depth range.

Another effect of the transmit-receive misalignment is that the shape of the beam profiles is asymmetric and changes from beam to beam within an MLA group. The variation in shape will result in a variation in overlap between adjacent two way beam profiles. This effect is referred to as skewing.

A third effect is that the outermost two-way beams in a 4MLA group have a lower sensitivity than the innermost. This causes a periodical lateral gain variation pattern in the image. The lateral gain variation pattern can be compensated for based either on a priori knowledge of the transmit and receive beams or on the measured gain variations in the recording. In the first approach, based on a priori knowledge, the gain compensation can be found by integrating two-way beam profiles. Estimating the gain variations from the recordings can be done in several ways. A straight forward technique is to calculate the relative gain variations internally in each MLA group. Averaging these internal variations for MLA groups in all positions, depths and frames will give a set of gain compensation values relatively independent of the imaged object. This method produces a number of gain compensation values equal to the size of an MLA group. A prerequisite for using only these compensation values is that the gain variations be constant throughout the image. This again requires the transmit and receive beam width to be constant. This will in most cases only be valid in a limited area (roughly equal to the depth of focus).

### 3.2.2 Correlation Analysis

The most important contributor to MLA artifacts is assumed to be irregular overlap between adjacent two way beam profiles. This causes irregular sampling of the imaged object. With correlation analysis of each pair of adjacent scan lines, the distribution of correlation values will be related to the regularity of the sampling. With regular sampling, all pairs should show similar correlation. In the case of irregular sampling, different pairs will have different correlation. To detect differences in correlation, the correlation values of each pair must be compared with the other pairs. A likelihood ratio test can be performed to find sufficient statistic for separating two different correlation values.

Letting $X = [x_1, x_2]$ where $x_1$ and $x_2$ are complex demodulated RF data from two adjacent scan lines, and modeling the signal as a zero mean complex Gaussian process, the probability density function is

$$p(X) = \pi^{-2}|C|^{-1}e^{X^H C^{-1}X}. \tag{3.1}$$

(From Eq. 15.17 in [8].) Assuming equal variance, $\sigma^2$, the covariance matrices under hypothesis $H_0$ and $H_1$ are

$$H_0 : C_0 = \sigma^2 \begin{bmatrix} 1 & \rho_0 \\ \rho_0^* & 1 \end{bmatrix}$$

and

$$H_1 : C_1 = \sigma^2 \begin{bmatrix} 1 & \rho_1 \\ \rho_1^* & 1 \end{bmatrix},$$

where $\rho_0$ and $\rho_1$ are different real positive numbers representing two different normalized cross correlation factors. $H_0$ could, for instance, represent a pair with high cross correlation whereas $H_1$ could represent a pair with low cross correlation.

The likelihood ratio is defined in Eq. 13 in [9] as

$$\Lambda(X) = \frac{p_{x|H_1}(X|H_1)}{p_{x|H_0}(X|H_0)} \tag{3.2}$$

The log likelihood ratio using Eqs. 3.1 and 3.2 reduces to

$$log(\Lambda(X)) = b \cdot (\hat{R}_{11} + \hat{R}_{22}) \cdot \left(1 - c \cdot \frac{2Real(\hat{R}_{12})}{\hat{R}_{11} + \hat{R}_{22}}\right), \tag{3.3}$$

where $b$ and $c$ are constants given by $\rho_0$ and $\rho_1$ and $\hat{R}_{ij} = \frac{1}{d} \sum_{r=n-d}^{n-1} x_i(r) x_j^*(r)$.

The $\hat{R}_{ij}$ estimate is calculated as correlation between data at scan lines $i$ and $j$ at $d$ depths given by sample numbers $r$. When averaging over several depths, $\hat{R}_{11}$ and $\hat{R}_{22}$ are approximately constant, and the latter part of the expression becomes a sufficient statistic. The correlation coefficient, being an optimal test for separating two different correlation values, then becomes:

$$C_c = \frac{2Real(\hat{R}_{ij})}{\hat{R}_{ii} + \hat{R}_{jj}}. \tag{3.4}$$

Due to the normalization, $C_c$ will range from 0, when no correlation is found between the scan lines, to 1, when full correlation is found between the scan lines.

$C_c$ can be calculated for each adjacent pair of scan lines as shown in Fig. 3.1. To compensate for gain variation along the scan lines, $C_c$ can be calculated in sections along the scan lines and then averaged. The calculated final $C_c$ for each scan line pair can be visualized in a $C_c$ plot representing all scan line pairs.

$C_c$ values and $C_c$ plots contain information concerning the correlation from scan line to scan line. Of special interest regarding MLA are $C_c$ values at transitions between MLA groups compared to $C_c$ values within MLA groups. To get a single quantitative measure for this, an indicator of fractional correlation coefficient difference, $D_c$, can be calculated as:

$$D_c = \frac{\frac{1}{N} \sum_{ij \in W} C_c - \frac{1}{M} \sum_{ij \in T} C_c}{\frac{1}{N} \sum_{ij \in W} C_c} \cdot 100, \tag{3.5}$$

where $ij$ is a pair of adjacent scan lines. The set $W$ contains all such pairs within MLA groups, and the set $T$ contains all such pairs located at transitions between MLA groups (such as correlation pair 4 in Fig. 3.1). $N$ is the size of the set $W$, and $M$ is the size of the set $T$. $D_c$ will be 0 when no repeating difference in correlation within and

| Table 3.1: Scan setup | |
| --- | --- |
| Transmit frequency | 2.5 MHz |
| Receive frequency | 2.5 MHz |
| # receive lines | 96 |
| Sector width | 75 deg |
| Beam spacing | 0.79 deg |
| Transmit aperture width | 7.5 mm |
| Receive aperture width | Expanding (max: 2.19 cm) |
| Transmit apodization | Rectangular |
| Receive apodization | Hamming |
| Transmit focus | 70 mm |
| Receive focus | Dynamic |

between MLA groups is present. When there is full correlation within MLA groups and no correlation between MLA groups, it will be 100.

## 3.3 Setup

An M3S probe and a GE Vingmed System 7 scanner capable of recording RF data was set up with the specifications given in Table 4.1. Using this setup both 4MLA and single line acquisition (SLA) were implemented. The setup was designed to be able to compensate for the negative effects of MLA. Hamming apodization on receive lowers the side lobes. This results in less skewing due to more symmetric two way beam profiles. The small transmit aperture also reduces the skewing effect due to wider transmit beams. In addition, it results in a long focus, hence enabling good compensation for the warping and gain variation effect over a long depth range. The distribution of transmit and receive scan lines is visualized in Fig. 3.1. The warp compensation was implemented by steering the inner beams of the MLA groups an additional 14% of the beam spacing away from the transmit beam directions and the outer beams of the MLA groups an additional 42%. The compensation steering offsets were found through simulations of the described setup.

The recorded RF data were processed to B-mode display by detection, time gain compensation, log compression, and scan conversion. A 40-dB dynamic range was used in the images.

Using the described setup, an ultrasound phantom (CIRS Model 40, General Purpose Multi-Tissue Ultrasound Phantom, 0.5 dB/cm/Mhz; CIRS, Inc., Norfolk, VA) was imaged while tilting the probe from side to side. The left ventricle (LV) of the heart of a healthy adult subject was also imaged.

To isolate the effects of aberration, a thin silicon aberrator, described in [10], was placed between the probe and the phantom for some recordings. This was a pure time-delay aberrator with a RMS time delay of 48.5 ns. This is similar to RMS time delays found in [11]. Since the RMS delay value for this aberrator corresponded to an abdominal body wall, a scaled-down version of the aberrator was also tested in

simulations. The RMS delay value of this scaled aberrator was set to 21.1 ns. This corresponds to typical values for thoracic body walls [12]. The correlation lengths of both aberrators were also in the range of typical thoracic body walls (2.47 mm) [12].

The described setup, aberrators, CIRS phantom, and a left ventricle computer model were also simulated in Matlab using Field II [13]. The left ventricle computer model is described in [14]. When gain compensation was applied, the gain compensation values were estimated from the recorded data and applied to the RF data before further processing.

To produce a quantitative analysis of the images, $C_c$ values between neighboring beams were calculated (a total of 95 pairs) using data from all frames of the recordings. To emphasize the difference in $C_c$ values between scan lines within MLA groups and between groups, every fourth $C_c$ value is colored brighter in the bar plots. $C_c$ analysis was performed after the data were gain corrected.

Since the gain and warp compensation are valid only throughout the depth of focus, only data from the lower 2/3 part of each image were used when estimating both gain compensation and $C_c$ values. The extent of this area is illustrated by a gray bar at the left side of the ultrasound sector in all images.

## 3.4   Results

All B-mode images in this section are also available as videos. The videos provide a far better impression of the described artifacts than the still images. These will be referred to with file names and can be found at *www.ntnu.no/us/ThesisMM/bjastad.*

### 3.4.1   Measurements

With the described 4MLA setup, a frame rate of 163 frames/s was achieved on the scanner. An image of the left ventricle of a healthy adult subject acquired using this setup without warp compensation is shown in Fig. 3.2. Notice the block-like appearance.

Images of the CIRS phantom are presented in Figs. 3.3 and 3.4. In Fig. 3.3, the phantom was imaged using the 4MLA setup without warp and gain compensation. The block artifacts are observable in the image/video. The $C_c$ plot shows a repeating pattern of three high $C_c$ values followed by a lower $C_c$ value. In Fig. 3.4, the described gain and warp compensation has been applied. No lateral block artifacts can be seen in this image, and the repeating pattern of three high $C_c$ values followed by a lower $C_c$ value is not present.

A cardiac ultrasound image with gain and warp compensation using the described 4MLA setup is shown in Fig. 3.5. The block artifacts are not as obvious as in Fig. 3.2, but they are still visible. When the $C_c$ plot is observed, the repeating pattern of three high $C_c$ values followed by a lower $C_c$ value is evident. Using SLA but otherwise the same setup produced the image in Fig. 3.6. There is no repeating pattern in the corresponding $C_c$ plot.
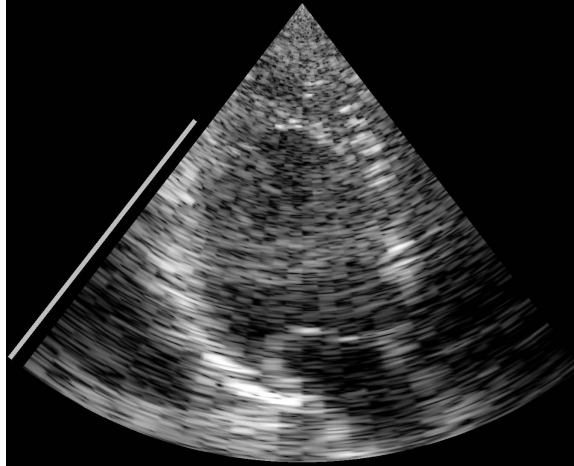
Figure 3.2: Human left ventricle imaged using the 4MLA setup without warp and gain compensation (*Ch3_Movie01.mpg*)

.

In Fig. 3.7, the aberrator was added to the phantom. The block artifacts appeared in the image. In the corresponding $C_c$ plot, the pattern of three high $C_c$ values followed by a lower $C_c$ value is very obvious.

## 3.4.2 Simulations

To investigate the effect of aberration in a controlled environment, the 4MLA setup, CIRS phantom, left ventricle phantom, and silicon aberrator were implemented in Field II and Matlab. Fig. 3.8 shows the simulated results from imaging the CIRS phantom through the silicon aberrator. The B-mode image shows good correspondence with the recorded B-mode (Fig. 3.7). Fig. 3.9 shows the B-mode image and correlation values from a simulated cardiac situation. In this case, the CIRS phantom was replaced with the left ventricle phantom, and the aberration delays of the silicon aberrator were scaled to match the RMS delay values found in the literature for thoracic body walls. The block artifacts can still be seen in this B-mode image, particularly around the boundary of the ventricle model.

In the aberrated cases in all remaining figures, only the silicon aberrator was simulated. Fig. 3.10 shows four adjacent two-way beam profiles using the setup in Table 4.1 in six different imaging cases: SLA with and without aberration, uncompensated 4MLA with and without aberration, and compensated 4MLA with and without aberration. The figure illustrates the beam to beam variations of the beam profiles in the different imaging cases. In the 4MLA cases, the beam profiles of scan lines 47 and 48 belong to MLA group 12, and the beam profiles of scan lines 49 and 50 belong to MLA group 13. In the aberrated 4MLA cases (middle and bottom right plots), it can be seen that both the beam profile spacing and the beam profile
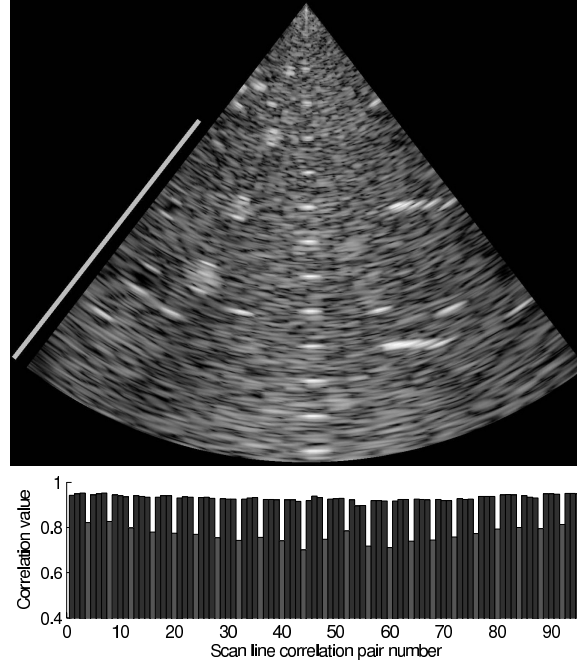
Figure 3.3: Phantom without aberrator imaged using the 4MLA setup without warp and gain compensation (*Ch3_Movie02.mpg*).

shape are varying from beam to beam both before and after compensation.

In Fig. 3.11, the same imaging cases are investigated for lateral shift variance (LSV) of the point spread function (PSF). Such figures will be referred to as LSV plots. The procedure for creating LSV plots is illustrated in Fig. 4.2. First, a point scatterer is imaged as it moves laterally at the focus depth (Fig. 4.2, top). Each image then corresponds to the PSF of the system at the position of the imaged point scatterer. Second, logarithmic radial mean square values of the point scatter images are calculated (Fig. 4.2, middle). Finally, the LSV plots are generated by stacking these logarithmic radial mean square values so that each row in the final LSV plot corresponds to a point scatterer position (Fig. 4.2, bottom). A shift invariant imaging system, where the PSF is independent of the position of the imaged point scatterer, should result in a straight diagonal structure. Deviations from a straight diagonal structure indicate that the PSF varies with lateral position and that the system is shift variant. The strong deviations from a diagonal structure in the bottom right pane of Fig. 3.11 indicate that this imaging system is shift variant. The structures visible in this pane are also similar to the block artifacts observed in the B-mode images.

Fig. 3.13 shows the aberrated beam profiles from three adjacent 4MLA groups. The figure shows on a larger scale the variation and pattern in the two-way beam
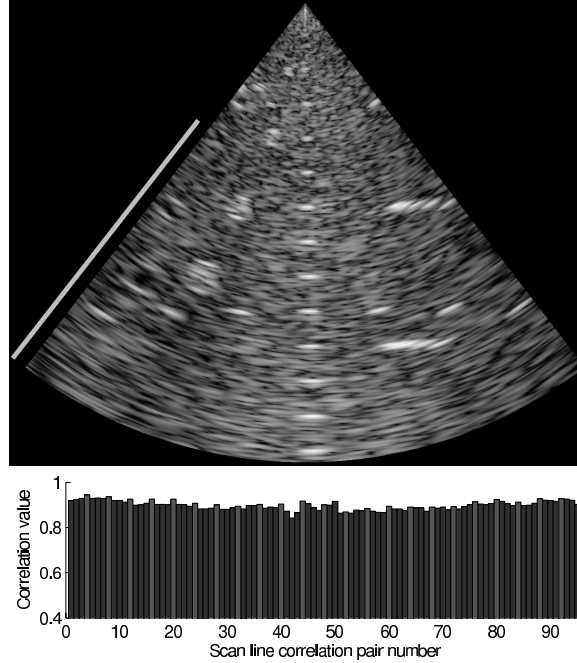
Figure 3.4: Phantom without aberrator imaged using the 4MLA setup with warp and gain compensation (*Ch3_Movie03.mpg*).

profiles.

### 3.4.3  Simulated and Measured $D_c$ Values

The indicator of correlation coefficient difference, $D_c$, was calculated for all images with $C_c$ plots. The results are shown in Table 3.2 where "Phant." denotes measured phantom, "Sim. phant." is simulated phantom, "LV" is the measured left ventricle of a healthy subject, "Sim. LV" is a simulated left ventricle phantom, "ab.1" is aberration by thin silicon aberrator, "ab.C" is the aberration present in cardiac in vivo images, "ab.2" is aberration by thorax-scaled (simulated) silicon aberrator, and "Compensation" is warp and gain compensation.

All 4MLA setups with aberration had $D_c$ values above 11. In the case of SLA with aberration (Fig. 3.6), the $D_c$ value was, of course, low, as the MLA group size for SLA is one and no MLA related pattern was expected. In the case of no aberration and no MLA compensation (Fig. 3.3), a large $D_c$ value was found. When MLA compensation was applied (Fig. 3.4), the $D_c$ value was close to zero.
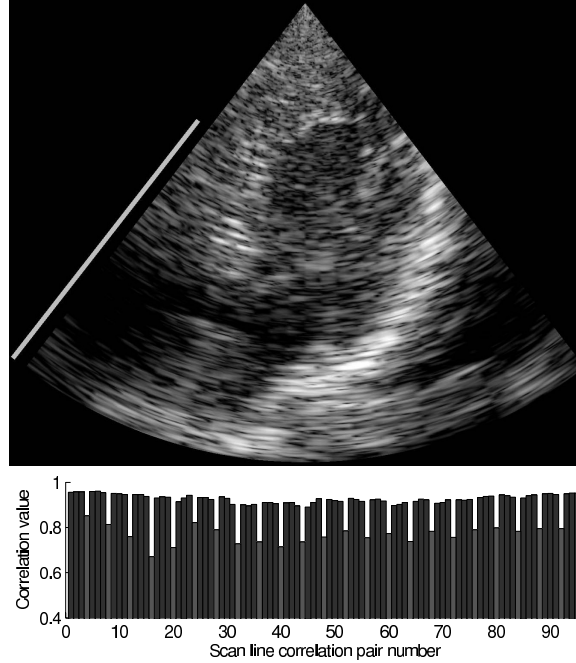
80

Figure 3.5: Human left ventricle imaged using the 4MLA setup with warp and gain compensation (*Ch3_Movie04.mpg*).

Table 3.2: Indicator showing differences in correlation, $D_c$

| Object | Aberration | #MLA | Compensation | Figure | $D_c$ |
|---|---|---|---|---|---|
| Phant. | | 4MLA | No | 3.3 | 17.7 |
| Phant. | | 4MLA | Yes | 3.4 | -1.5 |
| Phant. | ab.1 | 4MLA | Yes | 3.7 | 22.9 |
| Sim. phant. | ab.1 | 4MLA | Yes | 3.8 | 19.8 |
| LV | ab.C | 4MLA | Yes | 3.5 | 17.4 |
| LV | ab.C | SLA | | 3.6 | 0.02 |
| Sim. LV | ab.2 | 4MLA | Yes | 3.9 | 11.6 |

## 3.5   Discussion

The cardiac images recorded using 4MLA (Figs. 3.2 and 3.5) showed block artifacts. Although the artifacts were reduced by using warp compensation (Fig. 3.5), they were still visible.

To first study a simpler situation, a tissue mimicking phantom was used. The results showed that block artifacts in unaberrated 4MLA phantom images can be avoided by using warp and gain compensation (Figs. 3.3 and 3.4). The beam profiles in the two lower left panes of Fig. 3.10 correspond to Figs. 3.3 and 3.4, respectively.
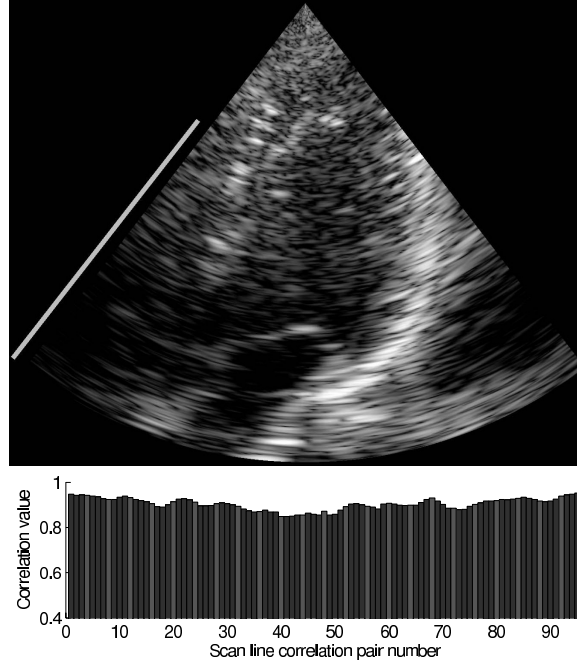
Figure 3.6: Human left ventricle imaged using the SLA setup (96 transmit beams) (*Ch3_Movie05.mpg*).

From the beam profiles, it is evident that warping is the main distorting effect. Skewing is not observable.

To emulate aberration, the thin silicon aberrator was placed between the probe and the phantom. Even though warp and gain compensation was applied, the block artifacts appeared and the $C_c$ plot showed a repeating pattern of three high/one low $C_c$ values (Fig. 3.7). This was the exact same setup as used when imaging the heart (Fig. 3.5). As shown in both images and both $C_c$ plots, the same pattern emerged. This implies that the thin silicon aberrator generates some of the beam manipulating effects that influence cardiac images. Cardiac images without the use of MLA (Fig. 3.6) did not contain block artifacts and corresponding patterns in the $C_c$ plots. These observations suggest that the combination of aberration and MLA cause the block artifacts.

The simulations supported the results from the measurements, showing that the introduction of an aberrator produces pronounced artifacts in the images. With good agreement between simulated and measured results, further insight was obtained from investigations of the aberrated beam profiles.

Fig. 3.10 shows the two-way beam profiles for four adjacent scan lines in six different imaging cases. On the left side, the beam profiles for the unaberrated case are presented. Using SLA (top left plot), the beam profiles are regularly spaced with
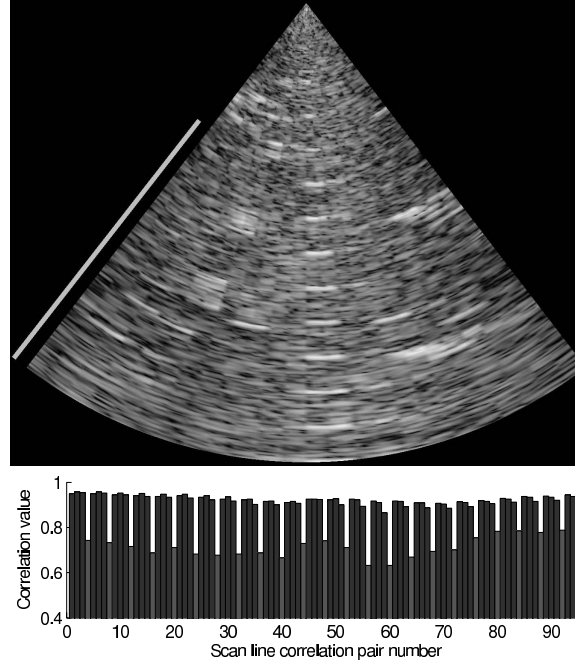
Figure 3.7: Phantom with aberrator imaged using the 4MLA setup with warp and gain compensation (*Ch3_Movie06.mpg*).

maximum sensitivity in the desired steering directions. For the 4MLA case (middle left plot), the beam profiles become irregularly spaced. Scan line 48 and 49 belongs to two different MLA groups. The gap between the beam profiles from these two scan lines results in a decorrelation that appears as a sharp lateral discontinuity in the B-mode image. Several such gaps cause the blocky appearance in the B-mode images. The larger this gap is, the more pronounced the artifacts will be. Such block artifacts and decorrelation can be seen in Fig. 3.3. In the bottom left plot of Fig. 3.10, warp compensation has been applied. Since the beam profiles now once again are regularly spaced, the block artifacts are no longer present in the images (Fig. 3.4). Proceeding to the aberrated SLA case (top right plot), the two-way beam profiles are clearly distorted. However, it is worth noticing that the shape and overlap between each adjacent beam is similar. Regular sampling is thus also achieved for the aberrated case. With regular sampling, the correlation between each adjacent beam will be similar. This is confirmed by the $C_c$ plot in Fig. 3.6. In the middle right plot of Fig. 3.10, the beam profiles for the aberrated, uncompensated 4MLA case are shown. Here, each scan line beam profile is different in shape and the spacing is irregular. One can expect high correlation between scan lines 47 and 48 due to the large overlap between the beam profiles. Similarly, one can expect low correlation between scan lines 48 and 49 due to significantly less overlap. As in the uncompensated 4MLA case
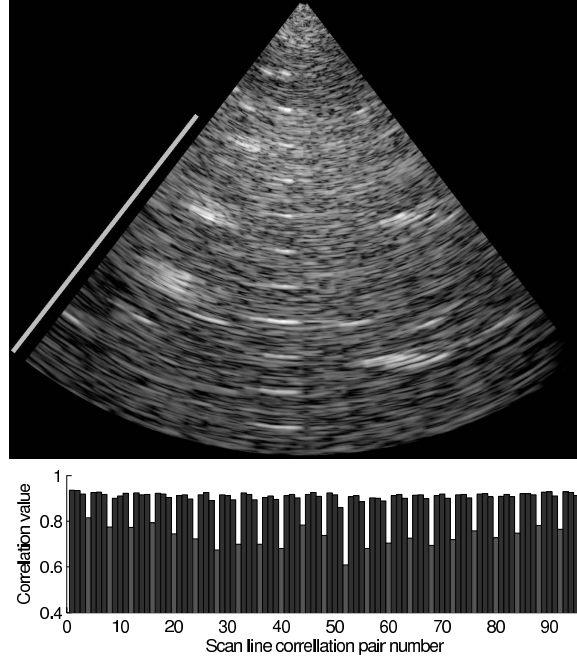
83

Figure 3.8: Phantom with aberrator simulated using the 4MLA setup with warp and gain compensation (*Ch3_Movie07.mpg*).

without aberration, this reduction in correlation will appear in the image as sharp lateral discontinuities between each MLA group, such as seen in the cardiac B-mode image in Fig. 3.2. The bottom right plot in Fig. 3.10 shows the beam profiles for warp-compensated 4MLA with aberration. The compensation results in a slightly more regular spacing of the beam profiles, but the fluctuation in the shape of the beam profiles still remains. Compared to the unaberrated, compensated 4MLA case, the compensation in the aberrated case is far from successful. This can also be seen in the simulated, aberrated B-mode image (Fig. 3.8), where the block artifacts are obvious.

Seemingly, the MLA artifacts were more visible when imaging objects with high dynamic range in the back scattering, such as the left ventricle phantom. The B-mode image of this phantom (Fig. 3.9) was generated using the default scan setup, 4MLA, and thorax-scaled aberration. Despite a significantly weaker aberrator, block artifacts can still clearly be seen in the image, particularly around the boundary of the ventricle model. The explanation for this can be found from the two-way beam profiles in Fig. 3.13. This figure shows two way beam profiles from three adjacent MLA groups in the compensated, aberrated 4MLA case. A beam profile defines the lateral sensitivity of a scan line. With that in mind, consider a point scatterer positioned from an angle around -1.5 degrees to 1.5 degrees. This point scatterer will be perceived approximately
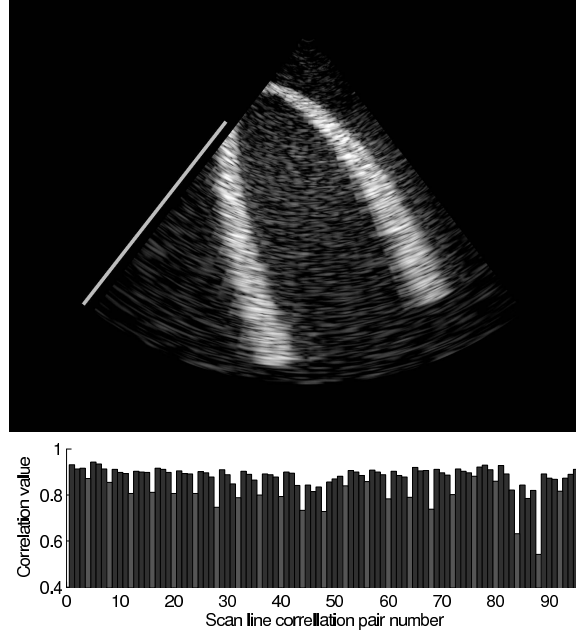
84

Figure 3.9:   Left ventricle model with aberrator scaled according to thoracic delay values simulated using the 4MLA setup with warp and gain compensation (*Ch3_Movie08.mpg*).

equally bright in all of the scan lines generated from the beam profiles in solid line style. In the scan lines generated from the dashed beam profiles, it will, however, be perceived significantly brighter and have different brightness values in each scan line. The result is a lateral plateau of four almost equal brightness values followed by a jump in brightness value. For a point scatterer moving laterally through the scan grid, the resulting pattern is shown in the bottom right pane of Fig. 3.11. When imaging the heart, a situation similar to the one in Fig. 3.9, a transition between two areas with low and high back scattering intensity will produce the same image artifact.

Some areas of the cardiac images and the simulated cardiac situation (Figs. 3.2, 3.5 and 3.9) can give an impression of axial block artifacts. With irregular lateral sampling, the speckle pattern will not be continuous laterally. This may cause an impression of discontinuous speckle in the radial direction. For areas with high dynamic range in the back scattering, the effect can also be explained as a perception of the lateral plateau artifacts described in the previous paragraph.

Fig. 3.11 shows how the point spread function varies in shape as a function of lateral position. The figure contains the same cases as for the beam profiles in Fig. 3.10. In the unaberrated case, the shift invariance property can be restored by warp compensation (from the middle left pane to the bottom left pane). In the aberrated 4MLA case, the compensation does not suffice, and the imaging system remains shift
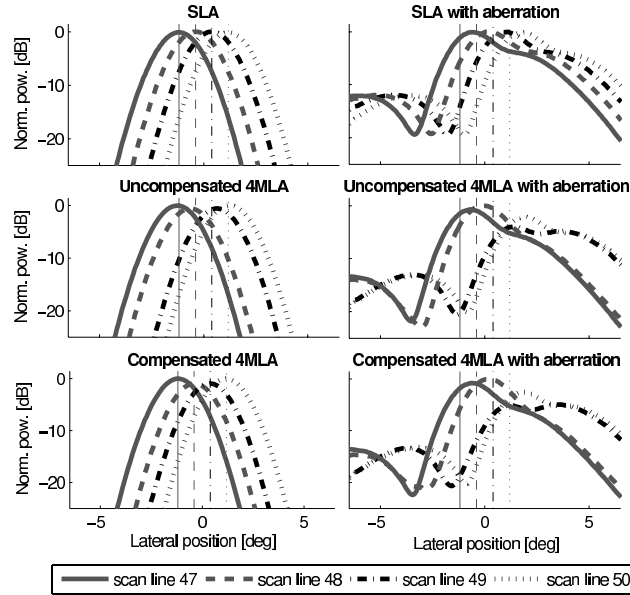
Figure 3.10: Simulated two-way beam profiles from four adjacent scan lines. The applied setup is given in Table 4.1. The vertical lines indicate the desired steering direction of the beam profiles in corresponding line style. Ideally these lines should intersect their beam profiles at their maximum. Left side: Without aberration. Right side: With aberration. Top: SLA. Middle: Uncompensated 4MLA. Bottom: Compensated 4MLA. In the 4MLA cases, the beam profiles in solid and dashed line style are the two last beams in a 4MLA group. The beam profiles in dash-dotted and dotted line style are the first two beams from the adjacent 4MLA group. Notice that with the combination of 4MLA and aberration, each scan line beam profile is different in shape, has different gain, and has irregular spacing.

variant (middle right pane and bottom right pane). This confirms the measured results.

Both the measured and simulated results showed that repeating patterns in the $C_c$ plots were related to the presence of block artifacts in the corresponding B-mode images. The $D_c$ values shown in Table 3.2 quantify the magnitude of these patterns and confirm the impression from images and $C_c$ plots. The situation with 4MLA without aberration (Fig. 3.4) produced a negative $D_c$ value. This indicates that the correlation at transitions between MLA groups was stronger than within the MLA groups. The reason for this might be overcompensation for the warping effect.

Larger $D_c$ values were measured with the aberrated phantom images than in the cardiac images. This was probably because the RMS delay values of the silicon aberrator were from abdominal measurements. To investigate a cardiac imaging situation, the aberrator was scaled to thoracic RMS delay values in simulations and used to image the left ventricle computer phantom. The resulting image and $C_c$
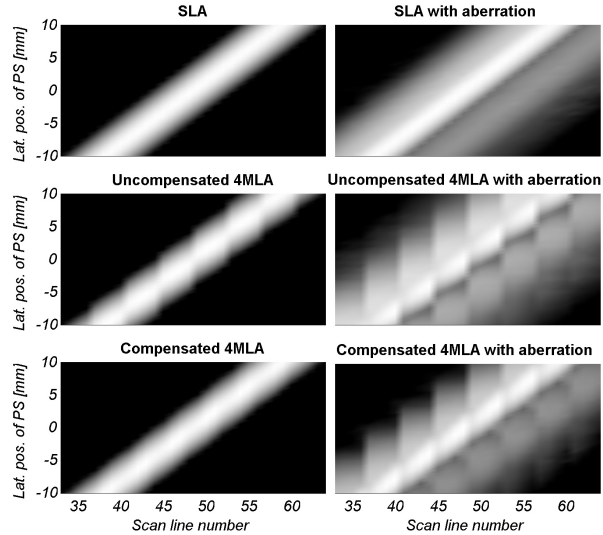
Figure 3.11: Lateral shift variance plots. Left side: Without aberration. Right side: With aberration. Top: SLA. Middle: Uncompensated 4MLA. Bottom: Compensated 4MLA. All figures are displayed with a 40-dB dynamic range.

plot (Fig. 3.9) still showed block artifacts. The $D_c$ value was, however, lower than in the measured cardiac case. A reason for this might be that aberrations from a thick body wall were approximated with a single phase screen at the face of the transducer. Results from [15, 16] show that this approximation models only parts of the total aberration. Another reason might be further aberrations from structures beyond the body wall. A third reason might be reverberations. In the in vivo recording, reverberations with evident block artifacts were visible within the cavity. Such effects were not included in the simulations. Additionally, the LV phantom is a coarse approximation of an in vivo left ventricle. All of these factors may have contributed to make the $D_c$ value of the simulated cardiac situation lower than in the measured situation.

The $D_c$ value and corresponding $C_c$ plot of Fig. 3.3 show that warping alone (no skewing present, see Fig. 3.10, middle left) will cause measurable decorrelation. Aberration in combination with MLA produces both warping and skewing effects and results in measurable decorrelation (Figs. 3.5, 3.7, 3.8, 3.9 and beam profiles in Fig. 3.10, lower right). The isolated effect of skewing on decorrelation has not been investigated. Although the $D_c$ value of Fig. 3.3 was high, block artifacts in the image were weak but observable. This might be related to the absence of skewing, but also possibly to the uniformity of the imaged object. In Fig. 3.8 (strong aberrator, relatively uniform phantom) and Fig. 3.9 (weak aberrator, non uniform phantom), the block artifacts are approximately equally visible. This indicates that the block artifacts are more easily detected visually in images of non uniform objects.
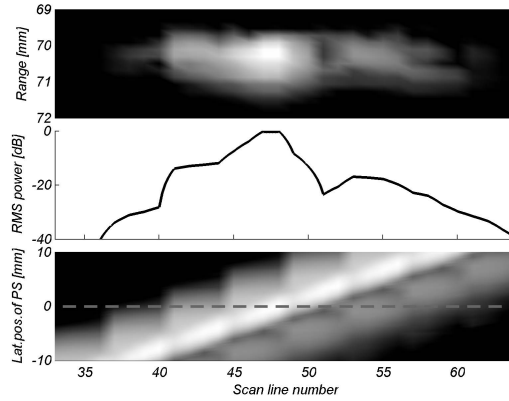
Figure 3.12: Illustration of how LSV plots are generated. Top: Image of a point scatterer at a lateral position at focus depth. Middle: Radial mean square value of the point scatterer image. Bottom: Stacked radial mean square values for several point scatterer positions. The dashed line indicates the position of the radial mean square value in the middle pane.
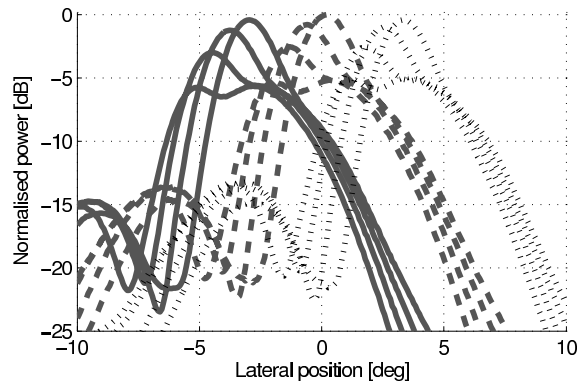


Figure 3.13: Two-way beam profiles from three adjacent 4MLA groups. The simulation setup was 4MLA with aberration and warp compensation. Group 11 plotted in solid, group 12 in dashed and group 13 in dotted line style.

## 3.6 Conclusions

Simulations and in vitro experiments showed that aberration in combination with parallel beamforming caused block artifacts similar to the artifacts observed in cardiac parallel beamforming images. Gain and beam steering compensation successful in non-aberrated in vitro cases failed in aberrated in vitro cases.

During investigation of simulated beam profiles, two underlying mechanisms were

identified. The first mechanism was irregular sampling and decorrelation. This was caused by aberration distorting and pulling the beam profiles out of the original scan grid, leaving gaps between the parallel receive groups. Second, the asymmetric and variable shape of the beam profiles caused a stair-like gain variation in transitions between imaged areas with low and high intensity.

## Acknowledgement

# References

[1] D. P. Shattuck, M. D. Weinshenker, S. W. Smith, and O. T. von Ramm, "Explososcan: A parallel processing technique for high speed ultrasound imaging with linear phased arrays," *J Acoust Soc Amer*, vol. 75, no. 4, pp. 1273–1282, 1984.

[2] O. T. von Ramm, S. W. Smith, and H. G. Pavy, "High-speed ultrasound volumetric imaging system – part II: Parallel processing and image display," *IEEE Trans Ultrason Ferroelectr Freq Control*, vol. 38, pp. 109–115, March 1991.

[3] G. L. Holley and I. M. Guracar, "Ultrasound multi-beam distortion correction system and method." U.S. Patent 5.779.640, July 14 1998.

[4] J. N. Wright, S. H. Maslak, D. J. Finger, and A. Gee, "Method and apparatus for coherent image formation." U.S. Patent 5.623.928, Apr. 29 1997.

[5] T. Hergum, T. Bjåstad, and H. Torp, "Parallel beamforming using synthetic transmit beams," *Proc IEEE Ultrason Symp*, vol. 2, pp. 1401–4, 2004.

[6] D.-L. D. Liu, J. C. Lazenby, Z. Banjanin, and B. A. McDermot, "System and method for reduction of parallel beamforming artifacts." U.S. Patent 6.447.452, Sep. 10 2002.

[7] T. J. Hunt, B. M. Herrick, K. K. Robertson, and J. M. Ziel, "Ultrasonic imaging system using line splicing and parallel receive beam formation." U.S. patent 5.462.057, Oct. 31 1995.

[8] S. M. Kay, *Fundamentals of Statistical Signal Processing: Estimation Theory*. Indianapolis, IN: Prentice-Hall PTR, 1993.

[9] H. L. V. Trees, *Detection, Estimation and Modulation Theory, Part I: Detection, Estimation, and Linear Modulation Theory*. New York: Wiley, 2001.

[10] T. F. Johansen, B. A. J. Angelsen, and W. Nordhøy, "Phase aberrations - Experiments and simulations," *Proc 23rd Scand Symp Phys Acoust*, pp. 57–60, 2000.

[11] L. M. Hinkelman, D.-L. Liu, L. A. Metlay, and R. C. Waag, "Measurements of ultrasonic pulse arrival time and energy level variations produced by propagation through abdominal wall," *J Acoust Soc Am*, vol. 95, no. 1, pp. 530–541, 1994.

[12] L. M. Hinkelman, T. L. Szabo, and R. C. Waag, "Measurements of ultrasonic pulse distortion produced by human chest wall," *J Acoust Soc Am*, vol. 101, no. 4, pp. 2365–2373, 1997.

[13] J. A. Jensen and N. B. Svendsen, "Calculation of pressure fields from arbitrarily shaped, apodized, and excited ultrasound transducers," *IEEE Trans Ultrason Ferroelectr Freq Control*, vol. 39, pp. 262–267, 1992.

[14] S. Rabben, A. Haukanes, and F. Irgens, "A kinematic model for simulating physiological left ventricular deformation patterns - a tool for evaluation of myocardial strain imaging," *Proc IEEE Ultrason Symp*, pp. 134–7, 2003.

[15] L. M. Hinkelman, T. D. Mast, L. A. Metlay, and R. C. Waag, "The effect of abdominal wall morphology on ultrasonic pulse distortion. part i. measurements," *J Acoust Soc Am*, vol. 104, no. 6, pp. 3635–3649, 1998.

[16] T. D. Mast, L. M. Hinkelman, M. J. Orr, V. W. Sparrow, and R. C. Waag, "Simulation of ultrasonic pulse propagation through the abdominal wall," *J Acoust Soc Am*, vol. 102, no. 2, pp. 1177–1190, 1997.

# Chapter 4

# Synthetic Transmit Beam Technique in an Aberrating Environment

T. Bjåstad and H. Torp
Dept. Circulation and Medical Imaging, NTNU

Parallel beamforming is a common method for increasing the frame rate in ultrasound imaging systems. By receiving in several directions for each transmit event, the frame rate is increased. However, this method also introduces block-like artifacts in the B-mode image due to the receive offsets compared to the transmit direction. The synthetic transmit beam technique, STB, has previously been proposed as a compensation technique to address these artifacts by creating synthetic transmit beams in each of the receive directions. Previous work by Hergum et al. investigated the performance of this method in the case of two parallel beams in tissue mimicking phantoms without aberrations.

This study is a continuation of that work, where the method is tested in an aberrating environment using four parallel beams. Several quantitative and qualitative performance aspects of the method has been investigated: Lateral shift invariance, beam to beam correlation fluctuations, speckle tracking performance, improvements from higher order STB interpolation, beam profile shape preservation as well as perceived image quality improvements. The results were obtained from simulations, *in vivo* and *in vitro* measurements.

The results showed that aberration amplified the image artifacts for regular parallel beamforming, resulting in more shift variance, lower beam to beam correlation, higher speckle tracking error and more variation in beam profile shape. Compared to regular parallel beamforming, STB resulted in significantly better image quality and a higher score in all measuring methods. The improvements from using STB were largest in the cases with aberration. Here, the variation in beam to beam correlation was reduced from 30% to 1% using STB.

## 4.1 Introduction

Increased frame rate is desirable in a number of ultrasound applications, particularly in cardiac three-dimensional imaging, but also in several two-dimensional applications. One example is duplex and triplex imaging, where several imaging modes are running simultaneously, such as B-mode, color flow and PW-Doppler. Compounding will also benefit from increased acquisition speed, as will multi-plane B-mode imaging, where several 2D B-mode scan planes are acquired simultaneously using a 2D array. High frame rates are also required for accurate tracking of cardiac tissue [1].

A common technique for increasing the frame rate is parallel beamforming [2, 3]. Using this technique, several scan lines are acquired in parallel from each transmit event. Parallel beamforming is therefore also known as multi-line acquisition (MLA). This technique increases the frame rate proportional to the number of parallel receive beams, but, as shown in [4, 5], the method also introduces artifacts in the images, typically giving them a blocky appearance. Such artifacts will be referred to as MLA artifacts.

The source of these artifacts is the inherent misalignment of the transmit and receive beams. The interaction between the transmit and receive beams when they are not pointing in the same direction causes distortions of the two-way beam profiles. These distortions can be split into two components: Warping and skewing. The warping effect causes the maximum point of the two-way beam profile to be shifted towards the transmit beam direction (in other words, the two-way beam direction is not the same as the receive beam direction). This results in a non-uniform lateral sampling of the imaged object. The skewing effect causes the two-way beam profiles to be asymmetrical. In addition, sensitivity is decreased as the receive beams are steered away from the transmit beam main lobe direction, resulting in gain variations [4, 5]. Since the warping, skewing and gain variation are related to beam geometry, they will be depth dependent. The severity of the effects will depend on how much the receive direction is offset compared to the transmit direction; hence the two-way beam profile shape will be different from scan line to scan line. The severity also depends on the width of the transmit beams relative to the receive beams. Reducing the transmit aperture will increase the beam width and thus reduce the warping and skewing [6]. However, it will also reduce penetration and resolution.

It is likely that the MLA artifacts will decrease the performance of speckle tracking. As shown in [5], parallel beamforming imaging systems will be shift variant, i.e. the image of a point scatterer will be dependent on its position. Speckle tracking methods assume that the speckle pattern is preserved during tissue movement. Shift variance will most likely reduce the validity of this assumption.

Several techniques have been proposed to compensate for MLA artifacts. In [7], a transmit sinc apodization was proposed to obtain a transmit beam with a rectangular shape. This would reduce the warping effect, but the skewing effect would still be present. Also, both resolution and penetration would be reduced due to the reduced effective transmit aperture.

In US Patents 5779640 [8] and 6447452 [9], the authors describe incoherent methods for beam interpolation applied after detection of the RF signal. These methods

compensate for warping by interpolating from a non-uniform scan grid to a regular scan grid before display. These methods do not compensate for skewing.

Another compensation technique is presented in US Patent 5462057 [10]. In this patent, the authors propose dynamic steering of the receive beams to counteract the warping effect throughout the imaging depth. However, this does require prediction or estimation of the warping at all depths. It will also increase skewing due to the increased receive offset.

The technique that has been investigated in this study is the synthetic transmit beam technique, STB. This technique reduces the effect of both skewing and warping and has previously been described in [5] and US Patent 5318033 [11]. The basic principle is to create synthetic transmit beams in all parallel receive directions. Ideally, this eliminates the effect of the transmit-receive offset in parallel beamforming. In [5], Hergum et al. showed that this technique strongly reduced MLA artifacts for two parallel beams in tissue mimicking phantoms without aberrations.

Due to inhomogeneities in the body wall, transthoracic imaging will always be affected by some degree of aberration. This aberration can result in distortions and asymmetry in the beam profiles.

Previous work presented in [4] applied a steering compensation method to reduce MLA artifacts. This method was similar to the dynamic steering method presented in [10], and counteracted the warping effect by adding offsets to the receive beam directions. The technique was shown to strongly reduce MLA artifacts in unaberrated phantom recordings. However, when using the same correction values in aberrated phantom recordings, the image artifacts remained. The presence of aberration distorted the beam profiles and invalidated the pre-programmed correction offsets. Since inhomogeneities causing aberrations are unknown, valid correction offsets are difficult to estimate. Similarly, this will also be a weakness in the beam interpolation methods presented in [8] and [9]. To some degree, the sinc apodization method presented in [7] will also be affected by aberration, since it relies on a certain transmit beam shape. STB, on the other hand, is a blind correction technique, requiring nothing more than a certain acquisition pattern. Given a thin aberrator close to the transducer surface, adequate beam density and ideal interpolation, STB should theoretically perform identically to single line acquisition.

In this work we investigate how well the STB technique performs in a realistic, aberrating environment using four parallel beams and linear STB interpolation. The performance is evaluated using several quantitative and qualitative measures.

Section II contains the theory behind STB and the methods used for analysis. Section III presents the simulation and measurement setup. Section IV contains the results. These results are discussed in Section V, with conclusions presented in Section VI.

## 4.2  Theory

The number of parallel beams will be indicated by the number in front of the MLA and STB abbreviations. For instance, 4MLA indicates four parallel beams and 4STB

indicates four output STB beams. The group of receive beams belonging to one transmit event will be termed parallel receive group or MLA group. Normal acquisition with one receive beam per transmit beam will be termed single line acquisition, SLA.

### 4.2.1 Two-way response and the point spread function

In this work, we define the two way response according to the pulse-echo formulation in [12]:

$$v_0 = e_T \star_t g_T \star_t h_t \star_t h_r \star_t g_R, \tag{4.1}$$

where $\star_t$ is a temporal convolution operator, $e_T$ is the excitation pulse, $g_T$ and $g_R$ are the transducer impulse responses on transmit and receive, $h_t$ is the spatial impulse response on transmit and $h_r$ is the spatial impulse response on receive.

The point spread function is defined as the image obtained from imaging a single point scatterer. For SLA imaging, the PSF will be identical to the two-way response, assuming that the two-way response is constant for all imaging beams. However, using parallel beamforming, the two-way response becomes variant from beam to beam. Hence the PSF will be the image obtained from sampling a point scatterer in a grid of beams with different two-way responses.

### 4.2.2 The Synthetic Transmit Beam method

As explained in the introduction, the source of MLA artifacts is the misalignment of the transmit and receive beams. The basic idea of STB is therefore to create a synthetic transmit beam for each receive beam direction. This is done through interpolation on channel data between neighboring transmit events. Since a single element is small compared to the wavelength, it can be considered omni directional. The resolution of an image obtained from receiving on a single element will then be determined almost solely by the transmit beam width. Hence, the lateral spatial bandwidth of image from a single element is determined by the transmit aperture. So as long as the transmit beam spacing satisfies the Nyquist sampling theorem for this bandwidth, data from any intervening transmit beam can be reconstructed using interpolation. Given adequate transmit beam density and ideal interpolation, each receive beam can then be perfectly aligned with a synthetic or real transmit beam as if traditional SLA had been used [5, 11].

### 4.2.3 STB and aberrations

Aberrations occurring close to the transducer surface can be modeled as simple alternations of the aperture function (phase and amplitude). This will result in higher side lobes and other distortions to the transmitted ultrasound pulse. It will however not change the lateral spatial bandwidth of the pulse. Hence, the requirements of the STB method to reconstruct intervening transmit beams is not violated. While the artifacts of regular MLA is amplified by aberrations [4], one can therefore assume that STB will perform just as well both with and without aberrations.

### 4.2.4 STB practical implementation

STB as described in the previous section requires coherent interpolation on channel data. This is computationally intense. In [5] and [11], it is shown that the STB interpolation also can be done after beamforming. This greatly reduces the computational complexity of the method. The easiest implementation comes from using linear interpolation. An equivalent implementation can then be achieved by receiving two times in each direction, but from different transmits events as illustrated in Fig. 4.1.
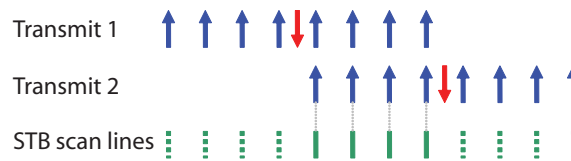


Figure 4.1: 4STB acquisition pattern. Figure shows transmit and receive directions for two neighboring transmit events. Receive directions are indicated with up arrows and transmit direction with down arrows. Resulting STB scan line positions are indicated with solid lines.

Each STB scan line is then created using a weighted summation of the two scan lines in the same direction. Using linear interpolation, the weighting of the scan lines before summation is given by the distance from their transmit direction. For the case of 4STB, the eight scan lines of each parallel receive group will be weighted with the coefficients $0.1250, 0.3750, 0.6250, 0.8750, 0.8750, 0.6250, 0.3750$ and $0.1250$ before summation of data from the same directions.

The downside of doing the STB interpolation after beamforming is that one will need eight parallel beams to achieve four output STB scan lines (See Fig. 4.1).

### 4.2.5 Higher order STB interpolation

The STB technique is not limited to linear interpolation. Any interpolation can in principle be used to create the synthetic transmit beams.

If STB is implemented using coherent interpolation on channel data, the synthetic transmit beams can for example be reconstructed from spline interpolation over four neighboring transmit events.

Equivalent higher order STB interpolation can also be implemented after beamforming, but requires more parallel beams. Using four point spline interpolation, one would have to receive four times in each directions from four neighboring transmit event.

The problem of doing higher order STB interpolation is that it increases the vulnerability to motion artifacts. This due to coherent summation of data from a larger time span.

### 4.2.6 Metrics to measure parallel beamforming artifact

Much of the literature on parallel beamforming compensation methods is to be found in patents. Due to this, there are few established methods on how to evaluate and quantify the artifacts.

First of all, the B-mode artifacts are mostly a visual disturbance. It does not decrease contrast resolution or spatial resolution and the human eye can in most cases easily determine that the artifacts are not physical features of the imaged object. But they remove attention from the actual imaged object, and any ultrasound clinician would like them removed.

The artifacts appear as a stationary blocky pattern in the image. What this actually shows, is that the imaging system is spatially shift variant. Ideally, the image of an object should be the same regardless of its position relative to the probe. But for a shift variant imaging system, the object image will change with object position.

For an imaging system to be shift invariant there are some factors that must be in place:

1. The two-way response of each imaging beam must be equal in shape.

2. The two-way response of each imaging beam must be equally spaced.

3. The distance between each imaging beam must satisfy the Nyquist sampling theorem.

The problem of parallel beamforming lies mainly in item 1 and 2. Skewing and warping results in varying shape and spacing of the two way responses. Item 3 assumes ideal lateral interpolation to avoid aliasing errors after detection. If not, the imaging system will still be spatially shift variant, even if 1 and 2 is satisfied. Since ideal interpolation can not be achieved in practical situations, the beam density should be somewhat higher than the Nyquist sampling limit to reduce aliasing errors. Typically some degree of under sampling and aliasing errors are tolerated when high frame rate is a priority.

Using simulations and measurements, the metrics used in this work tries to investigate and measure to what extend the three above listed requirements are satisfied using parallel beamforming with and without synthetic transmit beams.

**Lateral Shift Variance (LSV) plots**

LSV (Lateral Shift Variance) plots, such as those in Fig. 4.7 can be used to investigate the spatial invariance of an imaging system [4, 5]. They are created by simulating images of a point scatterer moving through the imaging sector. Each image will then correspond to the PSF of the system at the point scatterer location. For a shift invariant system, the resulting PSFs should be constant in shape. Since visualizing the whole 2D PSF in different positions is not suitable in printed form, the LSV plots show the axial mean square values of the PSFs instead. Each row in the LSV image
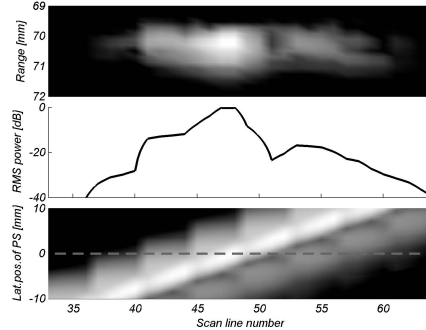
Figure 4.2: Illustration of how LSV plots are generated. Top: Image of a point scatterer at a lateral position at focus depth. Middle: Radial mean square value of the point scatterer image. Bottom: Stacked radial mean square values for several point scatterer positions. The dashed line indicates the position of the radial mean square value in the middle pane. Top and bottom images are shown with a dynamic range of 40 dB.

corresponds to a PSF at the position indicated by the y-axis. This provides a plot where it is easy to evaluate the spatial variance of the system. If the system is shift invariant, the LSV plot should show a straight diagonal structure. Deviations from a straight diagonal structure, such as in Fig. 4.2, indicate that the PSF varies with lateral position and that the system is shift variant. LSV plots also visualize the resulting MLA artifacts through the whole dynamic range of the B-mode image.

**Correlation Analysis**

Assuming Rayleigh scattering conditions, the authors in [13] show that the autocorrelation for a complex amplitude process equals the scaled autocorrelation of the two way response. This allow us to predict the correlation between scan lines from their corresponding two-way responses. In vivo, with aberrations, the two-way responses are unknown, but from the same relation we can get information about the two-way responses by estimating the scan line correlation from recordings.

In normal single line acquisition, the two-way responses are equally spaced and constant from beam to beam, resulting in a consistent cross correlation between neighboring scan lines. Due to warping and skewing, parallel beamforming two way responses are variant from beam to beam. This results in a variation in beam to beam correlation.

The work presented in [4] used variation in beam to beam correlation as a quantitative measure of the amount of MLA artifacts in recorded B-mode images. Pairs of neighboring beams across MLA groups were showed to have consistently lower correlation than pairs within MLA groups. This is caused by the transmit beams which pull the two way responses in opposite directions at these location. The location of

the correlation drops corresponded to the lateral discontinuities in the images and the magnitude of the drops seemed to correspond to the visibility of the artifacts in the images. When estimating the cross correlation from measurements there will always be a variance in the estimates. This could obscure the drop in correlation between MLA-groups. The cross correlation estimator that would differentiate best is in [4] showed to be as follows:

$$C_c = \frac{2Real(\hat{R}_{ij})}{\hat{R}_{ii} + \hat{R}_{jj}}, \tag{4.2}$$

where the $\hat{R}_{ij}$ estimate is calculated as correlation between IQ data in scan lines $i$ and $j$ averaged over a depth range. $C_c$ values for all neighboring scan lines can be plotted to visualize the correlation variation across the image. An overall percentage correlation variation can be calculated as follows [4]:

$$C_d = \frac{\frac{1}{N}\sum_{ij \in W} C_c - \frac{1}{M}\sum_{ij \in T} C_c}{\frac{1}{N}\sum_{ij \in W} C_c} \cdot 100, \tag{4.3}$$

where $ij$ is a pair of adjacent scan lines. The set $W$ contains all such pairs within MLA groups, and the set $T$ contains all such pairs located at transitions between MLA groups. $N$ is the size of the set $W$, and $M$ is the size of the set $T$. A good $C_d$ value should be as close as possible to zero since this indicates an even beam to beam correlation throughout the image. Using regular MLA, the value will in general be positive since the correlation within the MLA groups is larger than at the transitions between MLA groups.

If the two-way responses are known, the $C_c$ values can be calculated by inserting the cross correlation of the two-way responses for $\hat{R}_{ij}$ in Eq. 4.2.

### Speckle Tracking

Speckle tracking is a technique for evaluating cardiac tissue deformation. The reflected ultrasound from a tissue region creates a distinct interference pattern, called speckle, which can be followed from frame to frame to determine local tissue movement. 2D speckle tracking can only track points inside the imaging plane. Object movement out of the imaging plane will result in decorrelation and degraded tracking performance. Due to high tissue velocities and object movement in and out of the imaging plane, a high frame rate is desirable when performing 2D cardiac speckle tracking [1, 14]. This can be achieved by using parallel beamforming. However, uncompensated parallel beamforming results in a shift variant imaging system [4, 5]. Shift variance will cause the speckle pattern to change with object position, and is therefore likely to influence the speckle tracking accuracy. This makes speckle tracking suitable as a metric for comparing SLA, MLA and STB.

According to theory, ideal STB should perform just as well with speckle tracking as SLA. Since aberration not should impact STB shift variance, one can also predict

that STB should perform as well as SLA also with aberrations. However, due to linear STB interpolation it can be assumed that the practical STB implementation will have a somewhat lower performance.

## 4.3   Setup

All recordings were made using a M3S probe and a modified GE Vingmed System 7 scanner capable of recording IQ data. The acquisition parameters were set as specified in Table 4.1. These parameters were chosen to be identical to the ones used in a previous work [4] to enable comparison of results between the two publications. Measurements and simulations of SLA, 4MLA and 4STB were performed using these parameters.

The Nyquist sampling criterion, NSC, states the maximum allowed beam spacing while avoiding aliasing. The one way transmit NSC in radians is given by: $\delta\theta_t = \lambda/a_t$, where $a_t$ is the transmit aperture size. The two way NSC is given by: : $\delta\theta_{tr} = \lambda/(a_t + a_r)$, where $a_r$ is the receive aperture. Compared to the NSC, the parameters in Table 4.1 result in an over-sampled image. The transmit beam spacing is 69% of NSC and the two-way spacing 66% of NSC.

The STB technique was implemented using linear interpolation after beamforming. The only exceptions were two of the LSV simulations, where the STB technique was implemented using four point spline interpolation prior to beamforming. This was done to illustrate the improvement from using higher order STB interpolation.
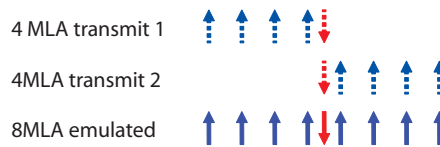


Figure 4.3: Emulation of 8MLA by combining two 4MLA transmits. Down arrows indicate transmit directions and up arrows indicate receive directions. The source beams are plotted in dotted style and the resulting emulated beams in solid style.

4STB requires 8MLA acquisition. Since the hardware was limited to four parallel beams, 8MLA was emulated as shown in Fig. 4.3. The 4MLA recordings and simulations were without any warping or skewing compensation.

The IQ data recordings were converted to B-mode images through lateral IQ interpolation, detection, time gain compensation, log compression and scan conversion. The IQ interpolation was performed to reduce aliasing errors from the detection step. It was implemented using linear interpolation at locations 0.25 and 0.75 between the original scan lines. In addition, MLA and STB recordings were compensated for lateral gain variations. The gain compensation values were estimated from IQ data and applied before further processing. The procedure is explained in more detail in [4].

Both *in vitro* phantom recordings and *in vivo* cardiac recordings were performed. The phantom was a CIRS Model 40, General Purpose Multi-Tissue Ultrasound Phantom with an attenuation of 0.5 dB/cm/Mhz. Recordings were performed both with fixed probe (images) and moving probe (movies). The cardiac recordings were of the left ventricle (LV) of a healthy male volunteer.

Simulations of beam profiles, lateral shift variance (LSV) and speckle tracking were performed using Matlab (The Mathworks, Inc.) and Field II [15]. Models of both the imaging system and the aberrator were implemented.

All *in vitro* recordings were performed both with and without an aberrating silicon patch in front of the transducer. The patch had a height profile (see Fig. 4.4) with a correlation length of 2.47 mm and a RMS time delay of 48.5 ns as described in [16]. This correlation length is in the range of typical thoracic body walls while the RMS time delay value corresponds to a worst-case value for thoracic body walls [17]. In the simulations, this aberrator was implemented as a pure time delay screen at the surface of the transducer. This was considered a good approximation since the patch was thin (0.69mm).

The simulated $C_d$ values were calculated at focus depth from the two-way responses of five beams located around zero degree steering angle.

To evaluate the speckle tracking performance using parallel beamforming, a sum of absolute difference, SAD, algorithm was applied to track the movement between two frames. A point with a surrounding kernel was defined in the first frame. The center of the kernel sized area in the next frame that minimized the sum of absolute difference compared to the kernel in the first frame was chosen as the new position of the point. The speckle tracking was performed on beam space data and interpolation was used to achieve sub pixel tracking resolution. First the number of beams was doubled using linear IQ-interpolation, and then the detected image data was interpolated 20 times. 480 points was tracked in four independent simulated 20 x 10 mm uniform speckle areas. The phantom was positioned at focus depth and was tilted a single distance corresponding to two receive beam widths. The speckle tracking kernel size was 4 beam widths laterally and 3.1 mm in range. The search region was set to +/- 3 beam widths laterally.
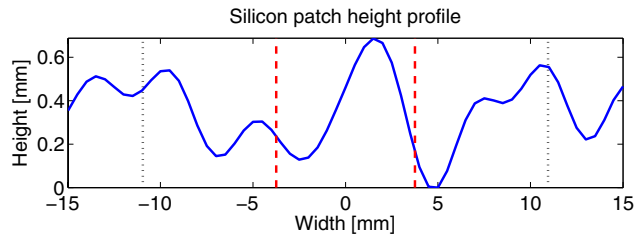


Figure 4.4: The height profile of the silicon patch used for aberration. The dotted line indicates the start and end of the receive aperture and the dashed line indicates the start and end of the transmit aperture.

Table 4.1: Scan setup

| | |
|---|---|
| Transmit frequency | 2.5 MHz |
| Receive frequency | 2.5 MHz |
| # Transmit beams | 96, 24, 24 (SLA, 4MLA, 4STB) |
| # MLA beams pr tx beam | 1, 4 and 8 (SLA, 4MLA, 4STB) |
| PRF | 4000 Hz |
| Sector width | 75 deg |
| Transmit aperture width | 7.5 mm |
| Receive aperture width | Expanding (max: 2.19 cm) |
| Transmit apodization | Rectangular |
| Receive apodization | Hamming |
| Transmit focus | 70 mm |
| Receive focus | Dynamic |

## 4.4 Results

Throughout the results, six different cases have been compared: SLA, 4MLA and 4STB both with and without aberration. These cases have been evaluated using several performance measures. Simulated beam profiles show the basic impact of MLA, STB and aberration on an acoustic level. The lateral shift variance (LSV) plots link the shapes and constellations of the beam profiles to the lateral shift variance of the system. *In vitro* phantom images show how the various acquisition methods perform when imaging several scatterers in a controlled environment. Finally, the *In vivo* recordings show the performance in a realistic scenario with naturally occurring aberration. In the latter two cases, the beam to beam correlation method presented in previous work [4] was used to quantify the amount of block artifacts in the B-mode images. Speckle tracking simulations further show how parallel beamforming and aberration influence the tracking accuracy, and the improvements gained from using the STB technique. Simulations of higher order STB interpolation show how the STB technique can approach its theoretical performance.

The reader should be aware that the MLA artifacts present in some of the B-mode images will be more visible when viewed on a screen than in the printed version. The available movies provide an even better impression of the artifacts. These will be referred to with file names and can be found at *www.ntnu.no/us/ThesisMM/bjastad*.

### 4.4.1 Simulations

The simulated one-way beam profiles are shown in Fig. 4.5. Both transmit and receive beam steering directions were set to zero degrees. Profiles without aberration are shown to the left and profiles with aberration to the right. One effect of the aberration was that the side lobe level of the Hamming apodized receive beams rose to the same level as the transmit beam's side lobes. Another effect was that the maximum for the transmit and receive directions was offset with 2.0 and 0.2 degrees respectively compared to the intentional steering direction. This steering was caused
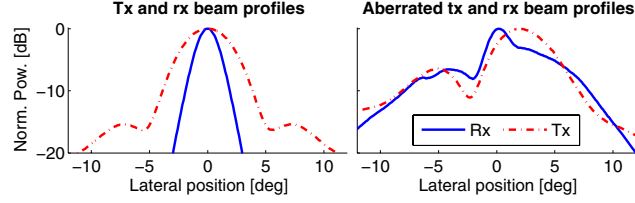
Figure 4.5: Transmit and receive one-way beam profiles. Left side: Without aberration. Right side: With aberration.

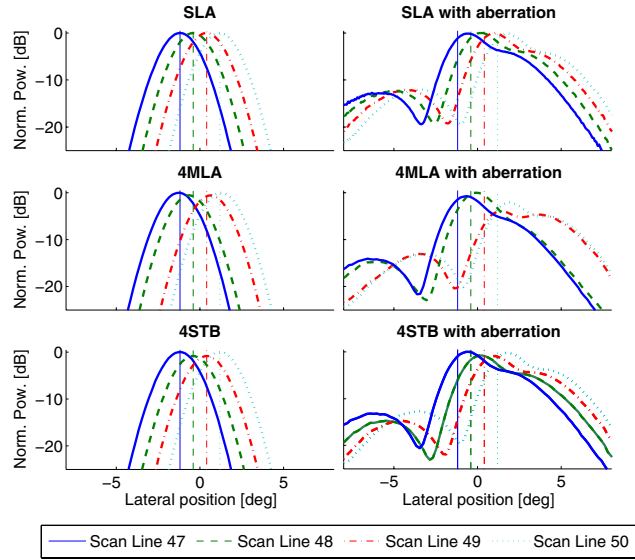by the smaller transmit aperture seeing a different aberrator than the larger receive aperture (See Fig. 4.4).



Figure 4.6: Two-way beam profiles of scan line 47, 48, 49 and 50 in the proposed scan setup of Table 4.1. The figure illustrates the variation in the shape and spacing of the two way beam profiles using the various acquisition methods with and without aberration. Scan line 47 and 48 belong to MLA group 12 and scan line 49 and 50 belong to MLA group 13. Notice that from the displayed beams, the variation in shape and spacing is largest between scan line 48 and 49, since they belong to different transmit beams. Left side: Without aberration. Right side: With aberration. Top: SLA. Middle: 4MLA. Bottom: 4STB. Vertical lines indicate the receive beam direction of the two-way beam profiles in corresponding line style.

The corresponding two-way beam profiles are shown in Fig. 4.6 for SLA, 4MLA and 4STB. Each plot shows four neighboring two-way beam profiles normalized to the maximum value of the four. In the 4MLA and 4STB cases, the two leftmost beam profiles in each plot belong to MLA group 12 and the two rightmost belong to MLA group 13. This selection was made to emphasize the transition between the MLA groups, as this is typically where the difference in beam profile shape and position is largest and the lateral discontinuities in the B-mode images appear. The vertical lines indicate the steering direction of each scan line. Ideally these vertical lines should intersect their corresponding beam profiles at their maximum.
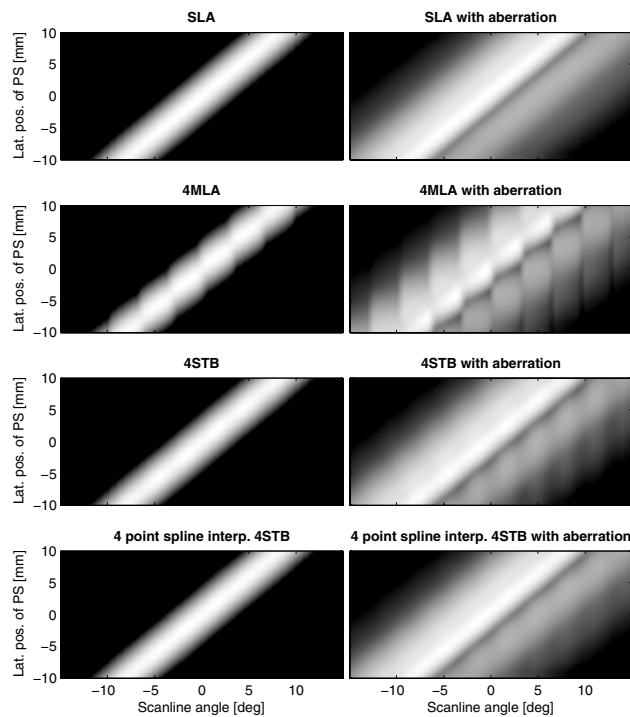


Figure 4.7: Lateral shift variance plots. Left side: Without aberration. Right side: With aberration. Top row: SLA. Second row: 4MLA. Third row: 4STB. Bottom row: 4STB using 4 point spline interpolation. All plots are displayed with a dynamic range of 40dB.

Fig. 4.7 shows the LSV plots. The three first figure rows show the LSV plots for the same cases as for the two-way beam profiles. The bottom figure row shows the LSV plot from using higher order interpolation to create the synthetic transmit beams.

Fig. 4.8 shows the error distribution from using speckle tracking on B-mode images acquired using SLA, 4MLA and 4STB. The tracking error was measured in percentage of the actual translation distance. Numerical results are summarized in Table 4.2.
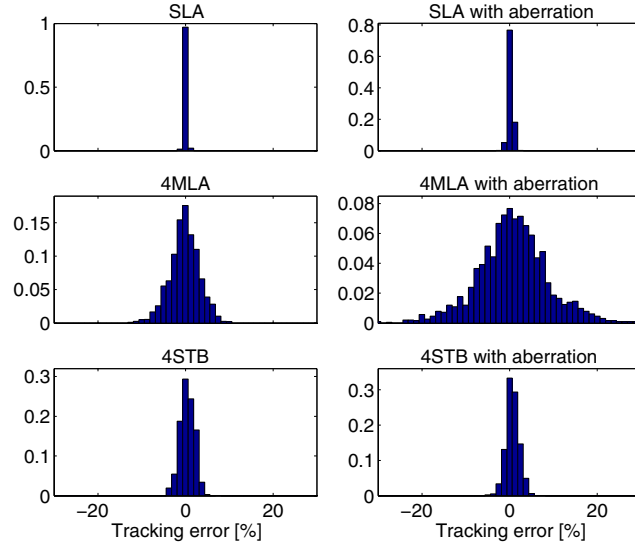
Figure 4.8: Speckle tracking error distributions using SLA, 4MLA and 4STB with and without aberration. The error is measured in percent of the total translation distance of two beam widths. The standard deviations of the distributions are tabulated in Table 4.2

.

Table 4.2: Speckle tracking error statistics

|  | Standard deviation [%] without aberration | Standard deviation [%] with aberration |
|---|---|---|
| SLA | 0.2 | 0.6 |
| 4MLA | 3.4 | 8.0 |
| 4STB | 1.7 | 1.5 |

## 4.4.2 Measurements

The *in vitro* phantom recordings are shown in Fig. 4.9 with their corresponding $C_c$-plots in Fig. 4.10. Both the B-mode images and the $C_c$-plots have been cropped to reduce print size. In both figures, the unaberrated cases are shown to the left and the aberrated cases to the right. The top row shows SLA, the middle row shows 4MLA and the bottom row shows 4STB. The block artifacts are fairly visible for the aberrated 4MLA image, but can also be seen in some parts of the unaberrated 4MLA image. Both the SLA images and 4STB images are apparently without any artifacts. Notice that this is in accordance with the observations in the $C_c$-plots in Fig. 4.10, where the 4MLA cases show a periodical pattern of three high values followed by a lower value. The periodicity of this pattern corresponds to the MLA groups, where the low $C_c$ values originate from transitions between MLA groups. The difference between the
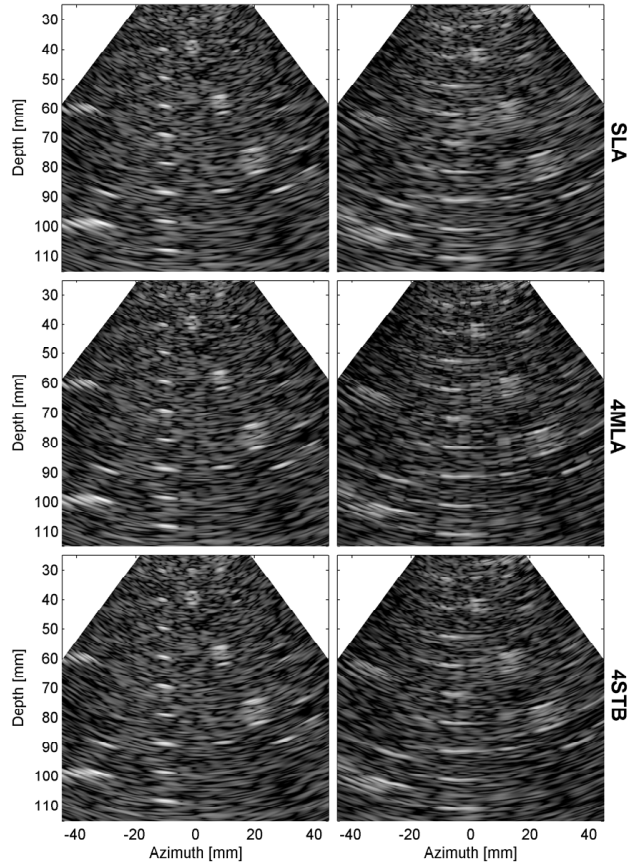
106

Figure 4.9: B-mode images from the CIRS40 phantom recordings. Figures on the left side are without aberration and figures on the right side are with aberration. Top left: SLA (*Ch4_Movie01.gif*). Top right: aberrated SLA (*Ch4_Movie02.gif*). Middle left: 4MLA (*Ch4_Movie03.gif*). Middle right: aberrated 4MLA (*Ch4_Movie04.gif*). Bottom left: 4STB (*Ch4_Movie05.gif*). Bottom right: aberrated 4STB (*Ch4_Movie06.gif*). All images are displayed with a dynamic range of 35 dB.

high and low values is largest for the aberrated 4MLA case. For the SLA and 4STB cases, no periodical pattern can be observed.

Fig. 4.11 shows the B-mode images and $C_c$-plots from the cardiac *in vivo* recordings. Regular 4MLA with the corresponding $C_c$-plot is shown to the left, and STB to the right. Notice the difference in both block artifacts and $C_c$ values.

Table 4.3 shows the $C_d$ values for the various recordings. This parameter gives a single value quantification of the MLA artifacts in the recordings. $C_d$ values calculated from recordings are displayed in the fourth column. $C_d$ values predicted from simulated
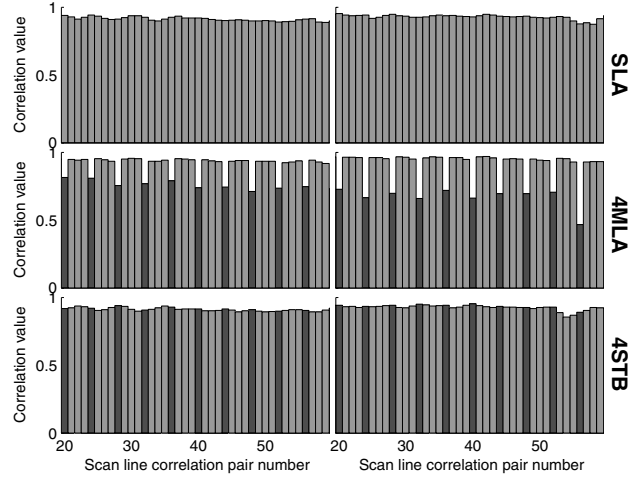
Figure 4.10: $C_c$ plots from the CIRS40 phantom recordings. Plots correspond to the B-mode images in Fig. 4.9. Plots on the left side are without aberration and plots on the right side are with aberration. Top: SLA. Middle: 4MLA. Bottom: 4STB.

Table 4.3: Indicator showing differences in correlation, $C_d$

| Acquisition | Object | Aberration | Meas $C_d$ | Sim $C_d$ |
|---|---|---|---|---|
| 4MLA | Phantom | None | 18.7 | 19.8 |
| 4MLA | Phantom | Silicon | 30.0 | 33.5 |
| 4STB | Phantom | None | -0.4 | -1.4 |
| 4STB | Phantom | Silicon | -1.1 | -1.2 |
| 4MLA | Heart | *in vivo* | 25.9 | *NA* |
| 4STB | Heart | *in vivo* | 2.3 | *NA* |

two way responses are shown in the last column. Measured and simulated $C_d$ values showed good correspondence. Notice the high values for 4MLA, the increase in the 4MLA $C_d$ value from unaberrated to aberrated and the low values for 4STB.

## 4.5 Discussion

### 4.5.1 General discussion

Fig. 4.6 shows the simulated two-way beam profiles from the different cases. The top row shows the beam profiles from using SLA. This case was included as a reference and gold standard. Without aberration, the beam profiles were evenly spaced and equal in shape. This resulted in a straight diagonal structure in the LSV plot shown in Fig. 4.7, indicating that this imaging system is shift invariant. As can be seen from the top left image in Fig. 4.9, the B-mode image obtained using this acquisition method
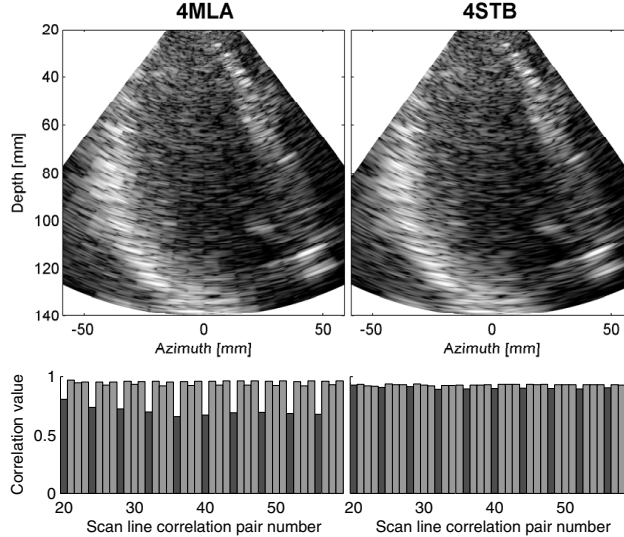
Figure 4.11: B-mode images and $C_c$ plots from human left ventricle recordings. B-mode images are displayed in the top pane with corresponding $C_c$ plots below. Regular 4MLA is shown to the left (*Ch4_Movie07.gif*), and 4STB to the right (*Ch4_Movie08.gif*).

contained no artifacts. This was also confirmed by the $C_c$-plot shown in the top left pane of Fig. 4.10. The $C_c$ values were approximately constant.

Adding aberration (Fig. 4.6, top right), the SLA beam profiles were distorted, the side lobe level increased, and the profile maximums shifted a bit to the right compared to the intentional receive directions. However, it is important to note that the beam profiles' shapes and spacing remained equal from beam to beam. So although the resolution and contrast were heavily reduced, the imaging system remained shift invariant (Fig. 4.7, top right), the B-mode remained free of block artifacts (Fig. 4.9, top right) and the $C_c$ values remained constant (Fig. 4.10, top right).

The second row of Fig. 4.6 shows the 4MLA cases. For the unaberrated case, the beam profiles were no longer equally spaced. Due to the warping effect, the first two beam profiles were pulled towards the transmit direction of MLA group 12 and the last two beam profiles were pulled towards the transmit direction of MLA group 13. This left a gap between the two MLA groups and resulted in a shift variant system since the data was incorrectly displayed as if the beam profiles were equally spaced. The B-mode image of the point scatterer changed depending on the lateral position of the point scatterer. This can be seen from the distorted structure shown to the left in the second figure row of Fig. 4.7. The pattern from the LSV plot can also be found in the B-mode image shown in Fig. 4.9. The pattern is not as visible here as in the LSV plot. This is due to the relatively uniform backscatter intensity of the imaged phantom. MLA artifacts are more visible when imaging objects with a high dynamic

109

range in the backscattering [4]. The gap between the beam profiles also caused a drop in beam to beam correlation. This can be seen from the $C_c$-plots in Fig. 4.10 (middle left), where every fourth value drops significantly. This systematic drop in correlation can also be seen from the measured $C_d$ value of 18.7 (Table 4.3).

When combining aberration with 4MLA, the distortions in the two-way beam profiles increased (Fig. 4.6, middle right). Not only did the gap between the MLA groups increase, the individual shape of all beam profiles within a MLA group became different. The difference in shape was largest at the borders between MLA groups, such as between scan lines 48 and 49 in the middle right plot in Fig. 4.6. The beam profile shape was found to be slowly changing from beam to beam within a MLA group, followed by an abrupt change in shape at the first beam in the neighboring MLA group. As discussed in [4] this causes a stair-like gain variation pattern when imaging objects with a high dynamic range in the backscattering. Such patterns can clearly be seen in the right pane of the second figure row in Fig. 4.7 and also in the bottom left corner of the cardiac 4MLA B-mode image in Fig. 4.11. The middle right pane of Fig. 4.9 shows the B-mode image from the aberrated 4MLA phantom recording. Compared to the unaberrated 4MLA B-mode phantom image, the block artifacts in this image are much stronger. This increase in image artifacts was also reflected in the $C_c$ plots (Fig. 4.10, middle right) and the 60% increase in measured $C_d$ value from 18.7 to 30.

The bottom left plot of Fig. 4.6 shows the two-way beam profiles when using 4STB without aberration. Compared to 4MLA, the beam profiles were clearly more regularly spaced, with the beam profile maximum in the desired direction for all the beams. This resulted in a much improved LSV plot (Fig. 4.7, second figure row to the left) that was hardly distinguishable from the one from the SLA acquisition (Fig. 4.7, top left). The 4STB B-mode image shown in Fig. 4.9 was also comparable to the SLA version, with no visible block artifacts. This was confirmed by the corresponding $C_c$-plot (Fig.4.10, bottom left), which showed no periodic correlation drops and a very low measured $C_d$ value of -0.4. The negative $C_d$ indicates that the beam to beam correlation is slightly higher at the transitions between MLA groups (see equation 4.3) than within.

When inserting the silicon aberrator in front of the probe, the 4STB beam profiles became more distorted (Fig. 4.6, bottom right). However, the spacing between the aberrated 4STB beam profiles was much more even than in the aberrated 4MLA case. Also, the shape of the aberrated 4STB beam profiles was more constant than in the aberrated 4MLA case. The beam profiles were not completely comparable to those in the aberrated SLA case, but aberrated 4STB showed a significant improvement compared to aberrated 4MLA. This could also be concluded from the LSV plot shown to the right in the third figure row of Fig. 4.7. The stair-like gain pattern observed in the aberrated 4MLA case was hardly visible in this plot. However, some spatial variance could be seen in the right side of the plot. These variations correspond with the uneven side lobes situated around -5 degrees in the bottom right beam profile plot of Fig. 4.6. Seemingly, the STB technique was not able to straighten the beam profiles equally good there as in the main lobe. Although the LSV-plot had some remaining discontinuities, no block artifacts could be seen in the phantom B-mode image (Fig.

4.9, bottom right). This 4STB B-mode image showed similar image quality to the SLA recording. The corresponding $C_c$-plot shown in Fig. 4.10 showed no periodic drops in correlation and the measured $C_d$ value was as low as -1.1.

The cardiac 4STB B-mode image and $C_c$ plot is shown to the right in Fig. 4.11. The improvement from using the STB technique compared to regular MLA could easily be seen both qualitatively in the B-mode images and quantitatively in the $C_c$ plots and $C_d$ value. By applying the STB technique, the measured $C_d$ value was reduced from 25.9 to 2.3.

### 4.5.2   Simulated and Measured $C_d$ values

Generally the measured and simulated $C_d$ values showed good correspondence. This demonstrates the accuracy of the simulations, and that the measured $C_d$ value provides indirect information about the warping and skewing of the imaging system beam profiles.

Although the correspondence was good, the simulated $C_d$ value of 4MLA both with and without aberration was slightly higher than the measured. The simulated $C_d$ value was calculated from two-way responses of five neighboring scan lines. The two-way responses were simulated at focus depth for steering angles around zero degrees. The $C_d$ value of the measurements is calculated from $C_c$ values throughout the imaging sector. The wider beams at the edges of the sector and in the near field results in a higher $C_c$ and then possibly a lower $C_d$ value.

### 4.5.3   Speckle Tracking

The results from the speckle tracking are displayed in Fig. 4.8 with tabulated standard deviations (SD) in Table 4.2. The top figure row shows the tracking error distribution using SLA. Both without and with aberration, the tracking was found to be very accurate for this case. Using four parallel beams the standard deviation of the tracking error increased noticeably from 0.2% to 3.4% without aberration and from 0.6% to 8.0% with aberration. Such increases in error correspond well with the observed increase in B-mode artifacts from SLA to 4MLA and from 4MLA without aberration to 4MLA with aberration. Using 4STB (Fig. 4.8 bottom figure row) the standard deviation of the tracking error was halved without aberration (from 3.5% to 1.7%) and reduced over five times with aberration (from 8.0% to 1.5%). The almost identical tracking results for 4STB both with and without aberration showed that the speckle tracking performance was not affected by aberration when using the STB technique.

### 4.5.4   Motion Artifacts

Since the STB technique is based on coherent interpolation between data from different transmit events, it will be vulnerable to motion artifacts when imaging moving objects such as the heart. Motion artifacts cannot easily be observed in Fig. 4.11. This is due to the short time delay between the data involved in the STB interpolation and the low velocity of the cardiac tissue compared to the pulse repetition frequency

(PRF) and receive frequency. Even when emulating 8MLA from two 4MLA transmits, the maximum delay between the scan lines in the same direction is 1/PRF (pulse repetition frequency). Using a PRF of 4000 Hz, a receive frequency of 2.5MHz and a sound velocity of 1540 m/s (see Table 4.1), the data from receive beams in the same direction will have opposite phase for tissue velocities of 61.6 cm/s (Nyquist limit). The maximum cardiac tissue velocity is around 17 cm/s for a short duration in the cardiac diastole [18]. This would result in a 50 degree phase difference, which again would result in a 0.85 dB reduction in power if the two signals were summed coherently. For most of the cardiac cycle the tissue velocities will be below 10 cm/s which result in a power reduction of only 0.21 dB.

Although no motion artifacts could be seen in the echoes from the cardiac tissue, some artifacts could be seen in echoes from the blood in the cavity. These are not easily seen in Fig. 4.11, and are best observed in the movie, *Ch4_Movie08.gif*. The motion artifacts appear due to the high velocity of the blood. The normal value of aortic peak blood velocity and trans-mitral flow are around 80 cm/s and 60 cm/s, respectively [19]. This is close to and above our Nyquist limit of 61.6, resulting in destructive interference between the signals involved in the coherent STB interpolation. The effect is however quite minute and will only be observed in patients with a good acoustic window where the echoes from the blood do not drown in reverberations.

### 4.5.5 Higher Order STB interpolation

Almost all experiments and simulations of the STB technique in this work have been done using linear interpolation. The exception is the last two figure rows of Fig. 4.7. The two figures in this row show the LSV-plot when using four point spline interpolation to create the synthetic transmit beams. This was done to investigate the potential improvement from using higher order interpolation.

Without aberration the performance seemed to be close to identical with the LSV plot from using linear STB interpolation. A larger improvement could be seen for the aberrated case shown in the bottom right plot of Fig. 4.7. Compared to the LSV plot using linear interpolation, the spatial variance observed in the lower right triangle of the LSV plot is reduced.

The benefit of higher order interpolation will depend on the transmit beam sampling density. For recordings with high transmit line density, the sinc squared frequency response of a linear STB interpolation will be sufficient to reconstruct the synthetic transmit beams. However, this would come at the cost of a lower frame rate. Using a transmit beam density close to the Nyquist sampling criterion maximizes the frame rate. In this case, the difference between linear interpolation and higher order interpolation with a more rectangular frequency response would probably be larger.

It is then likely to assume that these remaining artifacts seen in bottom right plot of Fig. 4.7 is related to STB interpolation order and transmit beam density, and that they could be further reduced from using an even higher order interpolation or increase the transmit beam density.

Although higher order interpolation produced better results in simulations, it might not be desirable in practice. Since it requires coherent interpolation between

data from three or more transmit events, the system would be more vulnerable to motion artifacts. Also, it would require three or more receive beams in each direction, something that increases the requirements to the hardware. The four point spline STB interpolation simulated in this work would require 16 parallel beams to produce four output STB beams (if the STB interpolation was done after beamforming).

### 4.5.6   Considerations on 3D Parallel Beamforming using STB

This study investigated the performance of a STB technique for 2D cardiac phased array imaging. If the method is used for 3D imaging, there are some challenges that one will have to consider. One challenge is motion artifacts. When scanning a volume instead of a plane, it is impossible to avoid large time delays between neighboring transmissions in one of the dimensions.  Another issue is the increased hardware requirements.  If applying the linear interpolation STB technique in both azimuth and elevation directions, the number beams in each receive direction would increase from two to four. Hence, a 16 parallel beams system would be required to generate 4 output parallel STB scan lines (two in each dimension).

## 4.6   Conclusion

In this work we compared the STB technique to regular parallel beamforming and single line acquisition using several qualitative and quantitative measures.  Using linear STB interpolation and four parallel receive beams in an aberrating environment, a frame rate of 167 Hz was achieved almost without any visually noticeable block artifacts in the B-mode images. The improvement from using STB was found to be largest with aberration. Both beam profile regularity, lateral shift invariance, beam to beam correlation consistency and speckle tracking errors improved noticeably in this case. Higher order STB interpolation was found to further improve lateral shift invariance, but might not be desirable due to motion artifacts.

## Acknowledgement

# References

[1] B. Lind, J. Nowak, J. Dorph, J. van der Linden, and L. A. Brodin, "Analysis of temporal requirements for myocardial tissue velocity imaging," *Eur J Echocardiogr*, vol. 3, pp. 214–9, Sep 2002.

[2] D. P. Shattuck, M. D. Weinshenker, S. W. Smith, and O. T. von Ramm, "Explososcan: A parallel processing technique for high speed ultrasound imaging with linear phased arrays," *J. Acoust, Soc. Amer.*, vol. 75, no. 4, pp. 1273–1282, 1984.

[3] O. T. von Ramm, S. W. Smith, and H. G. Pavy, "High-speed ultrasound volumetric imaging system – part ii: Parallel processing and image display," *IEEE transactions on ultrasonics, ferroelectrics, and frequency control*, vol. 38, March 1991.

[4] T. Bjåstad, S. A. Aase, and H. Torp, "The impact of aberration on high frame rate cardiac b-mode imaging," *IEEE transactions on ultrasonics, ferroelectrics, and frequency control*, vol. 54, January 2007.

[5] T. Hergum, T. Bjåstad, K. Kristoffersen, and H. Torp, "Parallel beamforming using synthetic transmit beams," *IEEE transactions on ultrasonics, ferroelectrics, and frequency control*, vol. 54, February 2007.

[6] J. J. Dahl, G. F. Pinton, M. L. Palmeri, V. Agrawal, K. R. Nightingale, and G. E. Trahey, "A parallel tracking method for acoustic radiation force impulse imaging," *IEEE transactions on ultrasonics, ferroelectrics, and frequency control*, vol. 54, February 2007.

[7] L. J. Augustine, "High resolution multiline ultrasonic beamformer." U.S. Patent 4.644.795, 1985.

[8] G. L. Holley and I. M. Guracar, "Ultrasound multi-beam distortion correction system and method." U.S. Patent 5.779.640, July 14 1998.

[9] D.-L. D. Liu, J. C. Lazenby, Z. Banjanin, and B. A. McDermot, "System and method for reduction of parallel beamforming artifacts." U.S. Patent 6.447.452, Sep. 10 2002.

[10] T. J. Hunt, B. M. Herrick, K. K. Robertson, and J. M. Ziel, "Ultrasonic imaging system using line splicing and parallel receive beam formation." U.S. patent 5.462.057, Oct. 31 1995.

[11] M. Bernard J. Savord, Andover, "Method and apparatus for increasing the frame rate and resolution of a phased array imaging system." U.S. patent 5.318.033, 1992.

[12] T. L. Szabo, *Diagnostic Ultrasound Imaging: Inside Out.* Elsevier Academic Press, 2004.

[13] R. F. Wagner, S. W. Smith, J. M. Sandrik, and H. Lopez, "Statistics of speckle in ultrasound b-scans," *IEEE transactions on ultrasonics, ferroelectrics, and frequency control*, 1983.

[14] J. D'hooge, *Myocardial Imaging: Tissue Doppler and Speckle Tracking*, ch. Principles and different techniques for speckle tracking, pp. 17–25. Blackwell Publishing, 2007.

[15] J. A. Jensen and N. B. Svendsen, "Calculation of pressure fields from arbitrarily shaped, apodized, and excited ultrasound transducers," *IEEE Trans. Ultrason.,Ferroelec., Freq. Contr.*, 1992.

[16] T. Johansen, B. Angelsen, and W. Nordhøy, "Phase aberrations - experiments and simulations," *Proceedings of the 23rd Scandinavian Symposium on Physical Acoustics*, 2000.

[17] L. M. Hinkelman, T. L. Szabo, and R. C. Waag, "Measurements of ultrasonic pulse distortion produced by human chest wall," *J. Acoust. Soc. Am.*, 1997.

[18] G. Sutherland, L. Hatle, P. Claus, L. Herbots, and J. Separovic, *Doppler Myocardial Imaging*, ch. Normal Data, pp. 49–102. BSWK, 2006.

[19] J. Rinaldi and B. Diebold, *Cardiac Ultrasound*, ch. Normal Intra Cardiac Doppler Flows, pp. 141–153. Churchill Livingstone, 1993.

# Chapter 5

# Single Pulse Tissue Doppler using Synthetic Transmit Beams

T. Bjåstad and H. Torp
Dept. Circulation and Medical Imaging, NTNU

Tissue Doppler Imaging (TDI) is a common technique for investigating myocardial function. Typically B-mode data and TDI data are recorded using separate acquisitions and combined into a single color overlaid image. In this work, we present a novel method for TDI imaging, where both TDI and B-mode are created from the same acquisition. Velocities are calculated from the phase shift between neighboring transmit events in the B-mode scan (hence the name Single Pulse Tissue Doppler, SPTD). Using a novel transmit beam interleaving pattern, this method provides TDI and B-mode at the same high frame rate with an adjustable Nyquist velocity limit.

Through simulations and measurements this work investigates the bias and variance of the SPTD velocities and compares the estimates to those of the conventional TDI autocorrelation estimation method.

The results showed that the method has a larger bias and variance in the velocity estimates than conventional TDI. However, by applying bias compensation, the accuracy of the SPTD velocity estimates was close to that of regular TDI. Using SPTD the whole left ventricle was imaged within a 65 degree sector at a frame rate of 110 frames per second.

## 5.1 Introduction

Tissue Doppler imaging was first introduced by McDicken et al in 1992 [1]. Since then, TDI has become a common imaging modality among cardiologists since it enables quantitative evaluation of cardiac tissue function. Due to rapid tissue deformation, high frame rate is a desired property in cardiac TDI. According to [2], frame rates above 100 Hz are required to accurately resolve all myocardial mechanical events

using tissueDoppler. However, the full frequency spectrum of cardiac motion contains components up to 100 Hertz [3, 4]. Detecting these components would require frame rates above 200 Hertz. Combined with high frame rate it is also desirable to have a wide sector. One specific example is when assessing asynchrony between cardiac walls [5, 6]. It is then advantageous to image the whole left ventricle in one field of view. High frame rate and large field of view are, however, conflicting properties. Increasing one of them will typically reduce the other. The factor determining the frame rate in cardiac TDI, is the number of transmit beams per image frame. Simply reducing the number of transmit beams will also reduce the imaging sector. If reducing the amount of transmit beams and at the same time maintaining a large field of view, the transmit beams will have to be wider. This is done by reducing the transmit aperture, something that reduces both penetration and lateral resolution. To avoid wider receive beams as well, multiple line acquisition (MLA) can be applied. Several narrow receive beams are then formed for each transmit event [7, 8]. However, using straightforward MLA the B-mode images will suffer from block like image artifacts [9]. In [10] it is shown that these block artifacts can be suppressed by creating synthetic transmit beams (STB) in each receive direction. The synthetic transmit beams were created by receiving in the same direction in neighboring transmit events.

Traditional TDI requires separate acquisitions for B-mode and Doppler images. One frame of B-mode is acquired for each Doppler frame. A possible approach to increase overall TDI frame rate is then to separately decrease the B-mode frame rate [11]. For example one B-mode frame for every second Doppler frame. This does, however, result in a lower B-mode temporal resolution and a temporal mismatch between the displayed B-mode image and the overlaid velocities.

In [12] a method for continuous acquisition high frame rate tissue Doppler is described. The velocities are then estimated from phase shifts between consecutive frames. This eliminates the need for a separate tissue Doppler acquisition, but, to avoid aliasing, the number of transmit beams have to be kept low. Hence, this method is most suitable for narrow sector imaging.

US patent 6589177 B1 [13] sketches a method for using the phase shift between neighboring transmit beams for both B-flow and B-mode. This technique may also be applied to tissue Doppler, but the patent does not address the problem of parallel beamforming artifacts in the B-mode. Neither does it provide any scheme for adjusting the Nyquist limit without reducing the frame rate, which is necessary for cardiac TDI.

In our single pulse tissue Doppler method (SPTD), we apply the STB technique (Synthetic Transmit Beam, [10, 14]) to achieve high frame rate B-mode with suppressed image artifacts. Using the STB implementation of [10], each scan line is created from two neighboring transmit events with identical receive direction. The idea of SPTD is to estimate the phase shift between these two receive beams in the same direction. In this way one can achieve both high frame rate B-mode and tissue Doppler from a single acquisition. We also suggest a novel transmit beam interleaving pattern to adjust the time delay between the overlapping receive beams. This allows adjustments of the Nyquist velocity limit without reducing the frame rate.

The paper is organized as follows. Section 5.2 contains theory on the SPTD method and the applied interleaving pattern. This chapter also contains a brief explanation on

118

the STB method used to remove parallel beamforming B-mode artifacts. Section 5.3 contains setup information on the various simulations and measurements performed in this work. Section 5.4 contains results on SPTD estimation bias and variance, as well as a description of the applied bias compensation. This section also contains *invivo* validation of the method including an imaging example of the full left ventricle. The results are discussed in section 5.5, followed by concluding remarks in section 5.6.

## 5.2 Theory

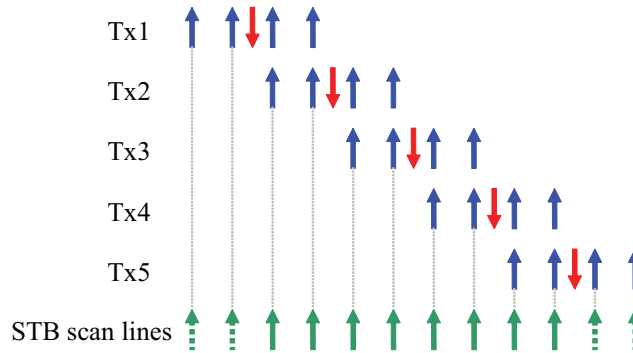### 5.2.1 Synthetic Transmit Beams



Figure 5.1: Illustration of 2STB scan sequence. Transmit directions are indicated with arrows pointing downwards, and receive directions with arrows pointing upwards.

B-mode recordings acquired using basic parallel beamforming contains block-like artifacts in the images [9]. The STB technique described in [10] and US Patent 5318033 [14] is a technique for removing these artifacts. The technique applies a special acquisition pattern with overlapping receive beams from neighboring transmit events (shown in Fig. 5.1). Each STB scan line is created through weighted summation of RF data from scan lines having identical receive directions but different transmit directions. This work implements a version of STB called incoherent STB (iSTB), where the weighted summation is done on detected data instead of RF data [15]. This was done to avoid motion artifacts arising from the large time delays between neighboring transmit beams. The scan lines of each MLA group are weighted with the coefficients 0.25 0.75 0.75 0.25 before summation of overlapping receive directions.

### 5.2.2 Single Pulse Tissue Doppler

In conventional tissue Doppler imaging, B-mode and tissue Doppler data are acquired sequentially using separate acquisition patterns. For example one frame of B-mode data followed by one frame of tissue Doppler data. The method that is presented in this paper, Single Pulse Tissue Doppler (SPTD), applies the STB acquisition pattern (Fig

5.1) and calculates both the B-mode image and tissue Doppler image from the same dataset. The autocorrelation approach is to calculate the velocities from phase shifts between RF data from several transmissions in the same direction. Instead of doing this, the proposed SPTD method calculates the velocities from pulses transmitted in neighboring directions but received in the same direction (See Fig. 5.1). Due to the warping and skewing effects of parallel beamforming [10], the resulting scan lines will not sample the exact same volume of the object, but their sampling volumes will have a large degree of overlap. The phase shift $\theta$ is estimated from the IQ data using the autocorrelation method:
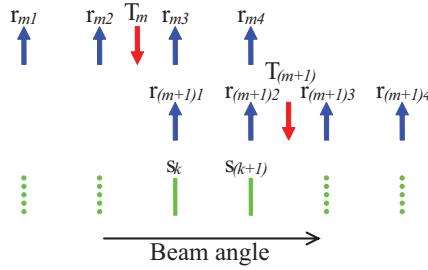


Figure 5.2: Illustration of the STB acquisition pattern. $T_m$ indicates transmit beam at spatial index $m$. $r_{mi}$ indicates receive beam with local MLA index $i$ from transmit beam $m$. $s_k$ indicates iSTB scan line number $k$.

$$R_k(1) = z_{m3}^* z_{(m+1)1}, \qquad k = 2m - 1, \tag{5.1}$$

$$R_k(1) = z_{m4}^* z_{(m+1)2}, \qquad k = 2m, \tag{5.2}$$

$$\theta_k = \angle R_k(1), \tag{5.3}$$

$$m \in < 1, 2, ..., M - 1 >$$

$R_k(1)$ is the autocorrelation of lag 1, $k$ is the scan line index, $z_{mi}$ is the IQ signal, $m$ is the transmit beam index, $i$ is the local parallel receive beam index, M is total number of transmit beams (see Fig 5.2).

The velocity, $v$, can further be calculated as:

$$v_{Nyquist} = \frac{c}{4f_0 \cdot PRT_p}, \tag{5.4}$$

$$v_k = \frac{\theta_k}{\pi} v_{Nyquist}, \tag{5.5}$$

where $PRT_p$ is the time delay between receive beams in the same direction (pulse repetition time), $c$ is the sound propagation velocity, and $f_0$ is the center frequency.

120

$v_{Nyquist}$ is the Nyquist velocity limit, which determines the maximum velocity that we can measure and corresponds to a phase shift of $\pi$. A longer observation time (increased $PRT_p$) results in a more accurate phase estimate. It is therefore desirable to use as high as possible $PRT_p$ while avoiding aliasing. Just increasing $PRT_p$ will also reduce the frame rate. To achieve maximum frame rate and at the same time a more flexible $PRT_p$ and $v_{Nyquist}$ one can use interleaving [16]. Instead of just waiting, the increased pulse repetition time is then utilized to acquire scan lines from other directions.
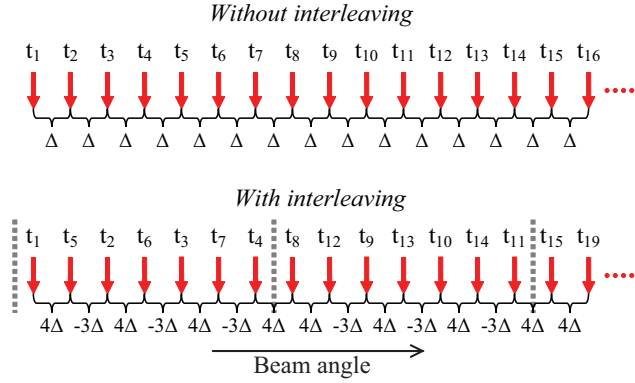


Figure 5.3: Illustration of a SPTD interleaved scan sequence. Transmit directions are indicated with arrows pointing downwards. $t_n$ indicates transmit at time index $n$. For simplicity, the receive beams of Fig. 5.2 has been left out. The text below the arrows indicate the delay between two neighboring transmit beams. This delay can be seen to alternate between $4\Delta$ and $-3\Delta$, where $\Delta$ is the time delay between each consecutive transmit. The vertical dashed lines indicate the periodicity of the acquisition pattern.

Fig. 5.3 shows a novel interleaving approach developed for the SPTD method. By skipping every second transmit beams $X$ times and then going back to transmit the skipped beams, the frame rate can be kept at a maximum while increasing the delay between neighboring transmit beams. This results in two different types of pulse repetition times. $PRT_p$ is the time between transmit events where the receive beams are in the same direction. $PRT_0$ is the time between consecutive transmit events regardless of direction. Fig. 5.3 shows the acquisition pattern for $X = 3$. The delays between neighboring transmit beams, $PRT_p$, can then be seen to alternate between $-3\Delta$ and $4\Delta$, where $\Delta$ equals $PRT_0$. To relate the phase shift calculated in Eq. 5.3 to $PRT_0$ instead of $-3PRT_0$ and $4PRT_0$, $R_k(1)$ is compensated as follows:

$$\tilde{R}_k = R_k e^{-j\theta_k \frac{X}{X+1}}, \quad k \in P, \tag{5.6}$$

$$\tilde{R}_k = R_k^* e^{j\theta_k \frac{X-1}{X}}, \quad k \in N, \tag{5.7}$$

where $P$ is all scan lines where the beam pair delay is positive, and $N$ is all scan

lines where the beam pair delay is negative. After this beam pair delay compensation, velocities can be calculated using Eq. 5.4 and 5.5 with $PRT_0$ instead of $PRT_p$.

From Fig 5.3, it can be seen that the acquisition pattern repeats after every seventh transmit beam (indicated by the vertical dashed lines in the figure). Periodic acquisition patterns for all delay combinations of $-X \cdot PRT_0$ and $(X+1) \cdot PRT_0$ can be constructed. Their period, $Ti$ is given by:

$$Ti = 2X + 1. \tag{5.8}$$

Using such interleaving patterns, the positive and negative delay beam pairs will have different Nyquist limit. Substituting $PRT_p$ in Eq. 5.4 with $(X+1) \cdot PRT_0$ and $X \cdot PRT_0$ gives:

$$v_{Nyquist_P} = \frac{c}{(X+1) \cdot PRT_0 \cdot 4f_0}, \tag{5.9}$$

$$v_{Nyquist_N} = \frac{c}{X \cdot PRT_0 \cdot 4f_0}. \tag{5.10}$$

where $v_{Nyquist_P}$ is the Nyquist limit for positive delay beam pairs and $v_{Nyquist_N}$ for negative delay beam pairs. Hence, the Nyquist limit of negative delay beam pairs will be $(X+1)/X$ times higher than for the positive delay beam pairs.

### 5.2.3 Inter scan line correlation

Assuming Rayleigh scattering conditions, the authors in [17] show that the autocorrelation for a complex amplitude process equals the scaled autocorrelation of the two-way response. Both conventional TDI and SPTD use autocorrelation to estimate phase shifts between consecutive transmit events. For conventional TDI, the two-way response of the consecutive transmit events are identical, since the transmit and receive direction are the same. Hence, the phase estimate for stationary targets will be consistently zero at all locations using conventional TDI. Using SPTD, the receive directions of consecutive transmit events are identical, but the transmit directions are different. The two-way responses will therefore not be completely correlated. This decorrelation will result in two things. Firstly the expected value of the phase estimate might not be zero for stationary targets. Secondly, the phase estimate will vary with position for stationary targets. In other words, the SPTD phase estimate will have a variance and might have a bias.

## 5.3 Setup

All recordings were made using a modified GE Vingmed System 7 scanner capable of recording IQ data and a M3S phased array probe. The main acquisition parameters are listed in Table 5.1. With the exception of the narrow sector recordings, the parameters specified in this table were used in all the recordings and simulations. Changes in acquisition parameters for the narrow sector recordings are listed in Table 5.2.

Table 5.1: Main scan setup

| | |
|---|---|
| Transmit frequency | 1.67 MHz |
| Receive frequency | 3.4 MHz |
| Transmit aperture width | 10 mm |
| Transmit focus | 112 mm |
| # Tx beams | 43 |
| # MLA beams pr Tx beam | 4 |
| PRF | 5000 Hz |
| Sector width | 65 deg |
| Receive beam spacing | 0.760 deg |
| Receive aperture | Expanding (max: 21.9 mm) |
| Receive focus | Dynamic |

Table 5.2: Narrow sector scan setup

| | |
|---|---|
| # Tx beams | 8 |
| # MLA beams pr tx beam | 4 |
| Sector width | 9 deg |
| Receive beam spacing | 0.581 deg |
| Transmit focus | 100mm |

The Nyquist sampling criterion, NSC, states the maximum allowed beam spacing while avoiding aliasing. The one way NSC in radians is given by: $\delta\theta = \lambda/a$, where $a$ is the aperture size. The two way NSC is given by: $\delta\theta_{tr} = \lambda/(a_t + a_r)$, where $a_t$ and $a_r$ are transmit and receive aperture sizes. The parameters in Table 5.1 result in a transmit beam spacing 60% of NSC, the receive beam spacing 65% of NSC and the two-way spacing 94% of NSC. The parameters in Table 5.2 result in a transmit beam spacing 50% of NSC, the receive beam spacing 51% of NSC and the two-way spacing 74% of NSC. Both setups are sufficiently sampled, but since no IQ-interpolation is performed, some aliasing artifacts could be expected after detection in the B-mode images. IQ interpolation could not be performed due to the large time delay between neighboring transmit beams.

The IQ data recordings were converted to B-mode images through detection, iSTB processing, time gain compensation, log compression and scan conversion. In addition the recordings were compensated for lateral gain variations. The gain compensation values were estimated from the recorded data. The procedure is explained in more detail in [9].

Both *in vitro* phantom recordings and *in vivo* cardiac recordings were performed. The phantom was a CIRS Model 40, General Purpose Multi-Tissue Ultrasound Phantom with an attenuation of 0.5 dB/cm/Mhz. The cardiac recordings were of the left ventricle (LV) of a healthy male volunteer.

Simulations were performed using Matlab (The Mathworks, Inc.) and Field II [18]. Since Field II cannot simulate second harmonic imaging, both transmit and receive frequency were set to 3.4MHz in the simulations. Some of the simulations included

the effect of phase aberrations (Fig. 5.7). The aberrations were implemented as a pure time delay screen at the surface of the transducer. The aberrator had a spatial correlation length of 2.47 mm and a RMS time delay of 21.1 ns. This is in the range of typical thoracic body walls [19]. The shape of the aberrator is described in [20].

When investigating the standard deviation of the SPTD phase estimates, the standard deviation was first measured from seven recordings with different beam densities. The normalized beam to beam correlation for each of these recordings was then calculated and used to perform comparative numerical simulations. The number of transmit beams in these recordings were 22, 29, 36, 43, 50, 57 and 64. The four first beam densities resulted in under-sampled images according to the Nyquist sampling criterion. The fourth beam density resulted in a marginally sampled image, and the last three resulted in over-sampled images.

The frame to frame tissue Doppler (F2FTD) recordings used to validate the SPTD velocities, were created by frame to frame Doppler processing on high frame rate recordings (similar to the method presented in [12]). The recordings were acquired using the SPTD acquisition pattern, allowing for direct comparison between the two methods. When displaying F2FTD velocities, the autocorrelation was first averaged 5mm in range and four receive beams laterally. The frame rate of 457 frames per second caused aliasing at 5.15 cm/s in the F2FTD recordings. For the velocity curves (Fig. 5.10), this was compensated for by using the *unwrap.m* function in Matlab. This unwrapping was not performed in the color M-mode recordings (Fig. 5.11) due to serious artifacts.
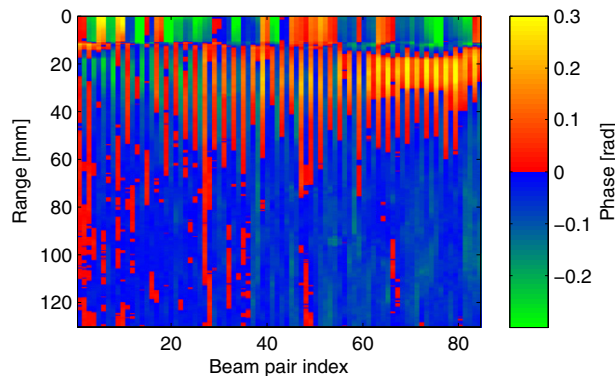
## 5.4 Results



Figure 5.4: The figure shows how the SPTD phase bias varies in azimuth and range. The bias was found from calculating $\theta$ of Eq. 5.3 from a static phantom recording with 20 mm radial averaging and no compensation for varying beam pair delay.

Fig. 5.4 shows the phase bias of the SPTD method versus range and beam pair index. The bias was found from calculating $\theta$ of Eq. 5.3 from a static phantom

recording using the SPTD acquisition pattern. $\theta$ was averaged over approximately 20 mm in the radial direction, and no compensation for varying beam pair delay was done. Ideally $\theta$ should be zero at all locations in a recording of at static phantom, but, as the figure shows, $\theta$ had a systematic pattern in the lateral direction which changed with depth.
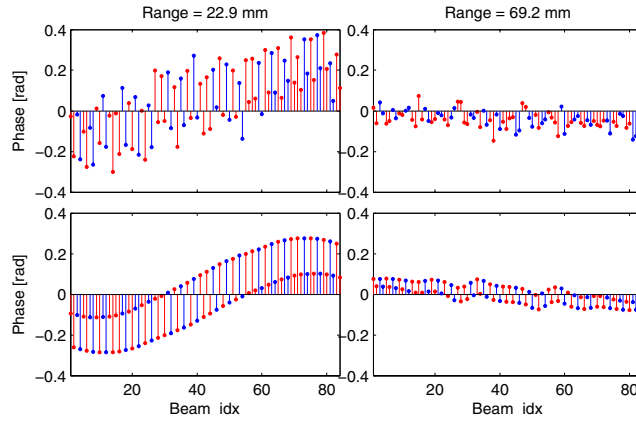


Figure 5.5: Comparison of simulated and measured phase bias. Top figure row shows the measured phase bias from static phantom recordings and bottom row shows the simulated phase bias as a function of beam pair index. Left figure column shows results from a range of 22.9 mm and the right figure column from a range of 69.2mm. Bias from beam pairs with positive delays are shown in red and negative delays in blue.

The top row of Fig. 5.5 shows plots of the measured phase bias at ranges 22.9 mm and 69.2 mm. The same phase bias should also be found from calculating the phase shift between the two-way responses of the scan lines at these depths [17]. The phase shifts found from simulating the two way responses of all scan lines at the same depths is shown in the bottom figure row of Fig. 5.5. These simulated phase shifts corresponded well with the measured ones. Notice the diagonal symmetry, and that the bias oscillates around a laterally slowly varying value.

The reason for this scan line dependent bias was found from investigating the lateral phase variation of the transmitted pressure field. Fig. 5.6 shows simulations of lateral phase variations across the transmit beam for ranges 22.9 mm and 69.2 mm. The first and second figure row show the transmitted pressure field and the transmit beam profile, respectively. The third figure row shows the actual phase variations. The same plots are repeated for range 69.2 mm in figure rows four to six. For both ranges the phase shift varied significantly with receive beam positions (indicated by the thin vertical lines). This resulted in phase shifts between the data from different parallel beams. The phase variation were largest at the 22.9 mm range. Notice that the phase profile was symmetrical for zero degree steering angles and asymmetrical when steering to either side. Also, the phase profiles were mirrored versions of each other when comparing positive and negative steering angles. This caused the s-shape
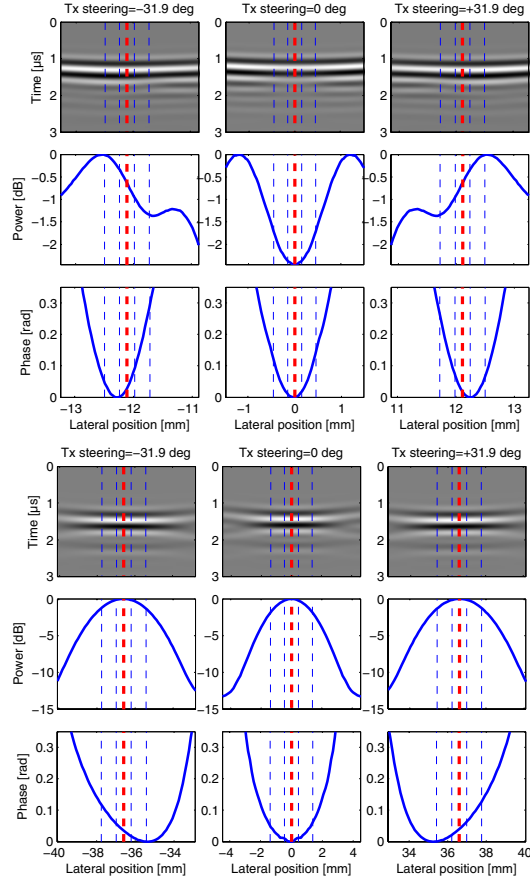
Figure 5.6: Transmit field lateral phase variations. Top three figure rows are from 22.9 mm range, bottom three figure rows from 69.2 mm range. Top figure row shows the transmitted pressure as a function of time, middle figure row shows the beam intensity profile and the bottom row shows the lateral phase variation of the transmitted field. The same description applies to the bottom three figure rows. First figure column shows results for a transmit steering angle of -31.9 degrees, second column 0 degrees and third column +31.9 degrees. Transmit directions are indicated by the thick, dashed, vertical, lines and the corresponding parallel beams are indicated by thin, dashed, vertical lines.

of the bias seen in the top left plot of Fig. 5.5.

Fig. 5.7 shows the simulated phase bias when imaging through a thorax aberrator. Compared to the unaberrated case in the top figure row of Fig. 5.5, the phase bias changed significantly with aberrations.

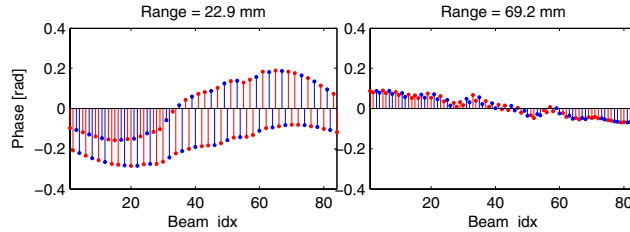Fig. 5.8 shows the applied bias compensation method step by step for range 22.9

Figure 5.7: Simulated phase bias with cardiac phase aberrations. Left plot shows the phase bias from range 22.9 mm and the right plot from range 69.2mm. Bias from beam pairs with positive delays are shown in red and negative delays in blue.

mm (which was the range with the highest bias). Beam pairs with positive delay are plotted in red and beam pairs with negative delay in blue. The top left plot shows the calculated phase, $\theta$, with no compensation. Top right plot shows the phase after compensation for beam pair delay variations. The phase of both positive and negative beam pairs are here related to $PRT_0$ (instead of $4 \cdot PRT_0$ and $-3 \cdot PRT_0$). In the middle left plot, the phases has been converted to velocities according to Eq. 5.4 and 5.5. In the middle right plot, $R_k(1)$ of two and two neighboring beam pairs has been averaged to remove the high frequency lateral bias variation. In the bottom left plot, $R_k(1)$ has been interpolated to all scan line positions. This was done separately for beam pairs with positive and negative delays. In the bottom right plot, $R_k(1)$ of positive and negative delay beam pairs has been averaged for each scan line position. For range 22.9 mm, this reduced the maximum absolute velocity bias from 4.82 cm/s to 0.32 cm/s (93.4%). For range 69.2 mm the maximum absolute velocity bias was reduced from 1.71 cm/s to 0.18 cm/s (89.5%).

Fig. 5.9 shows the standard deviation of the SPTD phase estimate as a function of the beam correlation coefficient. As could be expected, the phase estimate standard deviation dropped with increasing beam density (increasing beam correlation). The standard deviation of the measurements were compared to numerical simulations. The simulated and measured values corresponded well. The beam density of the main setup in Table 5.1 (43 tx beams, 65 degree sector) corresponds to the fourth data point from the left in this plot. The beam density of the narrow sector setup in Table 5.2 (8 transmit beams, 9 degree sector) corresponds to the sixth data point.

Fig. 5.10 shows a comparison between velocity curves from frame to frame tissue Doppler (F2FTD) and SPTD. F2FTD sample volumes are indicated in the B-mode image to the left, and the velocities are shown in corresponding order in the figure panes to the right. As could be expected, the SPTD curves showed a larger variance, but overall, good correspondence was found between the two methods at all sample volumes.

Fig. 5.11 shows a color M-mode comparison of SPTD processing and F2FTD processing. This plot shows the color coded velocities for all sample volumes along a straight line through the septum. The two processing methods produced quite similar images. The main differences were the fluctuations between positive and negative
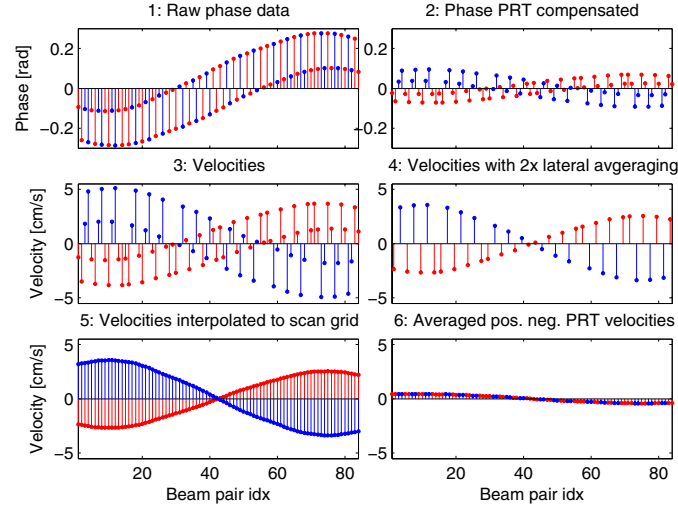
Figure 5.8: Bias compensation process step by step for range 22.9 mm. Red line indicates positive delay between correlated beams, blue line indicate negative delay. Top left: Simulated phase bias before beam pair delay compensation. Top right: Simulated phase bias after beam pair delay compensation. Middle left: Velocity bias after beam pair delay compensation. Middle right: Velocity bias after averaging correlation from two and two neighboring beam pairs. Bottom left: Velocity bias from step 4 interpolated to original scan grid. This was done separately for beam pairs with positive and negative delay. Bottom right: Velocity bias after averaging the interpolated correlation from positive and negative delay beam pairs of step 5.

velocities seen in the diastole using SPTD and the aliasing artifacts using F2FTD.

Fig. 5.12 shows an anatomical color M-mode image. This plot shows velocities at all points along a curve through the myocardium as a function of time. The left plot shows the location of the curve in a SPTD image of the left ventricle. The right plot shows the velocities clockwise along the curve. The y-axis indicates position along the curve and the x-axis time. The recording in the left plot is also available as video (*Ch5_Movie01.gif* located at *www.ntnu.no/us/ThesisMM/bjastad*).

## 5.5   Discussion

### 5.5.1   SPTD phase bias

The results clearly showed that a straight forward implementation of the SPTD method without any lateral averaging resulted in a phase estimation bias. When the method was applied on a simple recording of a static phantom, the estimated phase shifts fluctuated in a deterministic pattern laterally in the image (See Fig. 5.4). The reason for this bias was found by investigating the lateral phase variation across the
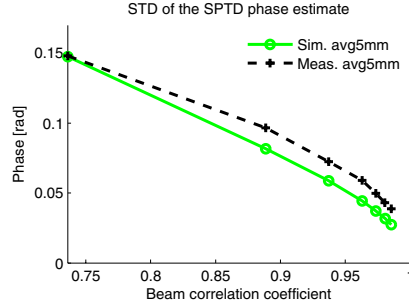
Figure 5.9: Standard deviation of the SPTD phase estimate as function of beam correlation coefficient. Dashed line with plus sign markers shows the measured standard deviation averaged over 5 mm. Solid line with circular markers shows the corresponding numerically simulated standard deviation. The phase values are before compensation for varying beam pair delay.

transmit beam (See Fig. 5.6). Simulations showed that this phase varied significantly across the transmit beam width. Using parallel beams, each receive beam then got a different phase shift dependent on its lateral offset. Larger offsets resulted in larger phase shifts. As shown in Fig. 5.2, the phase shift using SPTD is calculated from the autocorrelation between receive beams with different offsets. Due to this, the calculated phase shift can be larger than zero even if the imaged object is stationary. For the case of four parallel beams, the phase shift is calculated between two different combinations of beam offsets: small-large and large-small (See Fig. 5.2). If the transmit phase profile is symmetrical, such as in the middle figure column of Fig. 5.6, the phase shift will be positive for the first combination, and equally large but negative for the other combination. This is the scenario for beam index 42 and 43 in the simulated phase bias plots of Fig. 5.5. However, if the transmit beam phase profile is asymmetrical or the receive beams are positioned asymmetrically around the transmit direction, the phase bias of these two offset combinations will fluctuate around a value different from zero. This was the case when steering to the sides, as can be seen from the left and right figure columns of Fig. 5.6. Since the phase profiles in the left and right figure column are mirrored versions of each other, the SPTD phase bias plotted in Fig. 5.5 are diagonally symmetrical around zero degree steering direction.

The simulated and measured bias plotted in Fig. 5.5 showed strong similarities. Although there were some differences, the phase bias fluctuation and trend were very similar. This supports the theory that lateral transmit beam phase variations was the main cause of the phase estimation bias. The deviations between simulations and measurements could be due to differences between linear simulations at second harmonic frequency and actual second harmonic recordings.
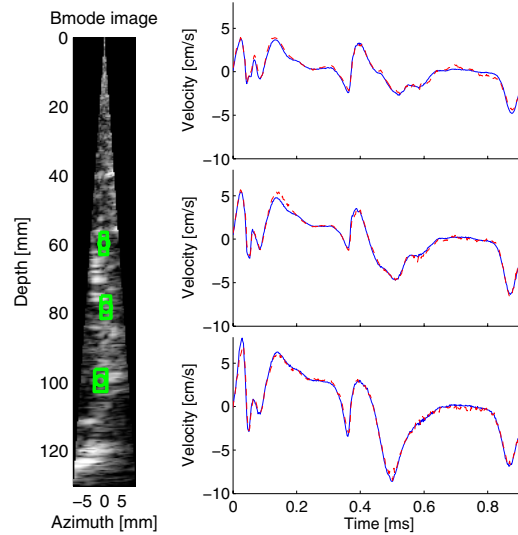
Figure 5.10: Comparison of velocity curves from the septum using SPTD and F2FTD. Narrow sector B-mode image with F2FTD sample volumes shown to the left. The corresponding velocity curves are shown to the right. The velocity curves from using F2FTD are shown in solid blue line style and SPTD in dashed red line style.

## 5.5.2 Bias compensation

The bias compensation approach chosen in this work was to perform lateral averaging (See Fig. 5.8). This was possible since the bias has opposite polarity for beam pairs with positive and negative delay (see left plot in figure row two). Since the mechanisms of the bias were known, this averaging could be done in a way where only the minimum number of beams necessary to cancel out the bias were averaged. The main advantage of this approach is the robustness. It will work regardless of acquisition parameters and phase aberrations. It will also reduce the phase estimate variance due to averaging over a larger number of samples. An other approach could have been to pre-calculate the bias based on models or simulations and subtract it. The advantage of such an approach would be the higher lateral resolution of the velocity estimates. However, it is likely to fail due to aberrations. Fig. 5.7 shows that the bias changes significantly with cardiac strength phase aberrations. This will make it impossible to accurately pre-calculate the bias. Subtracting pre-calculated values might actually increase the bias in such scenarios. Another approach might be to estimate the phase bias from recorded data and then subtract it. Since the bias is depth varying, the bias would have to be estimated for all depths. Such a method is beyond the scope of this work, but it is likely that it would be less robust than our proposed model based averaging.

For the two ranges investigated, 22.9 mm and 69.2 mm, the maximum absolute velocity bias was reduced with 93.4% and 89.5% respectively. Since the beam pair delay compensation scales the bias differently for positive and negative delay beam
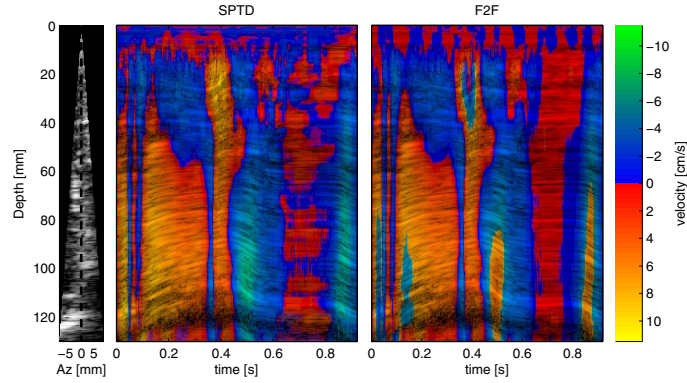
Figure 5.11: Color M-mode comparison from SPTD processing and F2FTD processing. The left plot shows the narrow sector B-mode image. The location of the M-mode line is indicated with a black dashed line. The middle plot shows the CM-mode image from using SPTD processing, and the right plot shows the CM-mode image from using F2FTD processing.
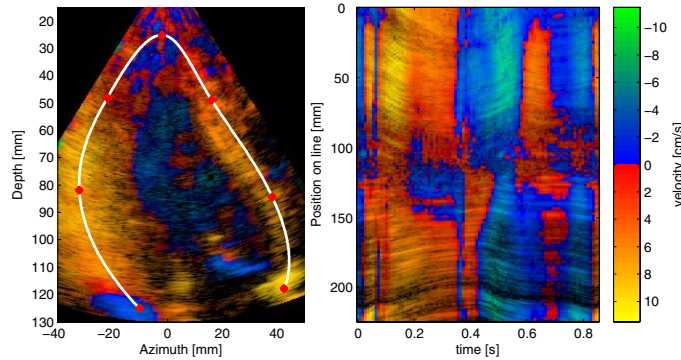


Figure 5.12: Anatomical color M-mode using the SPTD-technique. The left plot shows the tissue Doppler image and the location of the CM-mode anatomical line. The right plot shows the anatomical CM-mode. The y axis follows a clockwise rotation along the anatomical CM-mode line. The frame rate of the recording was 110 frames per second. 30 dB B-mode dynamic range. Video: *Ch5_Movie01.gif* located at *www.ntnu.no/us/ThesisMM/bjastad*

pairs, some bias will remain (see Eq. 5.6 and 5.7). How much the bias is reduced for other setups will depend on the interleaving factor $X$ and the transmit beam lateral phase profile.

### 5.5.3 Phase estimate variance

Fig. 5.9 shows the standard deviation of the phase estimate (Eq. 5.3) as a function of the beam correlation coefficient. The good correspondence between measured and simulated standard deviation shows that decorrelation is the main mechanism for the variance in the phase estimate. Since SPTD calculates the phase shift between identical receive beam directions but neighboring transmit directions, the correlation will be lower for SPTD than conventional TDI. Increasing the transmit beam spacing will lower the inter beam correlation and increase the phase estimate variance. Hence, when designing a SPTD setup there will always be a tradeoff between high frame rate and low variance in the phase estimates. Also, the velocity variance will be different for positive delay beams and negative delay beams since the phase is scaled differently when compensating for beam pair delay variations (See Eq. 5.6 and 5.7). The SPTD interleave pattern chosen in this work results in delays $4 \cdot PRT_0$ for positive delay beam pairs and $-3 \cdot PRT_0$ for negative delay beam pairs. After beam pair delay compensation, the standard deviation of negative delay beam pairs will therefore be $4/3$ of the positive delay beam pair standard deviation. This was however difficult to observe in the *in vivo* images.

### 5.5.4 Validation of the SPTD velocity estimate

The results from validating the SPTD method against conventional TDI are displayed in Fig. 5.10 and 5.11. A frame rate high enough to do tissue Doppler processing from frame to frame (F2FTD) was achieved by recording a narrow sector. This allowed for direct comparison between the methods on the same data set. The validation showed that the SPTD velocity estimates are quite accurate and only slightly deviates from those of the standard F2FTD method. This can be seen in detail for three sample volumes along the septum in Fig. 5.10 and color coded for all sample volumes in Fig. 5.11. The most visible differences were found in the cardiac diastole, where the cardiac tissue is stationary (located around 0.7 seconds in Fig. 5.10 and 5.11). Due to the sharp color transition between positive and negative velocities, the higher variance in the velocity estimate becomes very visible here. The aliasing artifacts seen in the high velocity areas of the F2FTD image were due to the larger beam pair delay when doing the tissue Doppler processing from frame to frame.

## 5.6 Conclusion

In this work we investigated a novel method which produces high frame rate B-mode and tissue Doppler images from the same acquisition. The method utilizes the phase shift between overlapping receive beams from neighboring transmit events. Using model based averaging for bias compensation, the bias caused by transmit beam lateral phase variations was almost eliminated. The cost of this bias compensation was some reduction on lateral resolution. Validations against conventional tissue Doppler processing showed good correspondence, although a higher variance in the velocity

estimate. Using the SPTD technique, tissue Doppler images with a sector width of 65 degrees were captured at a frame rate of 110 frames per second.

## Acknowledgement

# References

[1] W. McDicken, G. Sutherland, C. Moran, and L. Gordon, "Colour doppler velocity imaging of the myocardium," *Ultrasound Med Biol*, 1992.

[2] B. Lind, J. Nowak, J. Dorph, J. van der Linden, and L. A. Brodin, "Analysis of temporal requirements for myocardial tissue velocity imaging," *Eur J Echocardiogr*, vol. 3, pp. 214–9, Sep 2002.

[3] H. Kanai, H. Hasegawa, N. Chubachi, Y. Koiwa, and M. Tanaka, "Non-invasive evaluation of local myocardial thickening and its color-coded imaging," *IEEE Transactions on Ultrasonics Ferro-electrics and Frequency Control*, 1997.

[4] H. Kanai, M. Sato, Y. Koiwa, and N. Chubachi, "Transcutaneous measurement and spectrum analysis of heart wall vibrations," *IEEE Trans UFFC*, 1996.

[5] C.-M. Yu, E. Chau, J. E. Sanderson, K. Fan, M.-O. Tang, W.-H. Fung, H. Lin, S.-L. Kong, Y.-M. Lam, M. R. Hill, and C.-P. Lau, "Tissue doppler echocardiographic evidence of reverse remodeling and improved synchronicity by simultaneously delaying regional contraction after biventricular pacing therapy in heart failure," *Circulation*, 2002.

[6] M. Penicka, J. Bartunek, B. D. Bruyne, M. Vanderheyden, M. Goethals, M. D. Zutter, P. Brugada, and P. Geelen, "Improvement of left ventricular function after cardiac resynchronization therapy is predicted by tissue doppler imaging echocardiography," *Circulation*, 2004.

[7] D. P. Shattuck, M. D. Weinshenker, S. W. Smith, and O. T. von Ramm, "Explososcan: A parallel processing technique for high speed ultrasound imaging with linear phased arrays," *J. Acoust, Soc. Amer.*, vol. 75, no. 4, pp. 1273–1282, 1984.

[8] O. T. von Ramm, S. W. Smith, and H. G. Pavy, "High-speed ultrasound volumetric imaging system – part ii: Parallel processing and image display," *IEEE transactions on ultrasonics, ferroelectrics, and frequency control*, vol. 38, March 1991.

[9] T. Bjåstad, S. A. Aase, and H. Torp, "The impact of aberration on high frame rate cardiac b-mode imaging," *IEEE transactions on ultrasonics, ferroelectrics, and frequency control*, vol. 54, January 2007.

[10] T. Hergum, T. Bjåstad, K. Kristoffersen, and H. Torp, "Parallel beamforming using synthetic transmit beams," *IEEE transactions on ultrasonics, ferroelectrics, and frequency control*, vol. 54, February 2007.

[11] J. Kirkhorn, S. Bjærum, B. Olstad, K. Kristoffersen, and H. Torp, "A new technique for improved spatial resolution in high frame rate color doppler imaging," *Proceedings IEEE Ultrasonics Symposium*, 2003.

[12] S. Bjaerum, H. Torp, and K. Kristoffersen, "High frame rate tissue doppler imaging," *Proceedings IEEE Ultrasonics Symposium*, 2001.

[13] P. R. Detmer, J. R. Jago, and X.-N. Li, "Method and apparatus for obtaining b-flow and b-mode data from multiline beams in an ultrasound imaging system." U.S. Patent 6,589,177 B1, 2002.

[14] M. Bernard J. Savord, Andover, "Method and apparatus for increasing the frame rate and resolution of a phased array imaging system." U.S. patent 5.318.033, 1992.

[15] B. S. Robinson, "Ultrasonic diagnostic imaging systems with blended multiline for 2d and 3d applications." U.S. Patent 6.482.157, Mar. 30 2001.

[16] R. Chesarek, "Ultrasound imaging system for relatively low-velocity blood flow at relatively high frame rates." U.S. Patent 4,888,694, 1989.

[17] R. F. Wagner, S. W. Smith, J. M. Sandrik, and H. Lopez, "Statistics of speckle in ultrasound b-scans," *IEEE transactions on ultrasonics, ferroelectrics, and frequency control*, 1983.

[18] J. A. Jensen and N. B. Svendsen, "Calculation of pressure fields from arbitrarily shaped, apodized, and excited ultrasound transducers," *IEEE Trans. Ultrason.,Ferroelec., Freq. Contr.*, 1992.

[19] L. M. Hinkelman, T. L. Szabo, and R. C. Waag, "Measurements of ultrasonic pulse distortion produced by human chest wall," *J. Acoust. Soc. Am.*, 1997.

[20] T. Johansen, B. Angelsen, and W. Nordhøy, "Phase aberrations - experiments and simulations," *Proceedings of the 23rd Scandinavian Symposium on Physical Acoustics*, 2000.